

---

---

# One dimensional (1D) nanostructured Silicon as Anode for Rechargeable Lithium-ion Batteries

---

## Dissertation

zur Erlangung des

Doktorgrades der Ingenieurwissenschaften (*Dr.-Ing.*)

des

Zentrums für Ingenieurwissenschaften

der Martin-Luther-Universität Halle-Wittenberg

vorgelegt

von

Herrn Gibaek Lee

geboren am 11.05.1979 in Seoul, Korea

1. Gutachter: *Prof. Dr. rer. nat. Ralf B. Wehrspohn*,  
Martin-Luther-Universität Halle-Wittenberg
2. Gutachter: *Prof. Dr.-Ing. Thomas Mikolajick*,  
Technische Universität Dresden

Tag der Verteidigung: 12.11.2015

## Dedication

*To My Loving Parents.*

*For their endless love, support and encouragement*



# ABSTRACT

---

Electrochemical energy storage systems are becoming increasingly important with respect to their use in portable electronic devices, medical implantable devices, hybrid electric (HEV) and electric vehicles (EVs), and storage of solar and wind energies. Rechargeable lithium-ion battery is one of the most promising systems for them due to its high energy density and long cycle life. However, the sustainable development of new anode material with higher capacity or energy density remains one of the major challenges for lithium-ion batteries. Silicon nanowires (SiNWs) are drawing attention as a promising candidate for the anode material in lithium-ion batteries due to its huge high specific capacity of  $4,200 \text{ mAh}\cdot\text{g}^{-1}$  (10 times higher than conventional graphite anode), as well as stress accommodation for reversible lithiation and delithiation.

One dimensional (1D) silicon nanowires (SiNWs) and black silicon (b-Si) fabricated via metal assisted chemical etching (MaCE), and inductively coupled plasma reactive ion etching (ICP-RIE) methods respectively, are investigated as new anode material in lithium-ion batteries. The electrochemical studies of the SiNWs and b-Si have been performed in half-cells using  $\text{LiPF}_6$  in EC-DEC as electrolyte with a glass fiber separator.

Both SiNW and b-Si electrodes can maintain their structure during Li-insertion and extraction processes despite large volume expansion. The high-resolution electron microscopy analysis shows the composition of lithiated SiNWs consist of the unreacted crystalline silicon core and the reacted amorphous Li-Si alloy shell. In particular, the Li-Si shell is comprised of a mixture of amorphous silicon oxide and crystalline silicon, leading to hindrance during Li-Si alloying/dealloying upon cycling.

In case of the b-Si electrodes, the cycle life of the nanostructured Si electrode is heavily influenced by the constant reformation of the SEI layer depending upon the surface composition. In the fast lithiation experiments, it is important to maintain balance in the chemical kinetics between the lithium ion diffusion and the electron injection during the lithiation of nanostructured Si.

The metal-coated nanostructured Si electrodes deliver stable capacity retention and cycle life. In particular, the Cu-coated b-Si shows the most promising electrochemical performance enhancements for the initial specific capacity as well as their cyclability compared to pristine b-Si. The electrochemical and microstructural properties before and after cycling of the metal-coated nanostructured Si will be discussed in detail.

# Contents

<b>Abstract</b>	<b>I</b>
<b>List of Contents</b>	<b>II</b>
<b>List of Figures</b>	<b>IV</b>
<b>Abbreviations</b>	<b>VIII</b>
<b>1 Introduction</b>	<b>1</b>
1.1 Motivation . . . . .	1
1.2 Rechargeable lithium ion batteries . . . . .	2
1.2.1 Introduction . . . . .	2
1.2.2 Electrochemical processes . . . . .	4
1.2.3 Basic battery components . . . . .	5
1.3 Silicon anodes: An overview . . . . .	6
1.3.1 Advantage and challenge . . . . .	6
1.3.2 Approaches for improving Si anode performance . . . . .	9
1.4 The aim and outline of this work . . . . .	11
<b>2 Experimental and Technical Methodologies</b>	<b>12</b>
2.1 Fabrication methods for nanostructured silicon . . . . .	12
2.1.1 Introduction and mechanism of MaCE . . . . .	12
2.1.2 Introduction and mechanism of ICP-RIE . . . . .	15
2.2 Battery cell setup . . . . .	18
2.3 Electrochemical analysis methods . . . . .	20

2.3.1	Cyclic voltammetry . . . . .	20
2.3.2	Galvanostatic methods . . . . .	20
2.4	Characteristic analysis methods . . . . .	23
2.4.1	Scanning Electron Microscopy (SEM) . . . . .	23
2.4.2	Transmission Electron Microscopy (TEM) . . . . .	23
2.4.3	X-ray Diffraction (XRD) . . . . .	23
2.4.4	X-ray Photoelectron Spectroscopy (XPS) . . . . .	24
<b>3</b>	<b>Silicon Nanowires (SiNWs) as Anode Material</b>	<b>25</b>
3.1	Experimental . . . . .	25
3.1.1	Silicon nanowires (SiNWs) fabrication via MaCE . . . . .	25
3.1.2	Silicon nanowires (SiNWs) properties . . . . .	26
3.2	Results and Discussion . . . . .	29
3.2.1	Electrochemical investigation of SiNWs anodes . . . . .	29
3.2.2	Lithium intercalation in individual SiNWs . . . . .	33
3.3	Summary . . . . .	41
<b>4</b>	<b>Nanostructured Black Silicon (b-Si) as Anode Material</b>	<b>42</b>
4.1	Experimental . . . . .	42
4.1.1	Nanostructured black silicon (b-Si) fabrication via ICP- RIE technique . . . . .	42
4.1.2	Nanostructured black silicon (b-Si) properties . . . . .	43
4.2	Results and Discussion . . . . .	44
4.2.1	Electrochemical measurements of b-Si anodes . . . . .	44
4.2.2	Surface modifications of b-Si anode materials . . . . .	49
4.2.3	Si substrate influence at a high C-rate . . . . .	57
4.3	Summary . . . . .	62

<b>5</b>	<b>Metal-coated Nanostructured Silicon (M-Si) as Anode Material</b>	<b>63</b>
5.1	Experimental . . . . .	64
5.1.1	Metal-coated nanostructured silicon (M-Si) fabrication via sputtering . . . . .	64
5.1.2	Metal-coated nanostructured silicon (M-Si) properties . .	65
5.2	Results and Discussion . . . . .	70
5.2.1	Electrochemical measurements of M-Si anodes . . . . .	70
5.2.2	Cyclability for M-Si anodes . . . . .	74
5.2.3	Electrochemical characterization of M-Si anodes . . . . .	77
5.3	Summary . . . . .	82
<b>6</b>	<b>Conclusions and Outlook</b>	<b>83</b>
6.1	Conclusions . . . . .	83
6.2	Suggestions and Recommendations . . . . .	85
	<b>Bibliography</b>	<b>86</b>
	<b>Publications</b>	<b>95</b>
	<b>Acknowledgements</b>	<b>97</b>

# List of Figures

1.1	Comparison of the different battery technologies . . . . .	2
1.2	Scheme of a common rechargeable lithium ion battery. . . . .	3
1.3	Specific capacities of lithium metal alloys . . . . .	7
1.4	Si-Li equilibrium phase diagram and li/delithiation curves . . . . .	8
1.5	Si volume expansion from Si to full-discharge state of Si . . . . .	9
1.6	Comparison of Si structural changes during cycling . . . . .	10
2.1	Scheme of the fabrication process for SiNWs via MaCE . . . . .	13
2.2	Scheme of the formation of SiNWs on the Si substrate . . . . .	14
2.3	Schematics of the ICP-RIE . . . . .	15
2.4	Scheme of the fabrication process for b-Si via ICP-RIE . . . . .	17
2.5	Photograph of materials . . . . .	19
2.6	Scheme for self-designed li-ion cell . . . . .	19
2.7	Scheme of a typical current-voltage cycle (CV) . . . . .	21
2.8	Comparison of the different discharge curves . . . . .	22
3.1	Photograph of 4-inch Si wafer before and after MaCE . . . . .	26
3.2	SiNWs length vs. etching time . . . . .	27
3.3	SEM and TEM images of SiNWs prepared by MaCE . . . . .	28
3.4	EDX spectrum and XRD patterns of as-prepared SiNWs . . . . .	28
3.5	CV profile for the pristine SiNWs electrode . . . . .	30
3.6	Photograph of SiNWs electrode before and after CV . . . . .	30
3.7	XRD patterns comparison before and after CV and SEM . . . . .	31
3.8	Charge/discharge profile of the SiNWs . . . . .	32

3.9	SEM and TEM images of SiNWs electrode after 70 cycles . . . . .	33
3.10	HR-TEM images of SiNW electrode after 70 cycles . . . . .	34
3.11	Voltage profile as function of time of SiNWs . . . . .	34
3.12	TEM and HR-TEM images of lithiated single SiNW . . . . .	35
3.13	XPS spectra of SiNWs electrode at the lithiation/delithiation . . . . .	37
3.14	TEM and EELS spectra of the lithiated single SiNW . . . . .	38
3.15	HAADF-STEM and EELS of the lithiated SiNW . . . . .	40
4.1	Photograph and SEM of 4-inch black silicon wafer . . . . .	43
4.2	SEM of nanostructured b-Si prepared by ICP-RIE . . . . .	44
4.3	CV profile for the pristine b-Si electrode . . . . .	45
4.4	Galvanostatic charge/discharge curve of pristine b-Si . . . . .	46
4.5	SEM of lithiated/delithiated b-Si at the 1 <sup>st</sup> cycle. . . . .	47
4.6	Discharge capacity vs. coulombic efficiency of the pristine b-Si . . . . .	48
4.7	TEM of the lithiated b-Si electrode . . . . .	50
4.8	XPS spectra comparison between b-Si and SiNWs . . . . .	51
4.9	High resolution XPS spectra of pretreatment of b-Si . . . . .	52
4.10	Comparison for surface properties of b-Si and SiNWs . . . . .	53
4.11	CV profile of the pretreated b-Si electrode . . . . .	54
4.12	First charge/discharge profile of pristine and pretreated b-Si . . . . .	56
4.13	Charge/discharge profile and potential drop profile . . . . .	58
4.14	Discharge capacity vs. cycle numbers of b-Si . . . . .	60
4.15	Scheme of the failure of the b-Si electrode . . . . .	60
4.16	Photograph and SEM of b-Si electrodes after accelerated cycle . . . . .	61
5.1	Photograph of metal-coated nanostructured silicon electrodes . . . . .	64
5.2	Morphology of metal-coated SiNWs electrodes . . . . .	66
5.3	Morphology of metal-coated b-Si electrodes . . . . .	67
5.4	XRD patterns of metal-coated nanostructured Si electrodes . . . . .	69
5.5	Charge/discharge profiles of metal-coated Si electrodes . . . . .	71
5.6	Initial charge/discharge profiles of metal-coated Si . . . . .	73

5.7	Discharge capacity vs. cycle number for metal-coated Si . . . . .	75
5.8	SEM of Au- and Cu-coated b-Si after 50 cycles . . . . .	76
5.9	CV profile for metal-coated SiNWs electrode . . . . .	78
5.10	SEM for metal-coated SiNWs after 50 cycles . . . . .	79
5.11	CV profile of metal-coated b-Si electrode . . . . .	80
5.12	SEM of metal-coated b-Si after 50 cycle . . . . .	81

# ABBREVIATIONS

---

b-Si	nanostructured black silicon
CMOS	complementary metal-oxide semiconductor
CV	cyclic voltammetry
DRIE	deep reactive ion etching
EDX	energy-dispersive X-ray spectroscopy
EELS	electron energy loss spectroscopy
HAADF-STEM	high-angle annular dark-field scanning transmission electron microscopy
ICP-RIE	inductively coupled plasma reactive ion etching
MaCE	metal assisted chemical etching
redox	reduction-oxidation
SAED	selected area electron diffraction
SEI	solid electrolyte interphase
SEM	scanning electron microscopy
SHE	standard hydrogen electrode
SiNW	silicon nanowires
TEM	transmission electron microscopy
XPS	X-ray photoelectron spectroscopy
XRD	X-ray Diffraction

---



# Chapter 1

## Introduction

### 1.1 Motivation

Energy storage and production is one of the greatest challenges facing mankind in the 21<sup>th</sup> century. The rapid depletion of fossil fuel reserves, rising fuel costs, increasing greenhouse gas emission, and global climate changes are driving the development of sustainable clean energy technologies like fuel cells, solar cells, high energy density batteries, and supercapacitors. While fuel cells and solar cells are energy conversion devices, batteries and supercapacitors are energy storage devices.

Especially today, with the proliferation of various wireless communication devices, electric vehicles (EVs), and implantable devices arising from remarkable developments, the 21<sup>th</sup> century is moving toward the information-rich, mobile society, where high-quality information services are available regardless of time and place. Therefore, energy storage development becomes one of the most important topics. Energy storage, an intermediate step to the versatile, clean, and efficient use of energy, has received worldwide concern and increasing research interest. Rechargeable lithium ion batteries are appealing for these needs because of their high energy density, wide range of operating temperatures, and long shelf and cycle life.

Currently, rechargeable lithium ion batteries use graphite as anodes for reversible lithium intercalation and deintercalation. Graphite reaches the limits for the development of high capacity lithium ion batteries with a maximum theoretical specific capacity of  $\approx 372 \text{ mAh} \cdot \text{g}^{-1}$  corresponding to the formation of  $\text{LiC}_6$ . With that, silicon is drawing attention as upcoming noteworthy candidate for an anode material in rechargeable lithium ion batteries owing to its high theoretical specific capacity of  $\approx 4,200 \text{ mAh} \cdot \text{g}^{-1}$  at fully lithiated state of  $\text{Li}_{4.4}\text{Si}$  and low operating voltage of  $\approx 0.4 \text{ V}$ (vs.  $\text{Li}/\text{Li}^+$ ). Hence, the need for the fundamental understanding of the lithium reaction mechanism with silicon and phase transformation of  $\text{Li-Si}$  alloys during cycling arises. Novel nanostructured silicon anodes will be presented in this work.

## 1.2 Rechargeable lithium ion batteries

### 1.2.1 Introduction

Rechargeable lithium ion batteries have both the highest volumetric and gravimetric energy density among known technologies applied, including lead-acid, nickel-cadmium, nickel metal hydroxide and other systems as plotted in **Fig. 1.1** [1, 2].

Rechargeable lithium batteries involve a reversible insertion/extraction of lithium ions into/from a host electrode material during the charge/discharge process. The lithium insertion/extraction process occurring with a flow of ions through the electrolyte is accompanied by a reduction-oxidation (redox) reaction of the host matrix assisted with a flow of electrons through the external circuit [3, 4]. A schematic presentation of a rechargeable lithium ion battery is shown in **Fig. 1.2**.

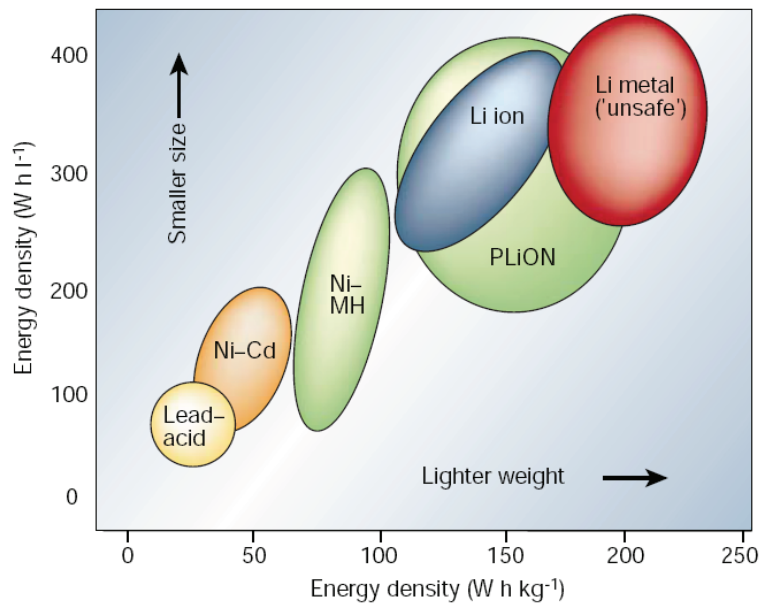


**Figure 1.1:** Comparison of the different battery technologies in terms of volumetric and gravimetric energy density. The share of worldwide sales for Ni-Cd, Ni-MH and Li-ion portable batteries is 23, 14 and 63 %, respectively [1].

The anode is the electropositive electrode from which electrons are generated to do external work. In a lithium cell, the anode contains lithium, commonly held within graphite in the well-known lithium ion batteries. The cathode is the electronegative electrode to which positive ions migrate inside the cell and electrons migrate through the external electrical circuit. The electrolyte allows the flow of positive ions, for example lithium ions, from one electrode

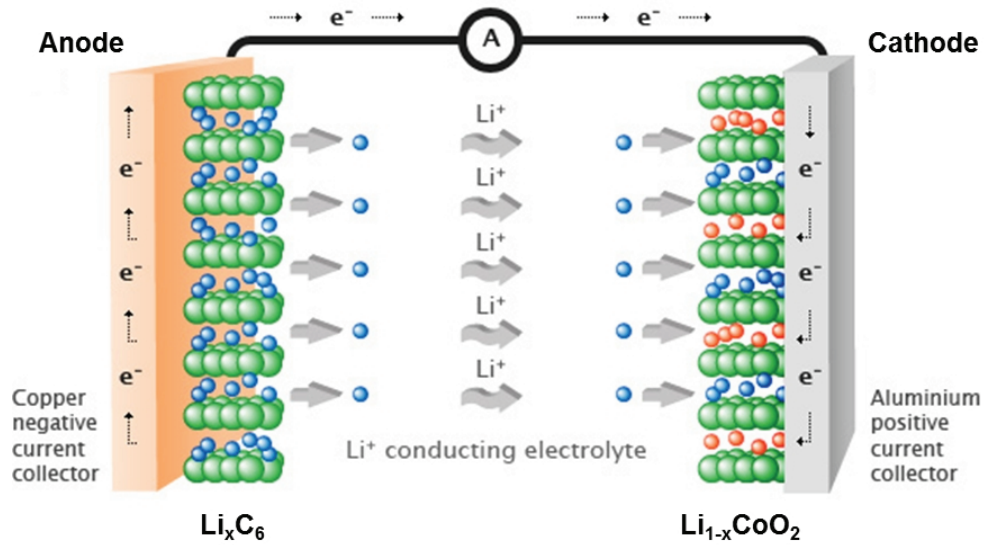


**Figure 1.2:** Scheme of a common rechargeable lithium ion battery.

to another. It allows the flow only of ions and not of electrons. The electrolyte is commonly a liquid solution containing a salt dissolved in a solvent.

The electrolyte must be stable in the presence of both electrodes. The current collectors allow the transport of electrons to and from the electrodes. They are typically metals and must not react with the electrode materials. Typically, copper is used for the anode and aluminum for the cathode (the lighter-weight aluminum reacts with lithium and therefore cannot be used for lithium-based anodes).

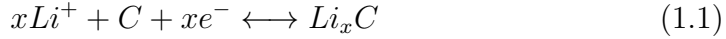
The cell voltage is determined by the energy of the chemical reaction occurring in the cell. The anode and cathode are, in practice, complex composites. They contain, besides the active material, polymeric binders to hold the powder structure together and conductive diluents such as carbon black to give the whole structure electronic conductivity so that electrons can be transported to the active material. In addition these components are combined so as to leave sufficient porosity to allow the liquid electrolyte to penetrate the powder structure and the ions to reach the reacting sites.

## 1.2.2 Electrochemical processes

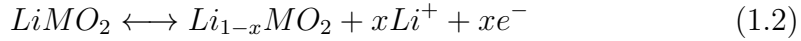
An electrochemical cell is the smallest unit of a device that converts chemical energy to electric energy, or vice versa. The three primary functional participants in the electrochemical reactions in a lithium ion battery are the anode, the cathode and the electrolyte.

During the discharge process, lithium ions ( $\text{Li}^+$ ) carry the current from the negative to the positive electrode, through the nonaqueous electrolyte and separator. During charging, an external electric power source applies a higher voltage than that produced by the battery, forcing the current to pass in the reverse direction. The lithium ions then migrate from the positive to the negative electrode, where they become embedded in the porous electrode material in a process known as intercalation. The following equations, (eq. 1.1), (eq. 1.2) and (eq. 1.3), are the corresponding reactions of anode and cathode upon **charging** and **discharging**, and the reactions are reversed during discharging [5]:

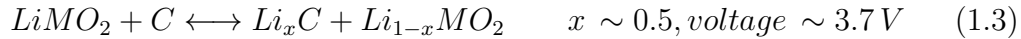
The anode half-reaction is



The cathode half-reaction is



The overall reaction is



### 1.2.3 Basic battery components

The total capacity of a rechargeable lithium ion battery strongly depends on capacities of anode, cathode and other components. Therefore, the role of battery components is important in a lithium ion battery. The most commercially popular anode material is graphite.

Li metal is attractive as an anode material due to its most negative potential ( $-3.045$  vs. standard hydrogen electrode) and the lowest material density ( $0.534 \text{ g} \cdot \text{cm}^{-3}$ ) [1]. However, it encounters the shortcomings of a Li–liquid electrolyte combination. By contrast, carbonaceous anodes offer a stable morphology resulting in consistent safety properties over their useful life.

The cathode is generally one of three materials: a layered oxide (such as lithium cobalt oxide), a polyanion (such as lithium iron phosphate), or a spinel (such as lithium manganese oxide).

The electrolyte is typically a mixture of organic carbonates such as ethylene carbonate (EC) or diethyl carbonate (DEC) containing complexes of lithium ions. These nonaqueous electrolytes generally use non-coordinating anion salts such as lithium hexafluorophosphate ( $\text{LiPF}_6$ ), lithium perchlorate ( $\text{LiClO}_4$ ), lithium hexafluoroarsenate monohydrate ( $\text{LiAsF}_6$ ), and lithium tetrafluoroborate ( $\text{LiBF}_4$ ) [6].

The battery separator is a porous sheet placed between the negative and positive electrodes in a liquid electrolyte, a gel electrolyte, or a molten salt electrolyte. Its function is to prevent physical contact of the negative and positive electrodes while serving as an electrolyte reservoir to enable free ionic transport.

A current collector is the key component of electron conduction between the electrode materials and the external circuit in lithium ion batteries. As the name implies, the function of current collector is assembling up current from active materials to form a large current output, which should have a low resistance.

## 1.3 Silicon anodes: An overview

### 1.3.1 Advantage and challenge

Following the commercialization of lithium ion batteries in 1991, graphite and other carbon materials have been used as anode materials. As electric devices become increasingly lightweight, compact and multifunctional, the energy density of lithium ion batteries should be enhanced to achieve long operating times. However, the lithium storage capacity ( $\text{LiC}_6$ ) has been limited to  $372 \text{ mAh} \cdot \text{g}^{-1}$  (or  $830 \text{ mAh} \cdot \text{cm}^{-3}$ ). This problem can be overcome by using anode materials with a larger lithium storage capacity. Among the candidates as anode materials, Si and Sn have been considered as one of the most attractive anode materials for lithium ion batteries.

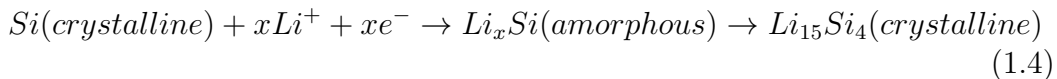
Li can be electrochemically alloyed with a number of metallic and semi-metallic elements in groups IV and V of the periodic table, such as Si, Sn, Ge, Pb, P, As, Sb, and Bi [7, 8, 9], and also some other metal elements, such as Al, Au, In, Ga, Zn, Cd, Ag, and Mg [10, 11, 12]. Comparison of several anode materials including density, theoretical specific capacity, charge density, volume change and onset potential for lithium insertion are tabulated as follows in **Table 1.1**. In particular, C, Si and Sn have been studied extensively [13].

Other elements such as Al, Ge and Pb have low reversible efficiency reactions and high average working potentials, making them inappropriate as anode materials. In this respect, Si is drawing attention as upcoming noteworthy candidate for an anode material in lithium ion batteries owing to its high theoretical specific capacity of  $\approx 4,200 \text{ mAh} \cdot \text{g}^{-1}$  at fully lithiated state of  $\text{Li}_{4.4}\text{Si}$  and its low operating voltage of  $\approx 0.4 \text{ V}$  (vs.  $\text{Li}/\text{Li}^+$ ) [14, 15, 16]. Moreover Si is also abundant, cheap, and environmentally benign.

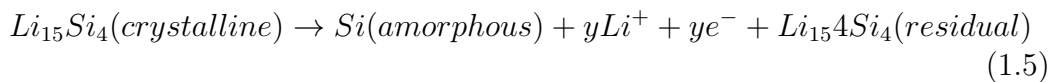
These metals react with lithium at a specific voltage range during charging to become alloys and return to their original state when discharged, thus allowing continuous reversible charge/discharge cycles. Reversible reactions occur upon alloying/dealloying with lithium unlike intercalation/deintercalation reactions in graphite. The capacity per unit mass/volume of metal elements known to form alloys with lithium ( $\text{Li}_x\text{M}$ ) is shown in **Fig. 1.3** [17].

The charge/discharge reaction mechanism of silicon anode is as follows at room temperature [18, 19, 20]:

**Discharge process:**



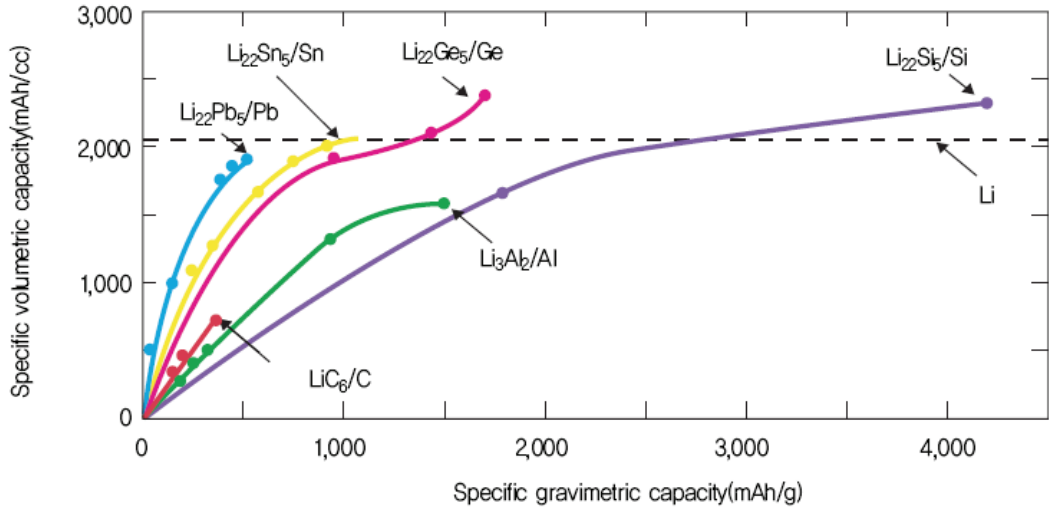
**Charge process:**



**Table 1.1:** Comparison of various anode materials for lithium ion battery including: density, theoretical specific capacity, charge density, volume change and onset potential for lithium insertion [13].

Materials	Li	C	Li <sub>4</sub> Ti <sub>5</sub> O <sub>12</sub>	Si	Sn	Sb
Density ( $g \cdot cm^{-3}$ )	0.53	2.25	3.5	<b>2.33</b>	7.29	6.7
Lithiated phase	Li	C	Li <sub>7</sub> Ti <sub>15</sub> O <sub>12</sub>	<b>Li<sub>4.4</sub>Si</b>	Li <sub>4.4</sub> Sn	Li <sub>3</sub> Sb
Theoretical specific capacity ( $mAh \cdot g^{-1}$ )	3862	372	175	<b>4 200</b>	994	660
Theoretical charge density ( $mAh \cdot cm^{-3}$ )	2047	837	613	<b>9,786</b>	7246	4422
Volume change (%)	100	12	1	<b>320</b>	260	200
Potential vs. Li ( $\sim V$ )	0	0.05	1.6	<b>0.4</b>	0.6	0.9

In the two-phase region during the lithiation process, crystalline Si becomes an amorphous Li–Si alloy and the amorphous phase suddenly crystallizes as a Li<sub>15</sub>Si<sub>4</sub> phase when the potential of the Si electrode is around 50 mV (vs. Li/Li<sup>+</sup>) at room temperature [18, 21, 22]. There is another two-phase region during the delithiation process, consisting of amorphous Si and residual Li<sub>15</sub>Si<sub>4</sub> phase. In this context, the phase of each compound can be conjectured from the phase diagram shown in **Fig. 1.4**.

**Figure 1.3:** Specific capacities of lithium metal alloys (charge capacity per unit volume includes the change in volume after alloying with lithium) [17].

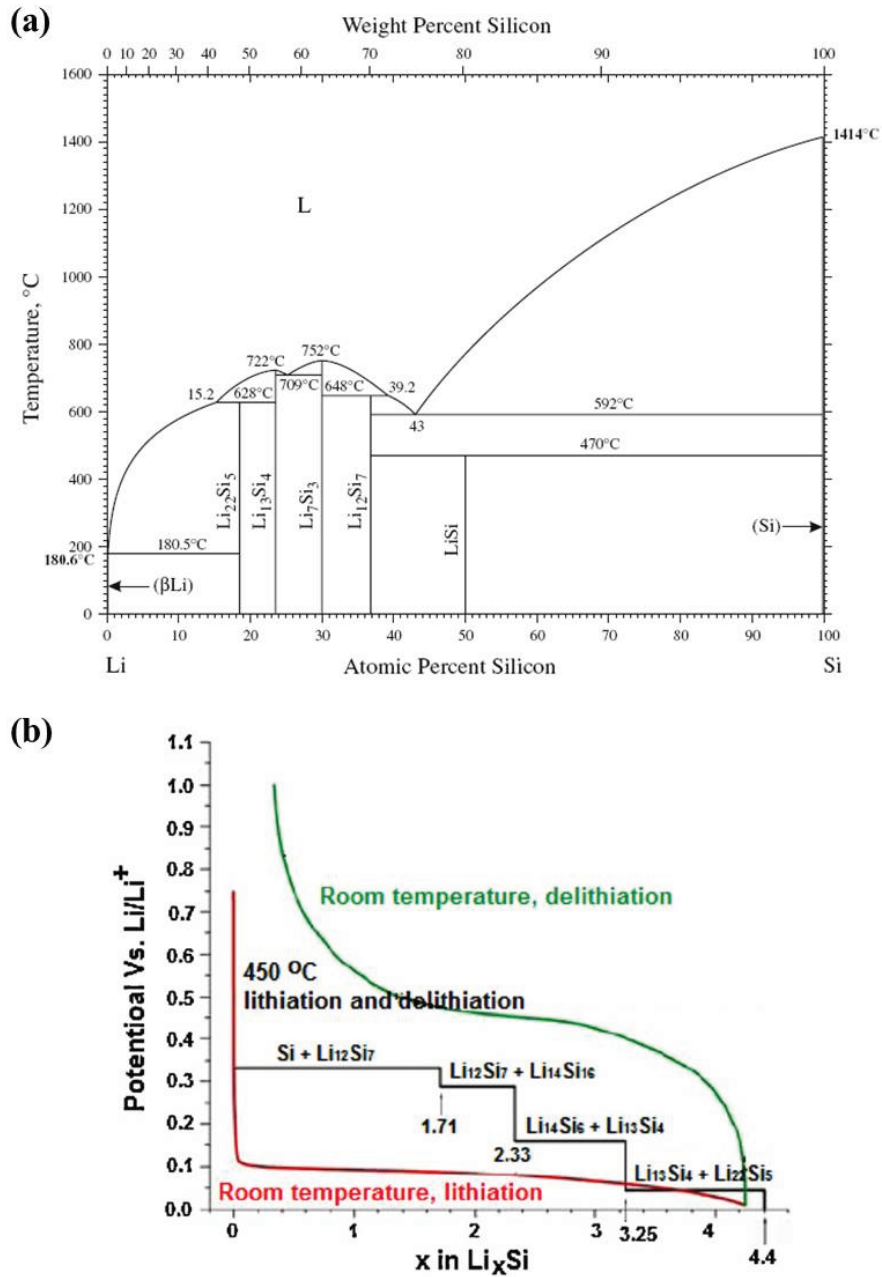


**Figure 1.4:** (a) Si-Li equilibrium phase diagram [23] and (b) Si electrochemical lithiation and delithiation curve at room temperature and high temperature. Black line: theoretical voltage curve at 450 °C. Red and green line: lithiation and delithiation of crystalline Si at room temperature, respectively [24].



### 1.3.2 Approaches for improving Si anode performance

Despite attractive features of silicon as anode material, the practical use of Si-based anodes suffers from poor capacity retention associated with its severe volume change ( $\sim 320\%$ ) during Li insertion into and extraction from silicon. This feature leads to cracking and pulverization of Si-based anodes induced by the large mechanical stresses, resulting in a loss of electric contact and eventually capacity fading during cycling (see **Fig. 1.5**) [11, 12, 13, 21, 22, 23, 24, 25, 26, 27, 28, 29]. Moreover, the formation of a solid/electrolyte interphase (SEI) at the interface layer between Si anode and electrolyte is an obstacle for practical applications. Previous studies in which Si films and micro-sized particles are used as anodes in lithium batteries have shown large capacity fading and short battery cycle life. The reason for this lies in the pulverization and loss of electrical contact between the active material and the current collector (see **Fig 1.6**) [18, 30, 31, 32]. Therefore, the main issue of improvement of Si anodes cyclability is how to overcome the volume change problem.

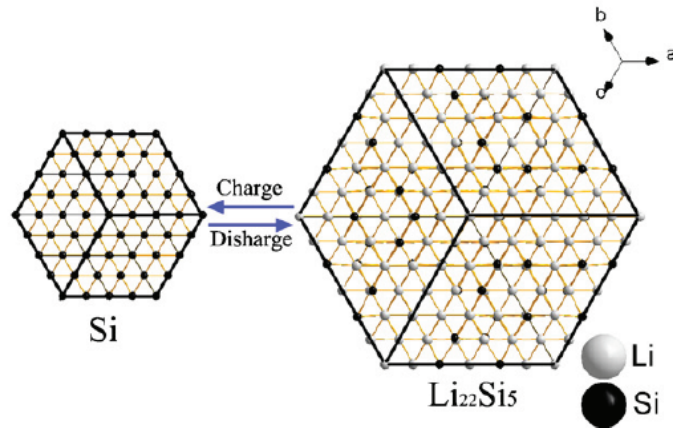


**Figure 1.5:** Illustration of Si volume expansion from Si to the full-discharge state of  $\text{Li}_{22}\text{Si}_5$ . During the whole charge and discharge process, the volume of Si undergoes a volume change of about 320% [27].

Various approaches have been carried out to overcome this issue, including the use of nano-sized active materials, active/inactive composite materials, and silicon-carbon composites [28, 30, 34, 35, 36, 37, 38]. Cui and co-workers recently published a seminal paper [33] that demonstrated that anodes comprised of silicon nanowires (SiNWs) are able to accommodate large strain without pulverization, and provide good electronic contact (see **Fig. 1.6**). One-dimensional (1D) nanomaterials such as nanowires and nanotubes have exhibited the enhanced electrochemical properties compared to bulk materials. This is because 1D nanostructures allow better accommodation of the huge volume change without the physical fracture. In addition, 1D nanostructures provide direct electronic path way allowing sufficient electron transport. Lastly, large surface areas of nanostructures allow reactions between the lithium ion and the silicon during cycling. Although this approach should show the enhanced

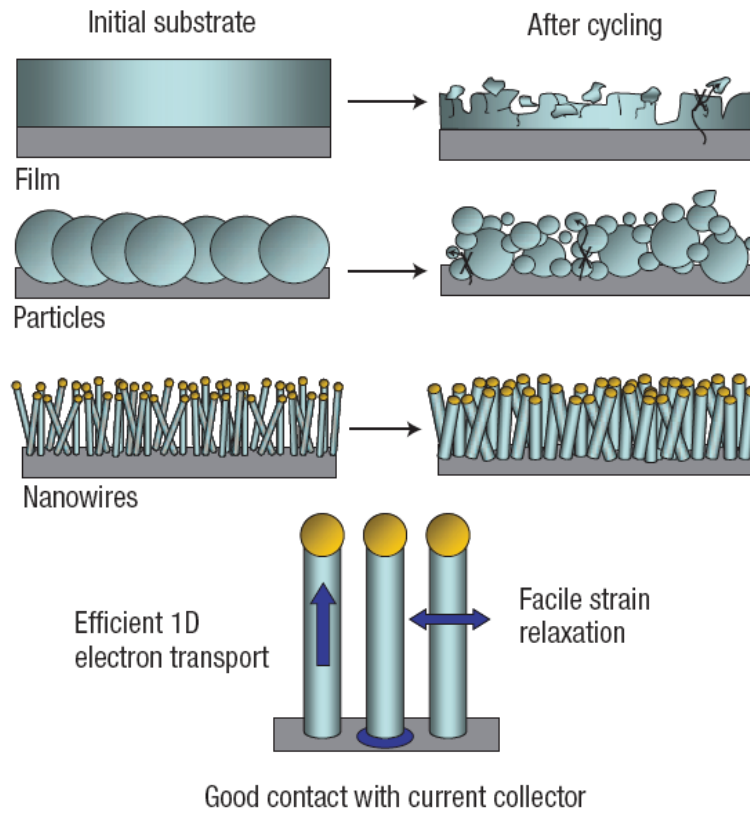


**Figure 1.6:** Schematic illustrations for comparison of structural changes that occur in Si anodes during electrochemical cycling in the form of film, particles and nanowires [33].

capacity and long cycle life for lithium ion batteries, the fast capacity fading is still present and the lithium reaction mechanisms and morphology changes are not yet fully understood. To understand the reasons for the poor cycling stability of Si anodes, the fundamental understanding of the lithium reaction mechanism and phase transformation during cycling should be investigated.

## 1.4 The aim and outline of this work

The aim of this dissertation is to understand the fundamental reaction mechanism between lithium ions and one dimensional (1D) nanostructured silicon as anodes, including deformation mechanism, mechanical stress caused by volume change, fracture of electrodes, and a good way to improve in lithium ion batteries.

After the motivation of the study in this chapter 1, chapter 2 demonstrates the mechanism of nanostructured Si fabrication, including the metal-assisted chemical etching (MaCE) and inductively coupled plasma reactive ion etching (ICP-RIE). The electrochemical analysis and measurement methods for lithium ion batteries are described.

In chapter 3, SiNWs prepared by MaCE are applied as anode material for lithium ion batteries, and investigated by the electrochemical measurements including cyclic voltammetry, charge/discharge cycling, and the material characterization of Li-Si alloys such as XPS, TEM, SAED, and EELS analysis.

Chapter 4 demonstrates the structural and electrochemical properties of a new type of well-ordered 1D nanostructured black silicon (b-Si) fabricated by ICP-RIE process as an anode material for rechargeable lithium ion batteries. The lithium storage characteristics and the morphology change of the b-Si electrode are investigated, and the critical factors influencing the charge/discharge (lithiation/delithiation) behavior are discussed.

Chapter 5 discusses the potential of a fully CMOS-compatible technology for metal-coated 1D silicon nanostructures using MaCE and ICP-RIE, and successive coating by metal magnetron sputtering. For comparison and evaluation of metallic additive materials, gold (Au) as a representative active metal material and copper (Cu) as an inactive metal material are used, respectively. Discussions including specific capacity, capacity retention, and cycle life of metal-coated silicon nanostructures compared with pristine silicon nanostructures will be presented.

Chapter 6 is the conclusion of this dissertation, including characteristics of the 1D SiNWs anodes prepared by MaCE and ICP-RIE, respectively, and electrochemical properties as Si anode material for lithium ion batteries. Several suggestions and recommendations are proposed for the improvement of future work in lithium ion batteries, covering high specific capacity, long-term cycle life, and stable capacity retention for practical application.

# Chapter 2

## Experimental and Technical Methodologies

In this chapter, I discuss methods for nanostructured Si fabrication via metal-assisted chemical etching (MaCE) and inductively coupled plasma reactive ion etching (ICP-RIE) techniques, and introduce electrochemical analysis and measurement methods with battery cell setup for lithium-ion batteries.

### 2.1 Fabrication methods for nanostructured silicon

#### 2.1.1 Introduction and mechanism of metal-assisted chemical etching (MaCE)

**Introduction** The wet etching into bulk Si substrates can give a nano- and micro geometrical Si structure, which is a relatively easy and economical method. The resulting structure has a high aspect ratio comparable to the Si dry etching which needs generally expensive vacuum equipment. Hence, the metal-assisted chemical etching (MaCE) method is a simple and low-cost approach to fabricate the silicon nanowires (SiNWs) with designable doping grade. The MaCE method proposed by Peng and co-workers can fabricate SiNWs by electroless etching in hydrofluoric acid solutions with metal catalysts [39, 40, 41, 42, 43]. MaCE method can generally be classified into two types: one-step (MaCE-I) and two-step (MaCE-II) reactions. **Fig. 2.1** shows the schematic diagrams of MaCE-I and MaCE-II. Both MaCE procedures are composed of two processes: a metal catalyst involving noble metals (e.g., Au, Ag or Pt) or coinage metals (e.g., Cu, Ni) is deposited partly onto Si substrate, followed by electroless etching of silicon derived by the metal catalysts. As a result, the detail geometries of silicon structures depend on the initial morphology of metal catalysts.

In this work, I focus on the etching reactions on the basis of MaCE-I. As for MaCE-I, only second etching processes occur sequentially in etching solutions, and the generation of SiNWs is much faster than MaCE-II using  $H_2O_2$  as the oxidant.

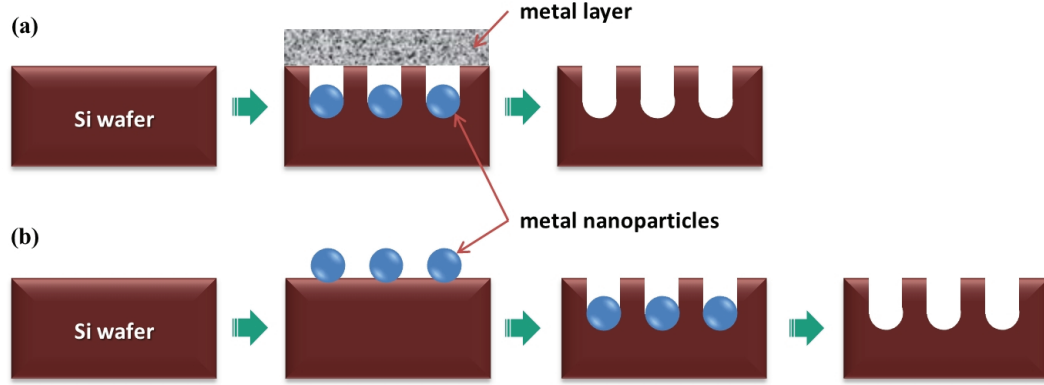


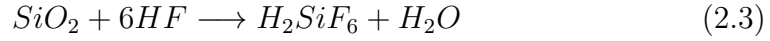
**Figure 2.1:** Schematic diagrams of the fabrication process for SiNWs via MaCE. (a) One-step (MaCE-I) and (b) two-step (MaCE-II) reaction processes.

**Mechanism** The reaction mechanism is a complex electrochemical process even though MaCE-I consists of a one-step reaction only. The SiNWs are produced by immersing the Si wafer into an aqueous solution with hydrofluoric acid and silver nitrate ( $HF/AgNO_3$ ). A spontaneous reduction of Ag ions and oxidation of silicon takes place [44, 45, 46, 47]. The nucleation of  $Ag^+$  ions preferentially occurs at the Si surface. An Ag ion in the environs of the Si substrate captures an electron from Si, leading to the reduction of the  $Ag^+$  ion consuming only one electron (eq. 2.1). Afterwards, silicon is oxidized to  $SiO_2$  (eq. 2.2), which is dissolved by HF (eq. 2.3). The excess oxidation is permissible to accumulate electrons on the nuclear surfaces and electrically drive  $Ag^+$  ions toward the nuclei for reduction. Hereby, consequent reaction brings about the growth of Ag particles. The reactions repeatedly take place, resulting in a downwards motion of the Ag particles into the Si substrate. Therefore,  $Ag^+$  ions are reduced and formed consistently in a dendrite layer and amassed on the top of SiNWs, which lead to repetitive and successive reaction.

This mechanism can be possible because the reduction potential of  $Ag^+/Ag$  is more positive than the flat band potential of silicon. The cathodic reaction for Ag reduction and anodic reaction for silicon oxidation are as follows [42, 48]:



In addition, silicon oxides are etched by HF and dissolved in solution:



The Ag particles sinking direction governs the crystalline structure and surface orientation of the as-generated SiNWs [44, 49, 50]. As a result, highly-ordered SiNW arrays are created on the Si substrate (see **Fig. 2.2**).

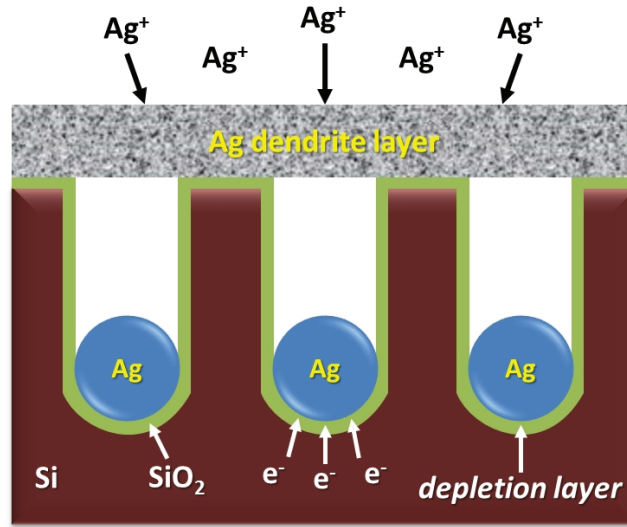


**Figure 2.2:** Schematic representation of the formation of highly-ordered SiNWs on the Si substrate in aqueous HF/AgNO<sub>3</sub> solution (MaCE-I).

### 2.1.2 Introduction and mechanism of inductively coupled plasma reactive ion etching (ICP-RIE)

**Introduction** The dry etch can be associated with the use of plasma reactions. Plasma etching techniques are one of the essential cornerstones of modern semiconductor fabrication [51, 52, 53]. These etching systems are routinely employed in industry for fabrication of integrated circuits and microelectromechanical systems. In general, plasma etching is done by ionizing a gas mixture to obtain ions reacting with the target material. The process depends, of course, on its parameters, such as gas flow, pressure and R.F. power. The balance between gas flow and R.F. power controls the ionization rate of the gases, while a higher pressure increases the probability of ions to get in contact with the target material. Also note that the gases flows control the rate at which products are evacuated from the chamber [54].

In this section, I describe the application of plasmas including etching and depositing methods to fabricate the nanostructured silicon. All these processes rely on the reactive ion etching (RIE). For treating Si and SiO<sub>2</sub> substrates it is used usually with the inductively coupled plasma (ICP) (see **Fig.2.3**).

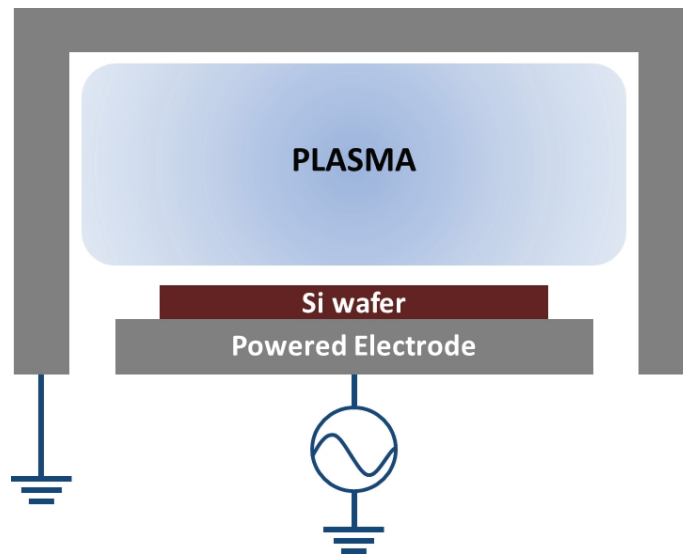


**Figure 2.3:** Schematics of the inductively coupled plasma reactive ion etching (ICP-RIE).

**Mechanism** The ICP-RIE chemistry is based on the well-known Bosch process [55, 56, 57], wherein deep reactive ion etching (DRIE) is an extension of RIE to indicate that the etching is anisotropic and can be used to etch pattern very deeply in the substrate. In order to achieve deep etches in silicon, two basic etch requirements must be met, which is the temporal separation of the etching and deposition reaction. This idea was first described by Tsujimoto et al. in 1986 for etching of tungsten or silicon using  $\text{SF}_6$  [58]. Later, this technique was applied for the etching of silicon, using  $\text{SF}_6$  as etching gas and  $\text{CHF}_3$  as deposition gas [59, 60]. The principle of this etching technique is depicted in **Fig. 2.4**.

At first a deposition step,

- (1) Polymer deposition: passivation layer is deposited, resulting in nothing or only little ion induced polymerization. The process gases used are a mixture of  $\text{CHF}_4$  and  $\text{CH}_4$ .

After this step, alternating plasma steps continue as the etching cycle:

- (2) Polymer removal (sputtering): the polymer layer has to be removed at the bottom using gas mixture of  $\text{SF}_6$ , Ar and  $\text{O}_2$ .
- (3) Etching (RIE): etching of silicon proceeds at the bottom of trench. These process conditions are usually the same as the polymer removal step.

Since the process gases required for the deposition and the etching cycle are different, they are continuously switched during the complete recipe or process. This DRIE of the process gases is one major distinction to conventional continuous-flow etching techniques, where the process gas mixture is constant during the complete etching process, and is the reason for its special name: gas chopping etching technique.



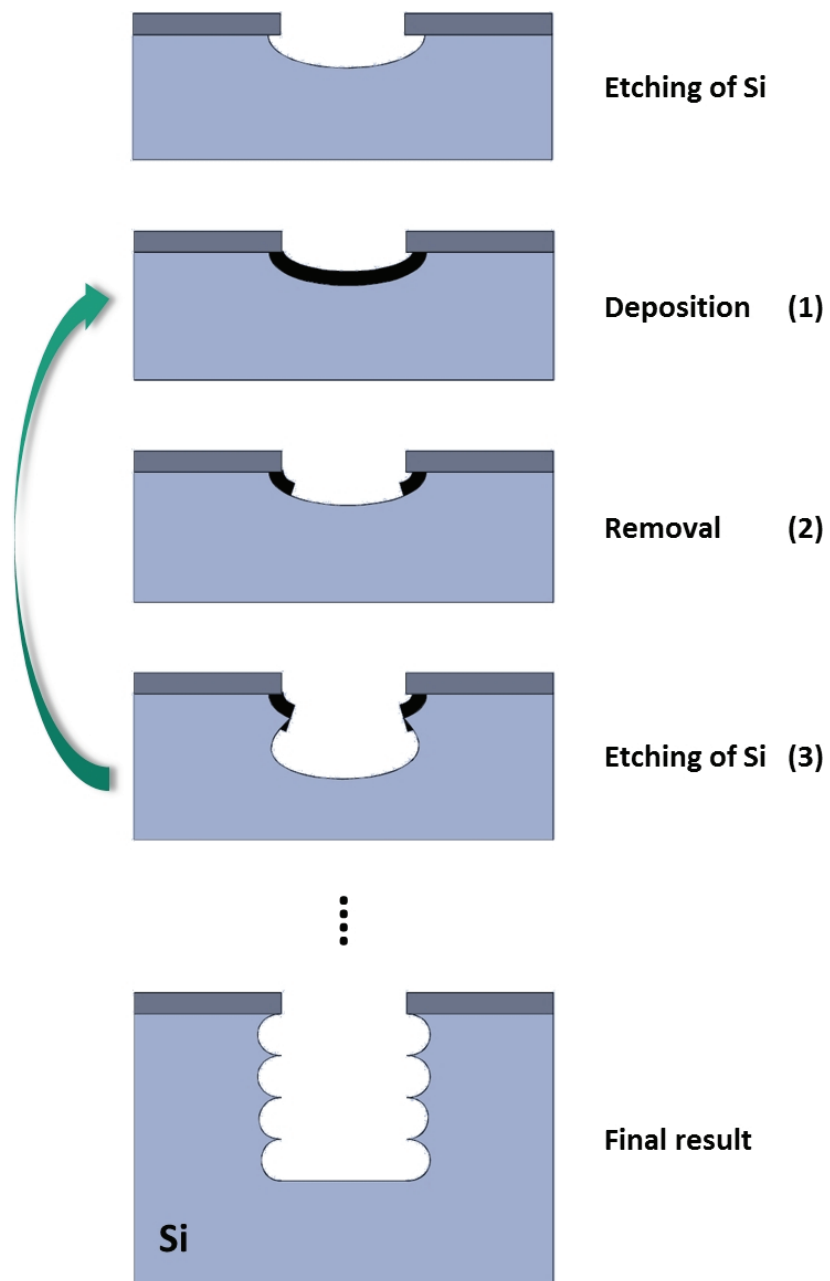


**Figure 2.4:** Schematic diagrams of the fabrication process for deep black silicon via the inductively coupled plasma reactive ion etching (ICP-RIE) method.

## 2.2 Battery cell setup

The wafer-scale nanostructured Si is cut into small pieces of suitable size and cleaned to remove oxides and impurities using a dilute hydrofluoric solution (see **Fig. 2.5**). To investigate the electrochemical properties of the nanostructured Si as anode, a lithium-ion half-cell is set up as a typical three-electrode cell (Swagelok cell) with excess electrolyte, nanostructured Si with 10 mm-diameter pieces as working electrode and a lithium foil as reference and counter electrode. A glass fiber (GF) separator is placed between the two electrodes. The back of the working electrode is placed in mechanical contact with the copper foil as a current collector, with no binder or conducting material. The reason for this is to investigate the effect of pure silicon only upon lithiation/delithiation (see **Fig. 2.6**). All of the Swagelok<sup>®</sup> cells are assembled and disassembled in an argon-filled glove-box (< 0.1 ppm oxygen, SylaTech GmbH) at room temperature. The electrolyte is 1 M LiPF<sub>6</sub> (lithium hexafluorophosphate) dissolved in 1:1 (w/w) mixture of ethylene carbonate (EC) and diethyl carbonate (DEC) (Merck).

In this work, all specific capacity data of charge and discharge are normalized by the geometric anode surface area that is exposed to the electrolyte. Thus, the current density is based on the average active material per anode area ( $\mu\text{A} \cdot \text{cm}^{-2}$ ). In addition, the discharge sequence represents lithiation due to silicon anode cell.

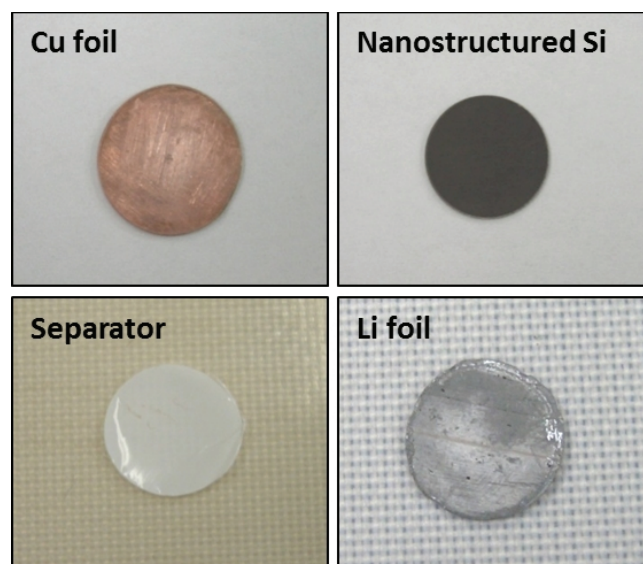


**Figure 2.5:** Images of materials: copper foil (current collector), nanostructured Si (working electrode), glass fiber (separator), and Li foil (counter and reference electrode).

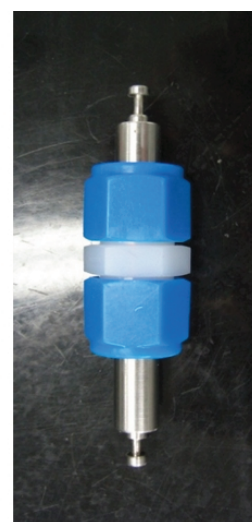
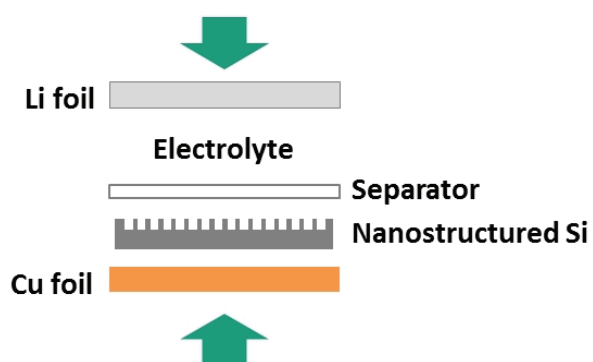


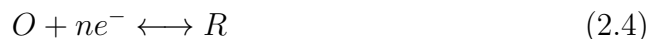
**Figure 2.6:** Scheme for self-designed Lithium-ion cell and Swagelok<sup>®</sup> cell.

## 2.3 Electrochemical analysis methods

### 2.3.1 Cyclic voltammetry

In describing batteries, cyclic voltammetry is a key electrochemical analysis method, giving information on the current available at any given cell voltage [61, 62, 63]. The voltage is swept between two values at a constant scan rate, however when the voltage reaches  $V_2$  the scan is reversed and the voltage is swept back to  $V_1$ , as is illustrated in **Fig. 2.7(a)**. Therefore, the scan rate,  $(V_2-V_1)/(T_2-T_1)$ , is a critical factor, since the duration of a scan must provide sufficient time to allow for a meaningful chemical reaction to occur. Thus, a low scan rate is recommended for detailed analysis of electrochemical reactions. Cyclic voltammetry repeats the same experiment for each cycle. Current-voltage curves obtained from cyclic voltammetry are different from linear plots, providing information on redox reactions occurring within the cell, including (1) potential, (2) quantity of electricity, (3) reversibility and (4) continuity. The scan rate alters depending on the purpose of experiments.

**Fig. 2.7(b)** is a typical cyclic voltammogram showing changes in current with varying applied potential. Oxidative reactions are induced by the anodic current when the scan direction is (+), while reductive reactions occur for (-). At sufficiently oxidizing or reducing potentials, where the ratio of electron transfer between the electrode and the redox species in solution is sufficiently fast, the Faradaic current is controlled by the rate of diffusion to the electrode. Hence, for the reversible reduction of redox species O and R, respectively



Therefore, it is possible to gain an estimate for the electron transfer rate constants by analyzing the variation of peak position as a function of the scan rate.

### 2.3.2 Galvanostatic methods

In general, the galvanostatic charge-discharge technique is widely used for characteristic of active materials in the electrochemical analysis method. When an electrochemical cell is assembled, this method can accurately provide the performance evaluation of active materials and the result data is based on reaction characteristic of active materials used in Lithium-ion batteries. The parameters are discharge curve, charge curve, coulombic efficiency, and cycle life. The discharge and charge curves are another important feature of battery system in determining the specific capacity and efficiency. The current rate can also have a significant effect on the performance of the battery system.

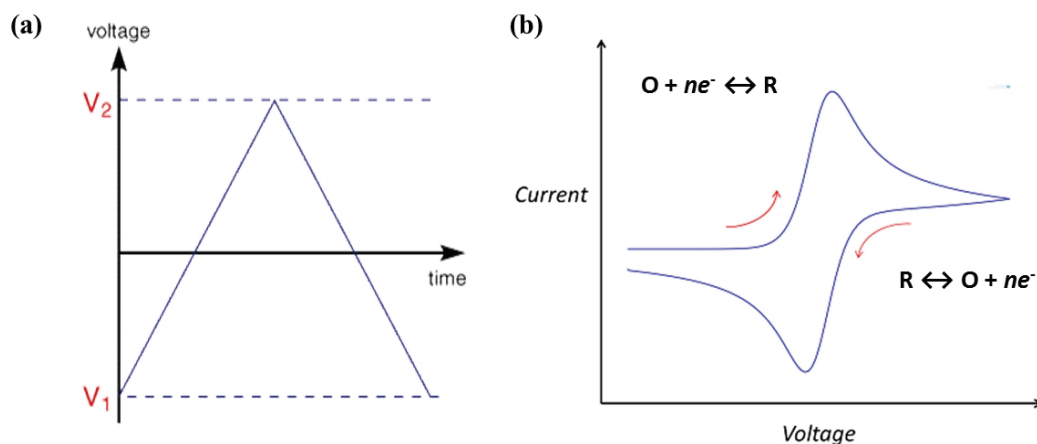


**Figure 2.7:** (a) Cyclic voltammetry potential function and (b) schematic diagram of a typical current-voltage cycle.

**Cycle life** Cycle life is the numbers of charge and discharge cycles that a battery can achieve before its capacity is depleted. A high performance battery should be able to maintain its capacity even after thousands of charge and discharge cycle. The cycle life of lithium ion batteries strongly depends on the structural stability of electrode active material during the charging and discharging process. Irreversible capacity, which is the amount of charge lost, is usually observed after the first cycle and results from the formation of a new layer at the interface of electrode and electrolyte such as a solid/electrolyte interphase (SEI).

**Discharge curves** The discharge curve is a plot of the voltage against the percentage of the capacity discharged. A flat discharge curve is desirable as this means that the voltage remains constant as the battery is used up. Repeated cycles affect the discharge characteristics of a battery, allowing the discharge curve to take various forms depending on discharge conditions, electrical properties, and other measurement variables. With the same battery consisting the same materials and cell design, various discharge curves can be produced according to measurement conditions. It is essential to compare these discharge curves to obtain a more accurate understanding of battery properties. The typical discharge curves of batteries are shown in **Fig. 2.8**.

In this work, galvanostatic charge-discharge measurements for the nanostructured Si electrode are performed using a battery testing system (Neware Co., Ltd.).

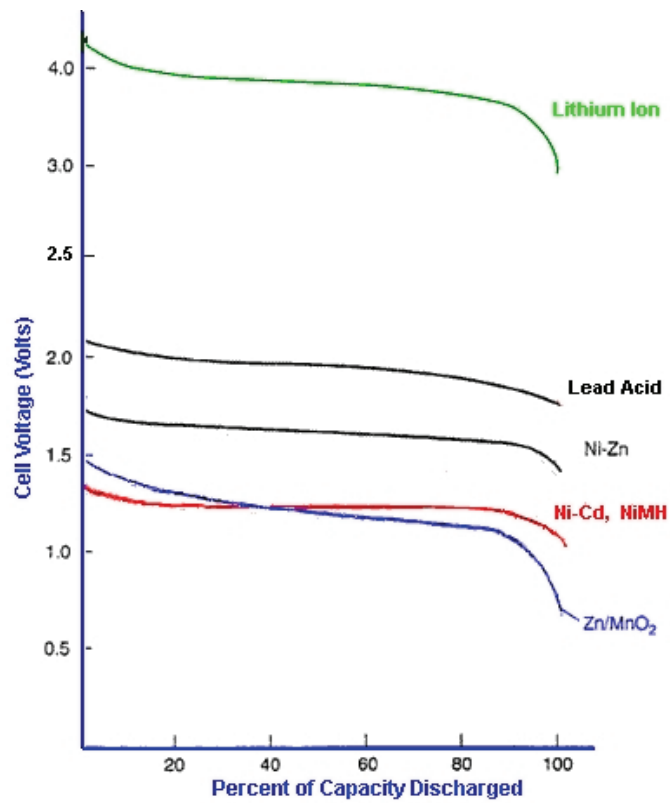


**Figure 2.8:** Comparison of the different discharge curves. The X axis shows the cell characteristics normalized as a percentage of cell capacity so that the shape of the graph can be shown independent of the actual cell capacity [64].

## 2.4 Characteristic analysis methods

### 2.4.1 Scanning Electron Microscopy (SEM)

Morphology characterizations of nanostructured Si electrodes are investigated by using scanning electron microscopy (SEM, JEOL-6700F) as well as field-emission scanning electron microscopy equipped with energy-dispersive spectroscopy (FE-SEM/EDX, Hitachi S-4300).

### 2.4.2 Transmission Electron Microscopy (TEM)

Transmission Electron Microscopy (TEM) is an imaging method whereby a beam of electrons is transmitted thorough an ultra-thin specimen, interacting with the specimen as it passes through. Therefore, TEM is a useful tool in material characterization and nanotechnology, which can provide nanometer scale high-resolution images for crystal lattices and atomic layer structures. From TEM, bright field (BF) images, dark field (DF) images, and selected area electron diffraction (SAED) patterns can be obtained.

An SAED aperture is used to observe diffraction patterns in a limited area. By restricting the observation region, diffraction patterns seen on the fluorescent plane correspond to the selected area only. In addition, electron energy-loss spectroscopy (EELS) is an analytical technique that measures the change in kinetic energy of electrons after they have interacted with a specimen. When carried out in a modern TEM, EELS is capable of giving structural and chemical information about a solid, with a spatial resolution down to the atomic level in favorable cases.

The microstructures and crystallographic orientations of nanostructured Si are evaluated by high-angle annular dark-field scanning transmission electron microscopy (HAADF-STEM, FEI Titan 80-300) and field-emission transmission electron microscopy (FE-TEM, JEOL JEM-2100F) equipped with SAED and EELS analysis.

### 2.4.3 X-ray Diffraction (XRD)

X-ray diffraction (XRD) is a technique used to characterize the crystallographic structure, crystallite size (grain size), and preferred orientation of a polycrystalline or solid specimen.

XRD patterns of the specimens are obtained the device from RIGAKU company, D/MAX-2200V/PC with Cu- $K\alpha$  radiation. The instrument is fully automated at room temperature and operates in conjunction with a comprehensive database.

#### 2.4.4 X-ray Photoelectron Spectroscopy (XPS)

X-ray photoelectron spectroscopy (XPS) is performed by irradiating the specimen with a beam of X-ray and measuring photoelectrons emitted by the material. Each element produces a characteristic set of XPS peaks at characteristic binding energy values, which gives direct evidence of each element that exists in or on the surface of the active material being analyzed. Thus, XPS analysis has been widely applied to investigate the silicon surface and SEI chemical composition.

XPS characterization for specimens is carried out via an Axis Ultra instrument (Kratos Analytical). XPS spectra are obtained with a monochromatic Al- $K\alpha$  X-ray source. Survey scans and high-resolution photoelectron spectra of the F 1s, O1s, C 1s, and Si 2p peaks are acquired with a pass-energy of 20 eV in hybrid (electrostatic and magnetic lens) mode with a slot aperture.



# Chapter 3

## Silicon Nanowires (SiNWs) as Anode Material

In this chapter, I present the fabrication for well-oriented silicon nanowire arrays (SiNWs) on Si substrate via one-step MaCE and study their potential as anodes for lithium-ion batteries. In Section 3.1, the fabrication and characterizations of as-prepared SiNWs electrodes are shown. Afterwards, the galvanostatic charge/discharge cycles of SiNWs electrodes related to lithium-ion insertion and extraction electrochemically are demonstrated in Section 3.2. Furthermore, the fundamental phenomenon of the reaction between lithium ions and silicon at the initial stage of lithiation is investigated in more depth. These researches can provide a better understanding of the electrochemical process Li-Si system for lithium-ion batteries using nanostructured Si, and may support an optimal design of nanostructured Si electrodes to increase the efficiency and cycle life of lithium-ion batteries.

### 3.1 Experimental

#### 3.1.1 Silicon nanowires (SiNWs) fabrication via MaCE method

Single crystal, n-type Si (100)-oriented wafers,  $525\ \mu\text{m}$  in thickness, with a resistivity in the range of  $1\text{--}5\ \Omega\cdot\text{cm}$  were used in this work. Highly ordered silicon nanowire arrays (SiNWs) were fabricated via the one-step MaCE method consisting of aqueous hydrofluoric acid (49% HF) and silver nitrate (0.1 M  $\text{AgNO}_3$ ) solutions in a 1:1 volume ration mixed at room temperature ( $\approx 25\ ^\circ\text{C}$ ). Following electroless etching, the species were treated in de-ionized (DI) water and then they were immersed in a nitric acid ( $\text{HNO}_3$ ) aqueous solution to dissolve the metallic silver dendrites from the SiNWs electrode. After that, the Si samples were rinsed with DI water and dried by nitrogen ( $\text{N}_2$ ) gas blowing. Lastly,

the wafer scale SiNWs were cut into small pieces of suitable size (dia. 10 mm) and dipped into diluted HF solution to remove the oxide and impurities.

**Fig. 3.1** shows the 4-inch Si wafer before and after the one-step MaCE method. The SiNWs are formed uniformly on the Si substrate, which changes color during the MaCE process. To further elucidate the SiNWs fabrication according to the different etching time, Si substrate is etched in the same amount of aqueous solution containing 49% HF and 0.1 M AgNO<sub>3</sub> (1:1 v/v) from 5 to 240 min.

By SEM observation, the SiNW lengths are obtained and plotted in **Fig. 3.2**. The Ag nanoparticle penetration depth increases linearly with time at a rate of about 1  $\mu\text{m}/\text{min}$  till about 50 min. After that, the etching velocity drops gradually by half (about 0.5  $\mu\text{m}/\text{min}$ ) after 60 min. It is probably due to the exhaustion of metal (Ag) catalyst in the etchant and the thick metal (Ag) layer on the top of SiNWs. Furthermore, the SiNWs growth rate of one-step MaCE is much faster than that of two-step MaCE (about 0.4  $\mu\text{m}/\text{min}$ ) [43]. The remnant of Si substrate can be etched when there is ample etchant during etching.

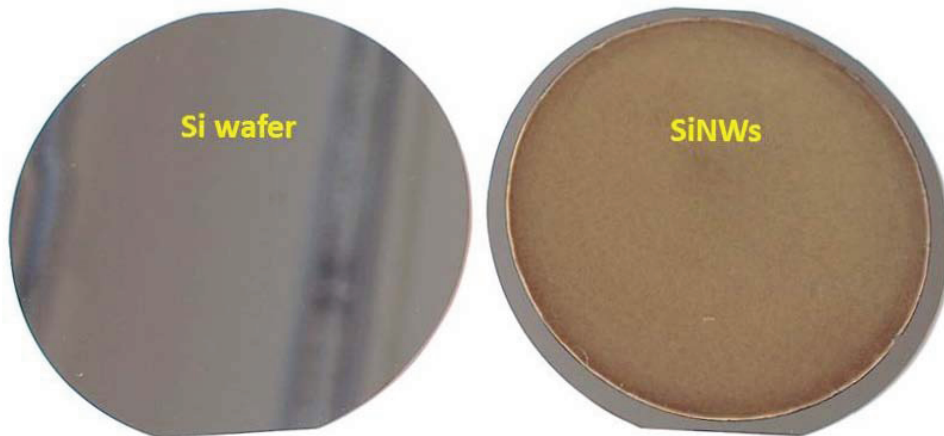


**Figure 3.1:** A photo with reflections of 4-inch Si wafer before and after one-step MaCE process.

### 3.1.2 Silicon nanowires (SiNWs) properties

The typical SEM images of SiNWs by the one-step MaCE method are shown in **Fig. 3.3(a)**, **(b)**, showing uniform long SiNWs. Sufficient free space between nanostructures for the large volume change during cycling is shown in **Fig. 3.3(a)**. Furthermore, **Fig. 3.3(b)** shows the cross-section details of the SiNWs: All SiNWs with a length of 28  $\mu\text{m}$  are distinguishable and most of them are vertically aligned on the Si substrate. The vertical direction of the SiNWs is (100), which is perpendicular to the original Si wafer surface used. As-prepared

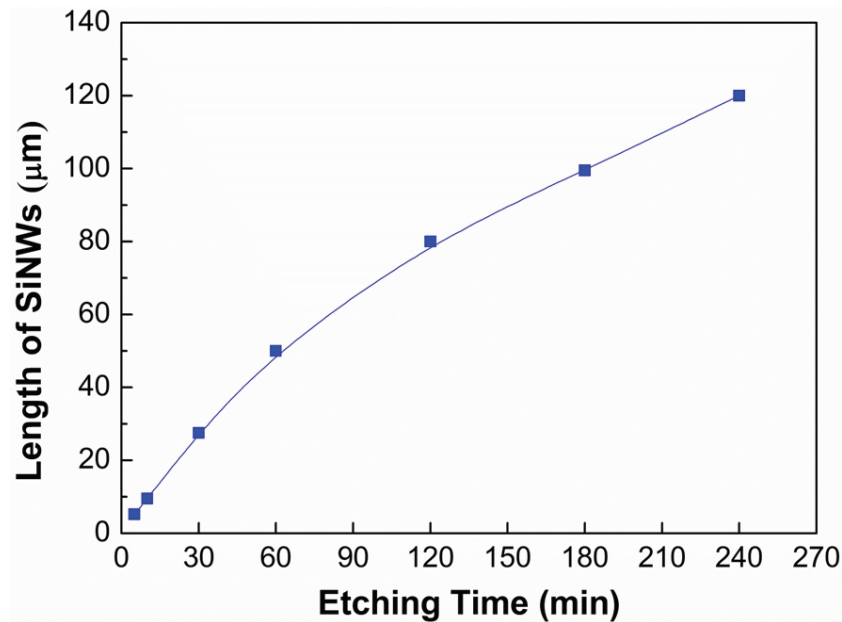


**Figure 3.2:** Fabricated SiNWs length versus etching time for n-type Si wafer. The etching is conducted in the same amount of aqueous solution in 48 % HF + 0.1 M AgNO<sub>3</sub> (1:1 v/v).

SiNWs are a component of the Si substrate and therefore have direct electric pathways via the Si substrate allowing efficient charge transport. As confirmed by TEM observation as shown in **Fig. 3.3(c)**, the surface of the SiNWs is somewhat rough and the diameters of the SiNWs range from 50 to 200 nm caused by the distribution of silver catalyst [65]. These nanowires are single crystalline, retain the electrical characteristics and crystallographic orientation of the original Si substrate.

The energy-dispersive X-ray spectroscopy (EDX) analysis of the SiNWs (see **Fig. 3.4(a)**) proves that the SiNWs are composed of Si with a small amount of oxygen, which is attributed to the surface oxidation covering the nanowires. The X-ray diffraction (XRD) pattern of the SiNWs is shown in **Fig. 3.4(b)**. It can be seen that the only peak at 69.82° attributed to the SiNWs is completely indexed as (400) of the standard cubic phase silicon, according to Ref. [66], which indicates the axes direction of the SiNWs has a preferred orientation of [100]. Furthermore, no diffraction peaks from SiO<sub>2</sub> or any impurities are detected, indicating the high purity of the as-prepared SiNWs electrode.

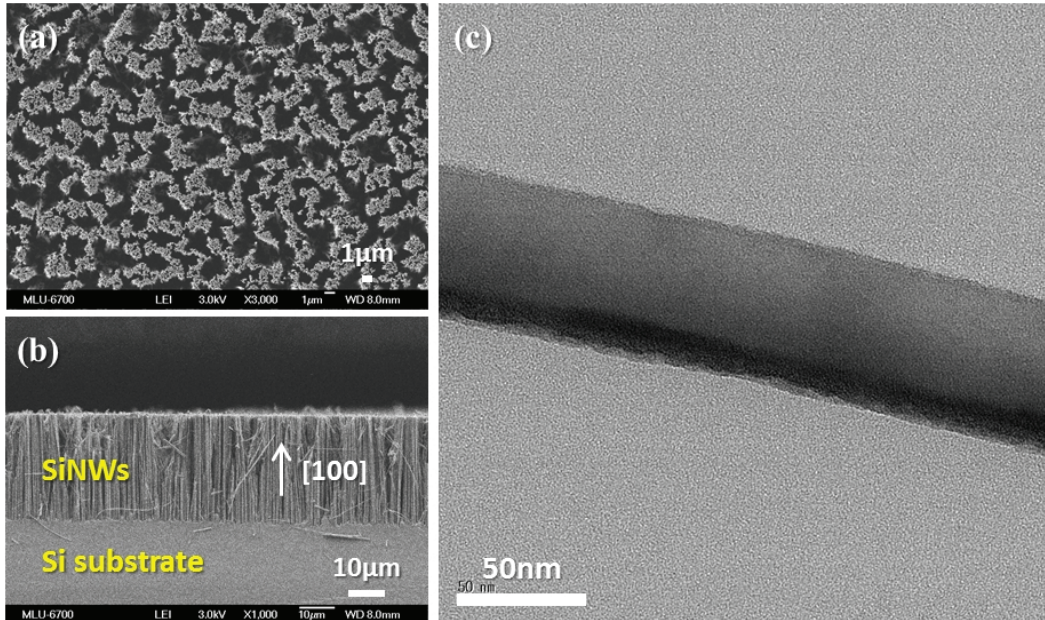


**Figure 3.3:** SEM images of silicon nanowire arrays (SiNWs) prepared via metal-assisted chemical etching, (a) top view and (b) cross-sectional view. (c) TEM image of a single silicon nanowire.

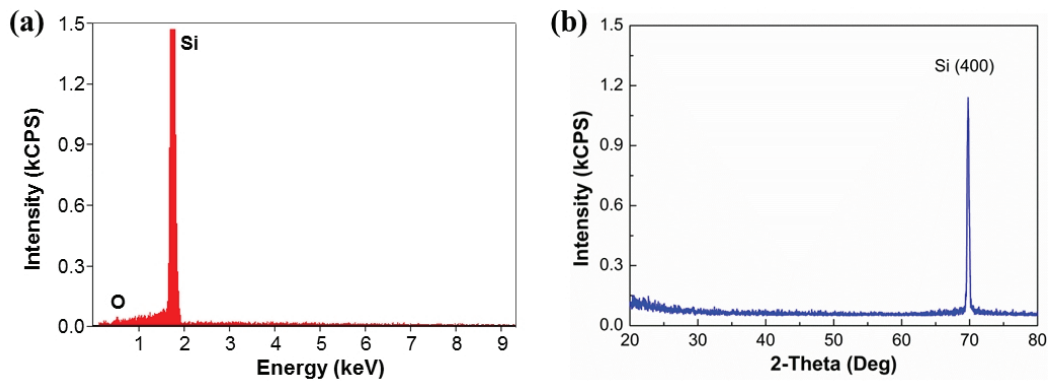


**Figure 3.4:** (a) EDX spectrum and (b) XRD patterns corresponding to as-prepared SiNWs.

## 3.2 Results and Discussion

### 3.2.1 Electrochemical investigation of SiNWs anodes

The SiNWs electrode on Si substrate is tested in a lithium-ion half-cell. A cyclic voltammogram (CV) of the SiNWs electrode in the potential range from 0.01 to 2.0 V (vs. Li/Li<sup>+</sup>) at a scan rate of 0.5 mVs<sup>-1</sup> is shown in **Fig. 3.5**. The first cycle profile has only one broad peak at about 0.6 V during the first discharging, which is associated with the formation of a solid/electrolyte interphase (SEI) on the surface of the SiNWs induced by the reduction of the electrolyte. In general, a SEI layer is considered to be formed during the first discharging in the potential range of 0.5–0.7 V [33]. Subsequent cycles do not show the same peak. Following the SEI formation, the redox pair peaks appear, which shows the phase transition of Li–Si phase upon Li insertion into and extraction from the crystalline Si, respectively. A big discharge current peak indicating a large double-layer capacity caused by the big surface area starts at 0.12 V and charge current peaks emerge at 0.35 and 0.52 V. Such redox behavior of the SiNWs electrode is consistent with lithiation/delithiation of microstructured Si electrodes due to the cycling rate, the electrolyte type, and the shape of SiNWs [28, 67, 68, 69]. The same redox peaks appear from the 1<sup>st</sup> cycle until the 50<sup>th</sup> cycle, reflecting that the same procedure takes place in all cycles. In addition, the increasing intensity of the redox peaks could be associated to the gradual activation of the SiNWs to react with lithium ions because CV profile meaning active surface area of SiNWs electrodes increases according to cycles.

The images of SiNWs electrode before and after CV experiment are shown in **Fig. 3.6**. The SiNW electrode clearly shows a transformation caused by the SEI formation and amorphization. To further elucidate the change of SiNWs electrode, the cycled SiNWs electrode is investigated by XRD analysis (see **Fig. 3.7(a)**). It can be seen that new peaks, (111), (220), (311), and (331), relating to new crystalline Si structures are detected. These crystalline Li-Si phases indicate the Li-trapping in silicon, leading to significant irreversible capacity loss even though original Si has a highest theoretical specific capacity. Through SEM observation, it confirms the deformation of SiNWs including the SEI formation caused by electrolyte decomposition, and structure transformation induced by amorphization (see **Fig. 3.7(b)**).

The SiNWs electrode is cycled in the potential range from 0.1 to 2.0 V (vs. Li/Li<sup>+</sup>) for 70 consecutive cycles at a current density of 50  $\mu\text{Acm}^{-2}$ . The lower cutoff voltage should be above 0.06 V to prevent the formation of the crystalline Li<sub>15</sub>Si<sub>4</sub> phase and to maintain the two-phase region composed of amorphous silicon and crystalline silicon [20, 70, 71]. The discharge/charge profiles for the SiNWs electrode are shown in **Fig. 3.8(a)** from the first cycle until the fifth cycle. The SiNWs electrode provides a capacity of 636.5  $\mu\text{Ahcm}^{-2}$  during the first discharge and had a charge capacity of 304.0  $\mu\text{Ahcm}^{-2}$  with an initial coulombic efficiency of 47.8%. This high irreversible capacity loss of 52.2%



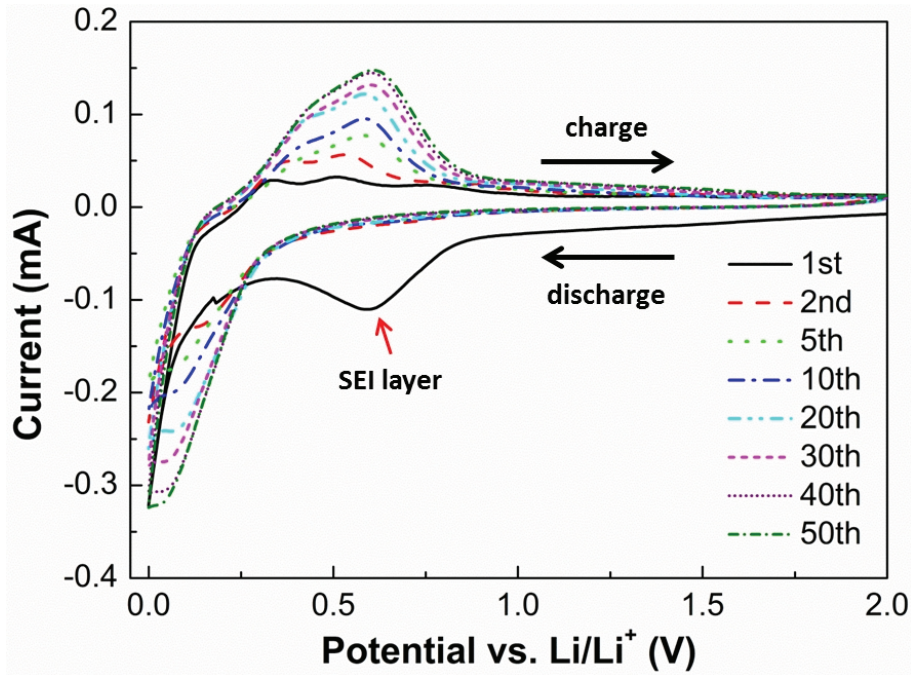


**Figure 3.5:** Cyclic voltammogram for the SiNWs electrode between 2.0 and 0.01 V (vs.  $\text{Li/Li}^+$ ) at a scan rate of  $0.5 \text{ mVs}^{-1}$ .

in the first cycle may be mainly due to the formation of a SEI layer on the surface of SiNWs electrode, resulting in the irreversible lithium insertion into the crystalline SiNWs. The discharge/charge capacity versus cycle number for the SiNWs electrode is shown in **Fig 3.8(b)**. It is observed that the discharge capacity of the SiNWs electrode drops drastically within a few cycles. However, after the initial capacity drop, the capacity profile is comparatively stable with a high coulombic efficiency, confirming that the initial lithiation/delithiation cycles play a major role in the following or overall cycle performance of Si electrode.

The cycled SiNWs electrodes are investigated in order to understand the

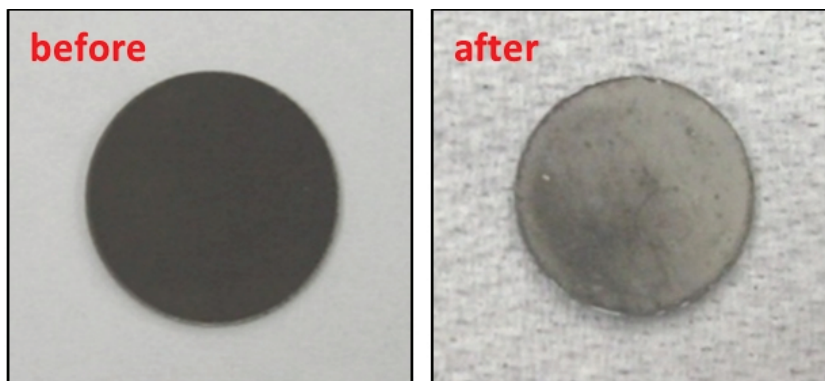


**Figure 3.6:** Photograph of the SiNWs electrode before and after CV experiments.

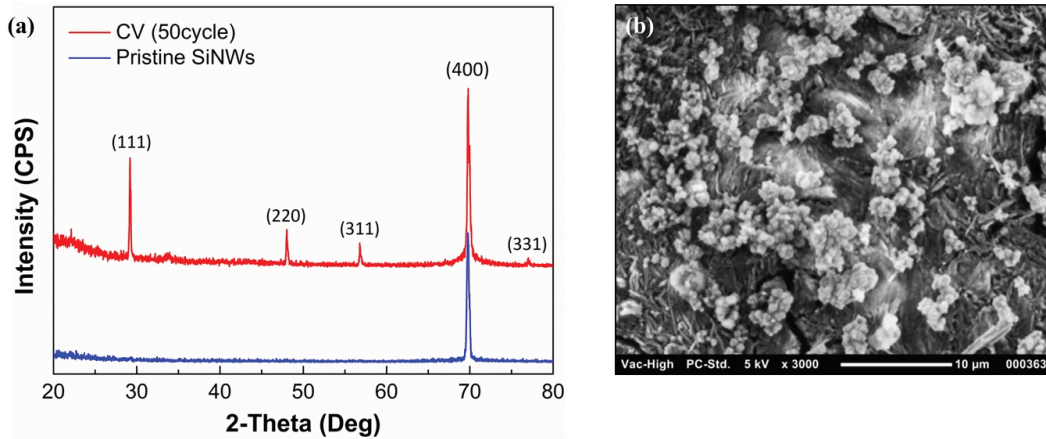


**Figure 3.7:** (a) XRD patterns comparison before and after CV experiment and (b) top-view SEM image measured for the cycled SiNWs electrode.

transformation of the morphology of SiNWs through cycling. **Fig. 3.9** shows SEM images of a SiNWs electrode after 70 cycles. It is observed that most SiNWs retains much of the original structure in spite of the repetitive large volume change during lithiation/delithiation cycles. Moreover, the thick SEI layer is formed mostly on top of SiNWs in comparison with the middle and bottom region of SiNWs (see **Fig. 3.9(b)**). Basically, Li-ions would be incorporated into the Si substrate, leading to local fracture and failure during cycles. **Fig. 3.9(c)**, however, shows that Si substrate is not involved in lithiation/delithiation. One possible reason is the limited penetration of the viscous electrolyte into long Si nanostructures, despite the strong capillary effect [68]. Consequently, the available surface of the long Si nanostructure is only partially active.

This is confirmed by TEM observations. **Fig. 3.10** shows the TEM images of the cycled SiNWs electrode (after charging to 2.0 V). It shows that the cycled SiNWs electrode is comprised of virtually non-transformed crystalline SiNWs despite continuative cycles (see **Fig. 3.10(a)**) and totally transformed amorphous SiNWs as indicated by the amorphous rings in the SAED (see **Fig. 3.10(b)**). It suggests that only a part of the pristine SiNWs of the electrode do react with lithium ions during lithiation/delithiation cycles. This means that the surface charge of individual SiNWs is clearly different. One possible reason is the various degrees of individual SiNWs dimensions. But this is not the case for our electrodes: All SiNWs have a similar diameter around 100 nm. Actually, we have figured out an approximate distribution profile of cycled SiNWs in TEM sampling. The amount of changed SiNWs is about 60%. That is because the LiSi phase is usually formed by lithium ion transfer to the stronger electric charged regions of nanowires at the initial stage of lithiation. Thus, the formation of the LiSi phase is different depending on the surface charge distribution in the individual SiNWs. At the initially lithiation, the reaction between lithium ions and silicon is not only limited to a thin layer

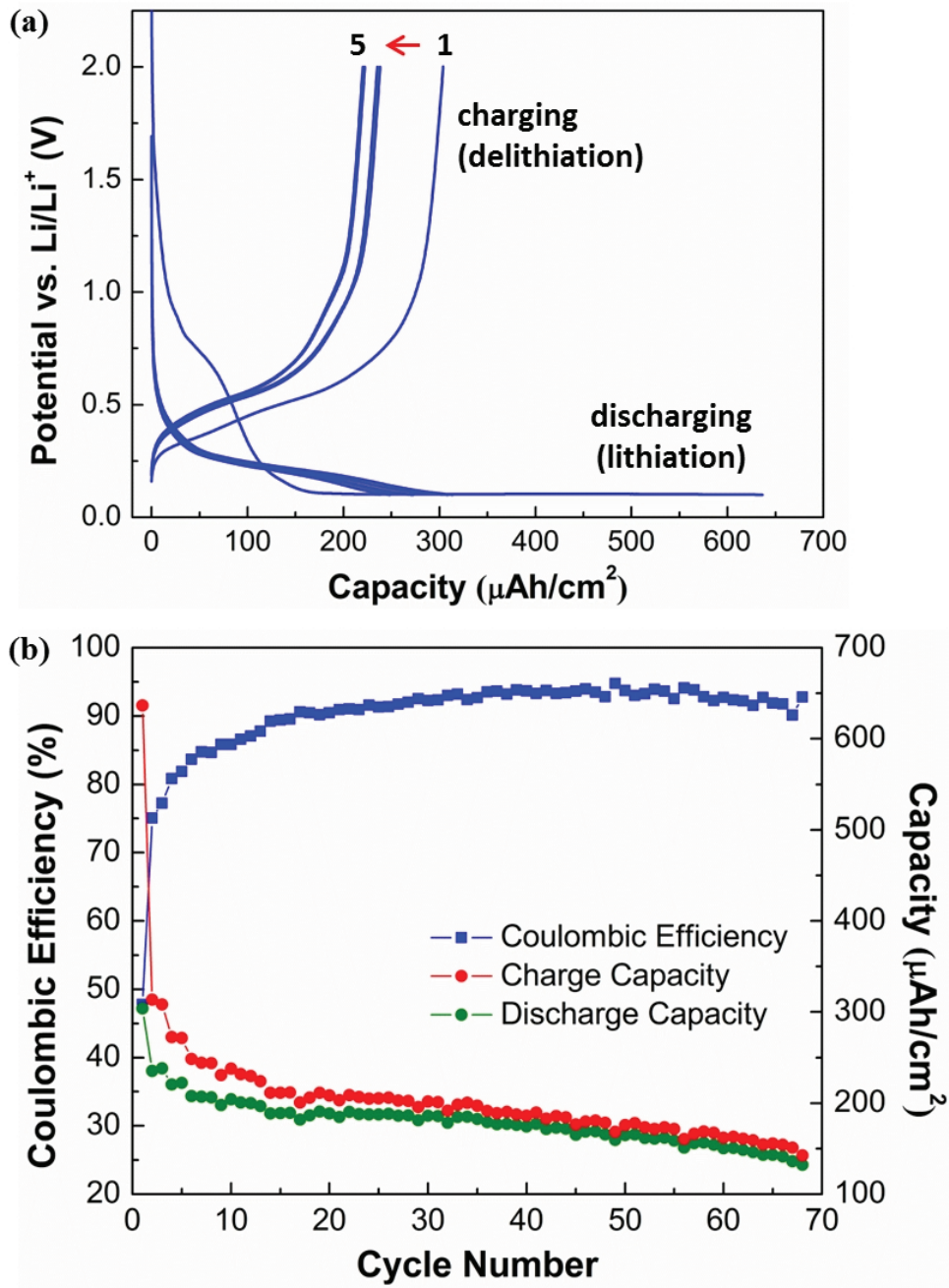


**Figure 3.8:** (a) Galvanostatic charge/discharge profile of the SiNWs electrode between 0.1 and 2.0 V (vs.  $\text{Li/Li}^+$ ) at a constant current density of  $50 \mu\text{A}/\text{cm}^2$ . (b) Plot of coulombic efficiency and charge/discharge capacity of the cell vs. cycle number for the SiNWs electrode.



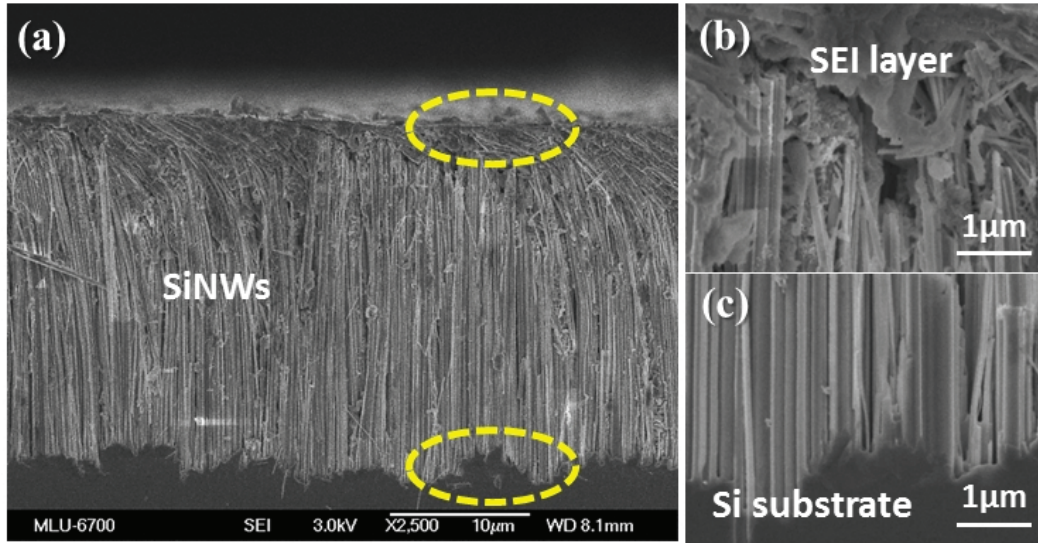


**Figure 3.9:** (a) SEM images of the SiNWs electrode after 70 cycles (the cell was delithiated to 2.0 V). High-resolution SEM images of (b) top and (c) bottom of the SiNWs corresponding to (a).

induced by the lithium diffusion near the electrolyte interface but also limited by the electrons provided from crystalline SiNWs core. Upon the subsequent lithiation, Li-ions prefer amorphous Si instead of crystalline Si to form the Li–Si phase, probably because of the homogeneous volume expansion and higher reactive potential ( $\approx 220$  mV) of amorphous Si [18, 72, 73].

This means a significantly diminution of the available surface area of cycled SiNWs in spite of its original large surface area. Consequentially, the cyclability of SiNWs electrode is in fact determined at the initial lithiation/delithiation cycles depending on how much crystalline Si could be converted into amorphous Si. In addition, the structural deformation of cycled SiNWs consisting of amorphous and crystalline Si is much less intense, and only a little fragmentation is observed despite the progressive volume change.

### 3.2.2 Lithium intercalation in individual SiNWs

In the interest of observing the formation of Li–Si phase, the morphology change of individual SiNWs at the first cycle is investigated because the first lithiation in individual SiNWs plays a quite important role in Li–Si cells as mentioned above. The first discharge/charge profile of the SiNWs electrode lithiated at a low constant current density is shown in **Fig. 3.11**. The electrode is lithiated at  $25 \mu\text{Acm}^{-2}$  for 25 h to ensure the complete reaction between the lithium ions and all SiNWs on the electrode, followed by delithiation at the same flux to the upper limit potential of 2.0 V (vs. Li/Li<sup>+</sup>). During discharging (lithiation), a peak of SEI formation is detected at the potential of about 0.6 V

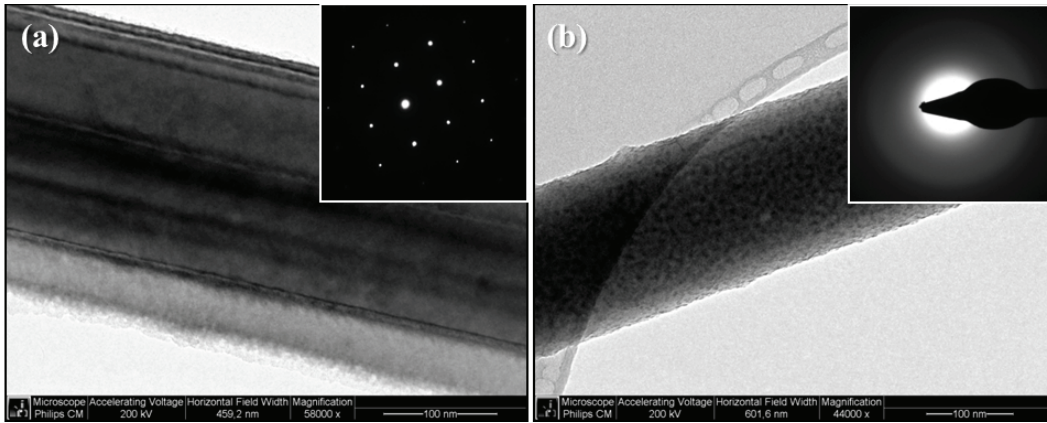


**Figure 3.10:** TEM images of the SiNW electrode after 70 cycles (the cell was delithiated to 2.0 V). (a) non-transformed SiNW, (b) totally transformed SiNW. The corresponding SAED patterns are shown in the insert of the figures.

(see **Fig. 3.5**), and the first lithiation of silicon begins at 0.15 V after about 4 h. Subsequently, a voltage plateau at about 0.1 V appears, which corresponds to the alloying of lithium ions with SiNWs. After the first discharging, the subsequent charge process (delithiation) is taking place in the linear regime of 0.3–0.5 V, reflecting the de-alloying of lithium ions from SiNWs. The SiNWs electrode provides an initial coulomb efficiency of 67.2% at the first cycle.

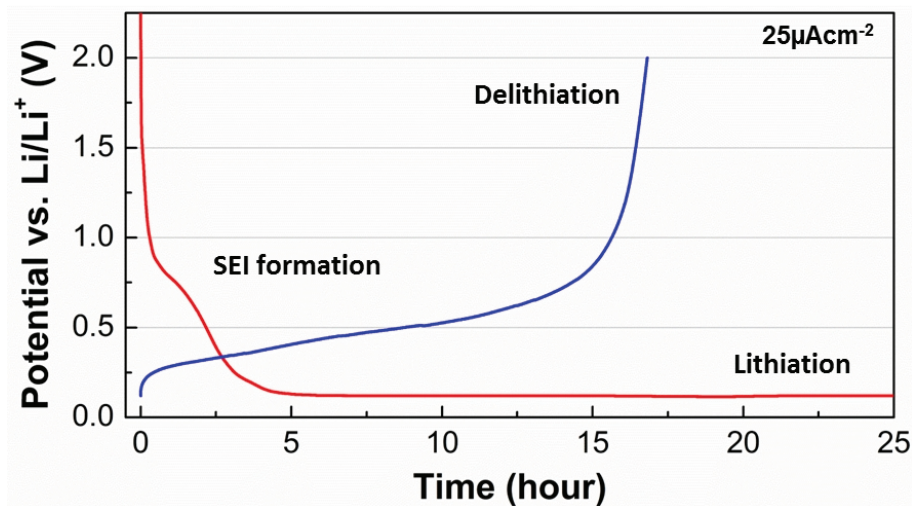


**Figure 3.11:** Voltage profile as a function of time during lithiation (discharging) and delithiation (charging) of the SiNWs electrode at the first cycle with low constant current density ( $25 \mu Acm^{-2}$ ).

**Fig. 3.12(a)** shows a TEM image of a single SiNW at the end of lithiation. In comparison with an as-prepared single SiNW (see **Fig. 3.3(c)**), the morphology becomes clearly rough, most likely due to the amorphization induced by volume expansion after lithium insertion. **Fig. 3.12(b)** shows a high-resolution TEM image of the SiNW sidewall corresponding to **Fig. 3.12(a)**. It is noted that the crystalline Si of the sidewalls is converted into an amorphous lithiated phase of about 10 nm in thickness, resulting in the revelation of obvious phase boundary between crystalline and amorphous phase as well. It also confirms that the phase transition takes place at different rates of reaction near the electrolyte interface due to the different surface charge of SiNWs, even if the lithium injection into silicon is constant. Thus, the lithiated SiNWs are composed of a crystalline Si core and an amorphous Li–Si alloy shell with various thicknesses. Consequently, the initial surface charge distribution would determine the formation of Li–Si phase related to overall cycle performance, involving previous studies [74].

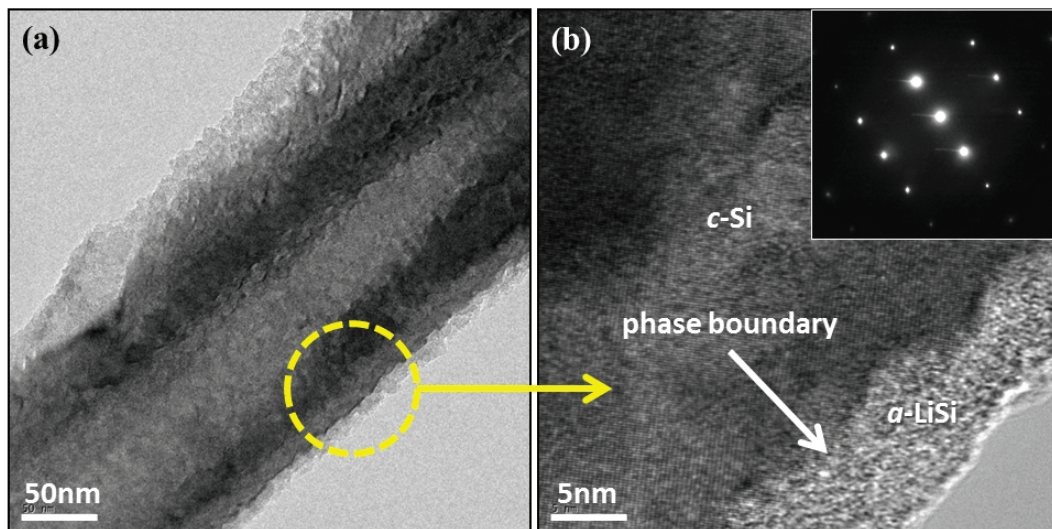


**Figure 3.12:** (a) TEM images of lithiated single SiNW. (b) High-resolution TEM image of the sidewall on lithiated single SiNW. The corresponding SAED pattern in c-Si regime is shown in the insert of the figure.

In order to figure out the surface reaction during the first lithiation/delithiation, the surface composition of SiNWs electrode is determined using X-ray diffraction (XPS) analysis. As shown in **Fig. 3.13**, the high-resolution spectra for the C (1s), Si (2p), O (1s), Li (1s) and F (1s) peaks are investigated concerning lithiated and delithiated SiNWs compared to pristine SiNWs, respectively.

In general, the SEI layer on silicon electrode is considerably different from thin layers typically formed on carbon electrodes. The main reason is that the silicon surface has vigorous reaction to electrolyte than carbon, resulting in the formation of a multi-compound SEI compound. The C (1s) spectra show increased peaks at lithiation/delithiation stages. In particular, the peaks of O–C=O at 289.9 eV increase significantly in comparison with pristine SiNWs, probably due to the formation of a SEI. For such a reason, the Si (2p) and O (1s) spectra of lithiated SiNWs decrease significantly, indicating that SiNWs surface is covered by the SEI.

In addition, fluoride has derived from electrolyte reduction such as  $\text{PF}_6^-$ , which causes formation of silicon fluorides. The Li (1s) and F (1s) spectra prove the production of LiF or other fluorinated species. These results may lead to irreversible reactions with fluorine and thus a capacity fading. And finally, such an electrolyte decomposition reaction leads to a higher the consumption of Li ions and a higher production of silicon compound. This hinders the Li ions transport, resulting in further capacity fading.



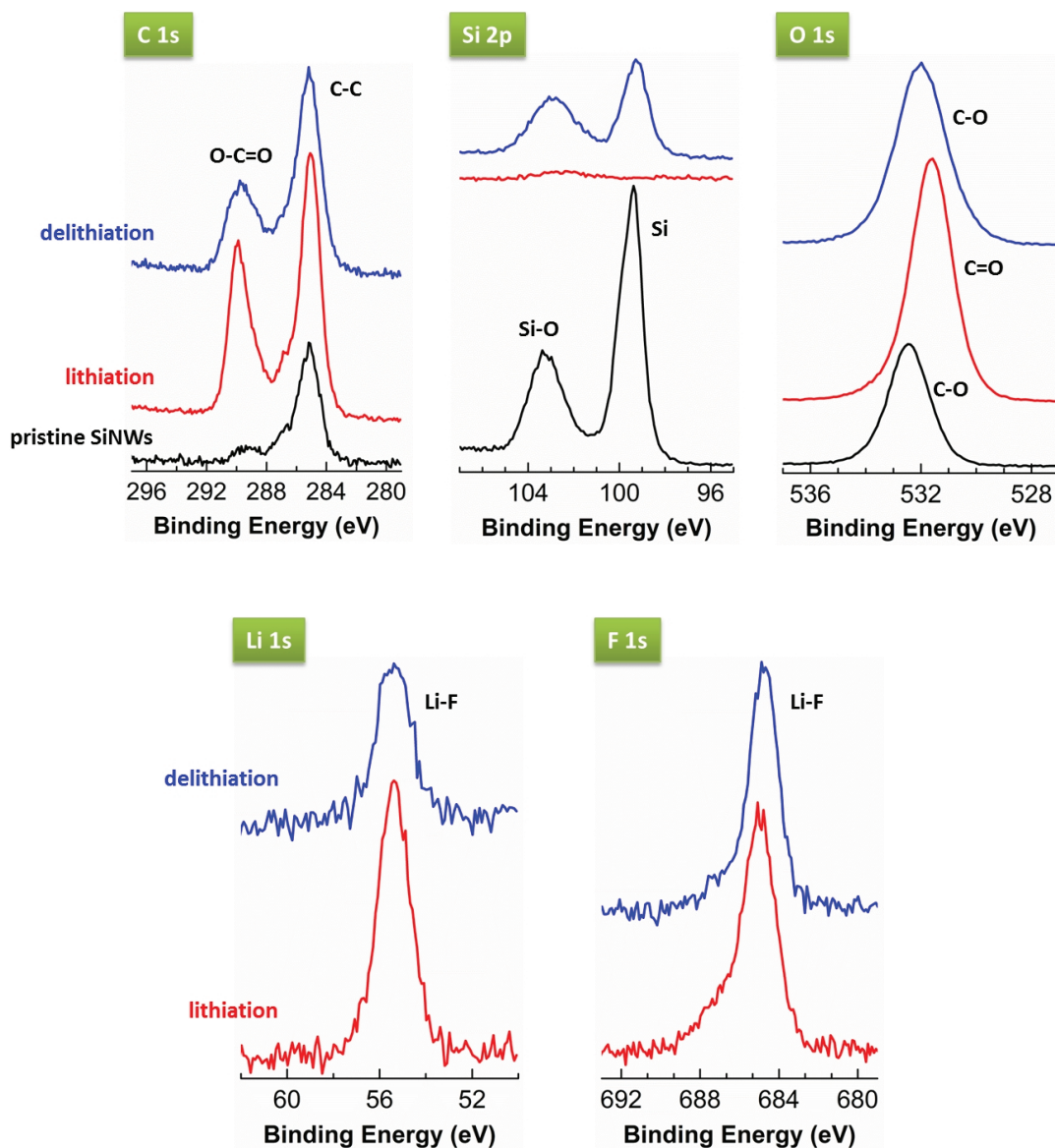


**Figure 3.13:** High-resolution X-ray photoelectron spectroscopy (XPS) spectra of SiNWs electrodes at the lithiation/delithiation stages of the first cycle compared with a pristine SiNWs electrode. All electrodes were exposed to ambient conditions for about 10 min.

**Table 3.1:** Comparison of XRD spectra peak positions (eV) of C, Si, O, Li and F of pristine, lithiated and delithiated SiNWs at the first cycle, respectively.

	C 1s	Si 2p	O 1s	Li 1s	F 1s
pristine SiNWs	285.16	99.38 / 103.38	532.45	—	—
Lithiation	285.05 / 289.88	—	531.61	55.39	684.77
Delithiation	285.18 / 289.78	99.28 / 103.08	532.01	55.40	685.01

The lithiation at the high C-rate is investigated as well. **Fig. 3.14(a)** shows a TEM image of a lithiated single SiNW after the SEI layer is removed by dissolution in acetonitrile. Lithiation experiment is performed at a higher constant current density of  $100 \mu\text{Acm}^{-2}$  for 24 h. A similar phenomenon is detected as in the previous lithiation experiment at low current density: The sidewall morphology of lithiated SiNW becomes rather rough and its volume is expanded. Furthermore, a thick amorphous lithiated phase of 20–40 nm is formed. The bonding state and chemical composition of the lithiated single nanowire are investigated by electron energy loss spectroscopy (EELS) in **Fig. 3.14(b)**. The detected peaks are situated around 56.5 and 101 eV, indicating the presence of Li and Si, respectively. The EELS spectra show that the Li *K*-edge comes out remarkably around 56 eV and then the Si *L*<sub>2,3</sub>-edge diminishes (onset at  $\approx 99$  eV) [75].

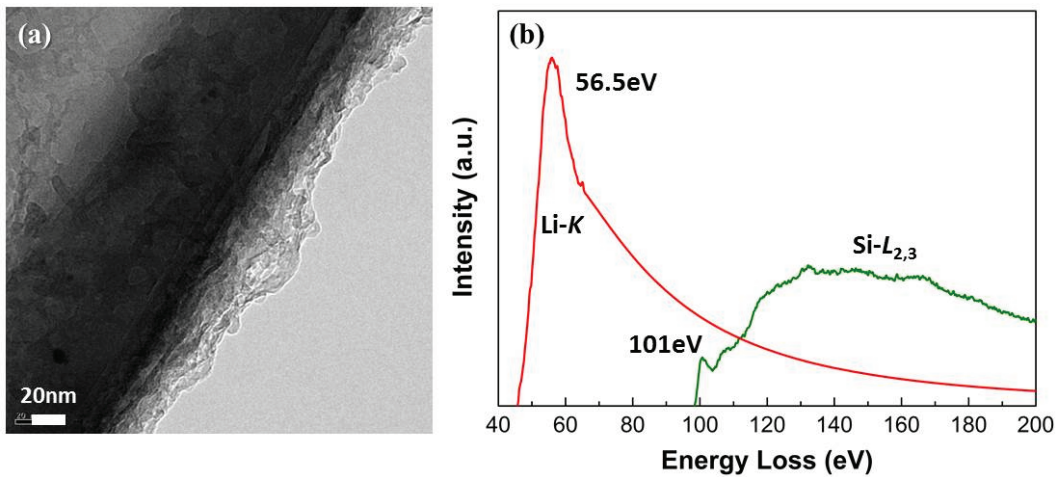


**Figure 3.14:** (a) TEM image of the lithiated SiNW at a constant current density of  $100 \mu\text{Acm}^{-2}$ . (b) EELS spectra corresponding to (a).

The results are consistent with the high-angle annular dark-field scanning transmission electron microscopy (HAADF-STEM) image of the lithiated SiNW as shown in **Fig. 3.15(a)**. This clearly shows that an untransformed crystalline silicon core in the central bright region is surrounded by the lithiated amorphous silicon shell in the outer wing of the lithiated SiNW. This is probably due to deficient electron transport through the Li–Si alloy shell or poor electrical conductivity of the crystalline Si core induced by the charge starvation on the surface of the SiNW [76, 77]. **Fig. 3.15(b)** shows an EELS spectrum at the edge and core of the lithiated SiNW corresponding to **Fig. 3.15(a)**.

At the core of the lithiated SiNW, a strong peak of Si  $L_{2,3}$ -edge at 99.5 eV is detected, followed by a broadened region. The EELS spectrum obtained at the edge of lithiated SiNW (Li–Si alloy shell) includes elemental silicon peaks at 99.2 and 107.7 eV, referring to Si and  $\text{SiO}_x$ , respectively. Moreover, another two resonances are lightly present at 110.7 and 119.5 eV marked by ( $\downarrow$ ). The amorphous  $\text{SiO}_x$  can be essentially described by the characteristic of the spectrum from the near edge of  $\text{SiO}_2$  [78]. This indicates that the Li–Si alloy shell is a mixture of amorphous and crystalline Si. This amorphous  $\text{SiO}_2$  phase in the outer wing could gradually interrupt the lithium ions movement and electron transport during cycles. Therefore, the formation of Li–Si alloy is hindered, leading to a fast capacity fading and a poor cycle life [79]. The EELS studies at the high C-rate also confirm that the lithiated SiNWs are composed of a crystalline Si core and an amorphous lithiated Si. In particular, Li–Si alloy shell contains a certain amount of amorphous silicon oxide. However, the exact amorphous/crystalline silicon ratio in the Li–Si phase is not known during the first lithiation because the detail atomic structure could not be obtained from the amorphous phase. Therefore, the understanding of their mechanical stress and phase transition will require further work and discussion of the lithiation reaction in the silicon.

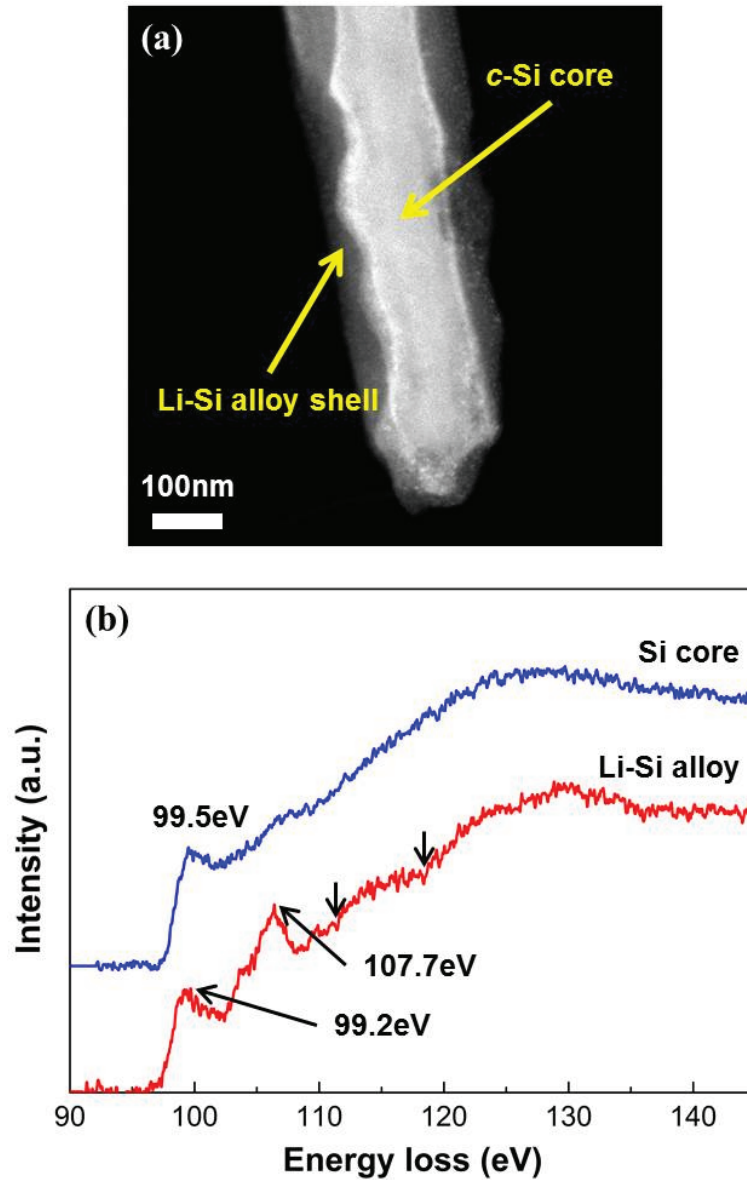


**Figure 3.15:** (a) High angle annular dark field scanning transmission electron microscopy (HAADF-STEM) image of the lithiated SiNW. (b) Electron energy loss spectra (EELS) obtained at edge and center corresponding to (a).



### 3.3 Summary

In this chapter, the experimental studies on lithium-ion battery applications were shown using the SiNWs electrode prepared via direct metal-assisted chemical etching of silicon wafer. The observation shows that the SiNWs electrode, having good conductivity and large surface area, can maintain its structure during the Li–insertion and extraction processes. However, it does not reach the high theoretical specific capacity of silicon material during long-term charge/discharge cycles. Only part of as-prepared SiNWs was transformed into amorphous SiNWs after continuative cycles, resulting from the different surface charge distribution in the individual SiNWs. Therefore, all SiNWs of the electrode should be activated to increase the specific capacity and cycling stability. Consequently, a silicon anode should be of nano-size structure, but also have the uniform surface charge distribution to achieve performance enhancement. By doing this, it would lead to better transport and electrical conductivity between lithium ion and silicon structure.

In addition, the lithiation and delithiation process was analyzed in detail by high-resolution electron microscopy. By TEM observation with EELS analysis, the morphology change and the chemical composition of individual SiNWs were identified during the lithiation process. The SiNWs obtained an amorphous lithiated silicon shell, yet their core still remains crystalline. Also the Li–Si alloy shell of the nanowire was analyzed, which is a mixture of crystalline Si and amorphous SiO<sub>2</sub>. This composition might lead to constraints in Li–Si alloy formation and limit the cycling performance. Non-cylindrical nanostructures like mesoporous nanowires might be a better design as recently suggested in literature. These results confirm that a uniform surface charge distribution on reactive layers is needed to enhance the specific capacity and cycle life during Li insertion.

# Chapter 4

## Nanostructured Black Silicon (b-Si) as Anode Material

In this chapter, the focus is on the nanostructured Si as an anode material for lithium-ion batteries produced for the first time by inductively coupled plasma reactive ion etching (ICP-RIE) of Si wafers with a black silicon (b-Si) surface. The microscopic structure strongly resembles other types of nanostructured silicon, with a well-arranged nanostructure possessing a sufficient porosity for accommodating large volume expansions. In Section 4.1, the fabrication of b-Si electrode via ICP-RIE technique is shown and the characteristic of the b-Si structure is illustrated. Afterwards, the structural and electrochemical properties of b-Si electrode according to surface condition are investigated. In addition, the fast lithiation is demonstrated before and after surface treatment in Section 4.2. These results can explain the function of surface properties and the interrelation between high current rate and failure of cycle life, which could improve the understanding of the substantive lithium reaction mechanism in nanostructured Si anodes.

### 4.1 Experimental

#### 4.1.1 Nanostructured black silicon (b-Si) fabrication via ICP-RIE technique

The Si substrate used in this work was a single-crystal n-type Si (100) wafer,  $525 \pm 25 \mu\text{m}$  in thickness with a resistivity of  $1-5 \Omega\cdot\text{cm}$ . Nanostructured black silicon (b-Si) was fabricated via ICP-RIE using gas mixtures comprising  $\text{SiF}_6$  as the etching gas and  $\text{C}_4\text{F}_8$  as the deposition gas. I prepared three b-Si electrodes with a length of 5, 10 and  $25 \mu\text{m}$ , respectively. Thereupon, the wafer-scale b-Si was cut into small pieces of suitable size and cleaned to remove oxides and impurities using a dilute hydrofluoric solution.

**Fig. 4.1** shows the 4-inch Si wafer after ICP-RIE. The nanostructured Si region shows clearly a color change. Nanostructured Si was formed evenly on the Si substrate (see **Fig. 4.1(b)**).

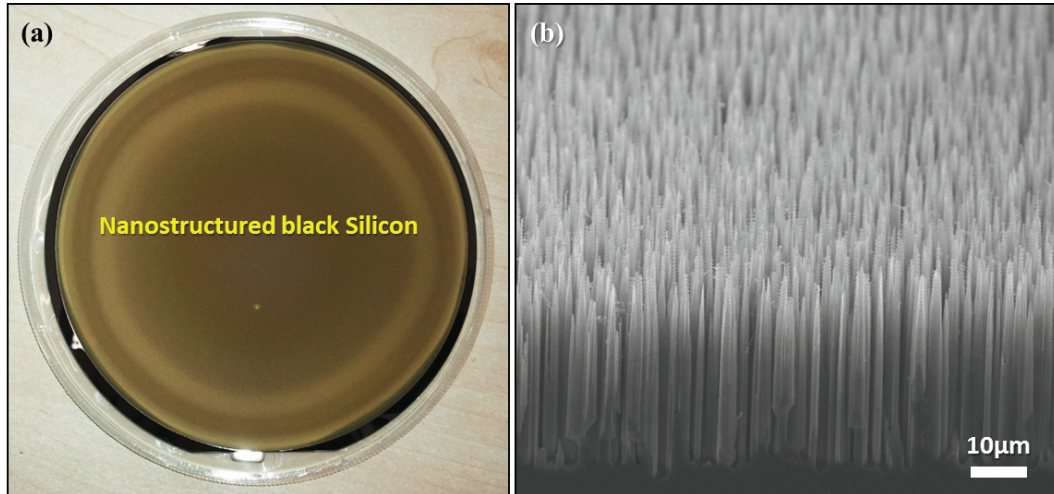


**Figure 4.1:** (a) Photograph of a 4-inch Si wafer and (b) SEM image corresponding to the nanostructured black silicon (b-Si) produced by ICP-RIE etching technique.

#### 4.1.2 Nanostructured black silicon (b-Si) properties

**Fig. 4.2** shows a typical SEM image of the pristine b-Si prepared by the ICP-RIE technique. The used Si nanostructures have three different geometries:  $5\ \mu\text{m}$  in length and about 300 nm in diameter,  $10\ \mu\text{m}$  in length and about 450 nm in diameter, and  $25\ \mu\text{m}$  in length and about 730 nm in diameter, respectively. The randomness observed in the nanostructure diameter may be induced by the repeated short deposition and etch steps, leading to the somewhat indented surface of the b-Si (see **Fig. 4.2(b)**) [59]. The Si nanostructures are well separated from each other in morphologies that are vertically aligned and fairly straight. This is expected that the morphology of the b-Si will create an improvement in the battery cycle performance owing to its sufficient free space to accommodate the volume expansion/contraction that occurs during lithium insertion/extraction. More importantly, one of the advantages of using Si nanostructures is to have large surface areas that will be able to react further with lithium ions in the battery system.

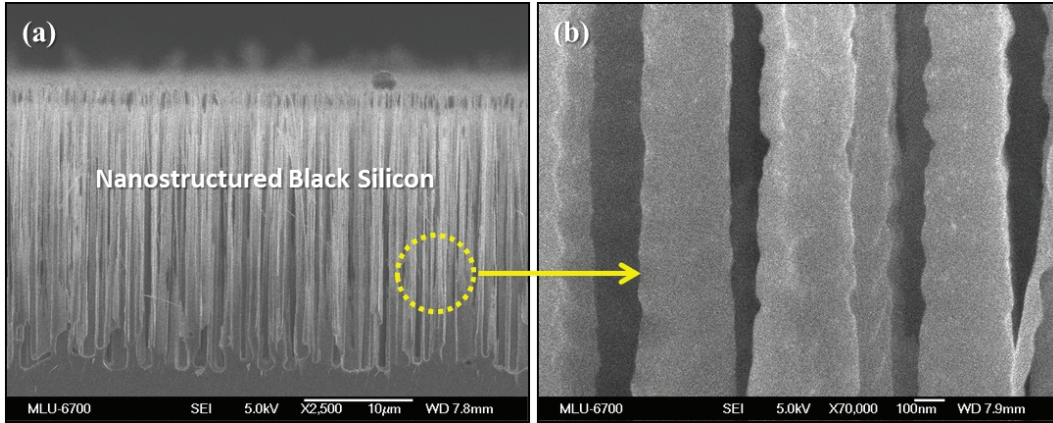


**Figure 4.2:** SEM images of nanostructured black silicon (b-Si) prepared by ICP-RIE technique.

## 4.2 Results and Discussion

### 4.2.1 Electrochemical measurements of b-Si anodes

**Fig. 4.3** shows the cyclic voltammetry profiles of the pristine b-Si electrode in the potential range from 0.01 to 2.0 V at a scan rate of  $0.5 \text{ mV s}^{-1}$  for seven different cycles. Generally, the solid-electrolyte interphase (SEI) is formed during the first discharge cycle in the potential range of 0.5–0.7 V [33]. But no peak in the profile indicating this formation on the pristine b-Si electrode is observed in this potential range, probably because the electrolyte decomposition does not occur or is insignificant on the surface of the pristine b-Si electrode during the initial cycle. It can be seen that the discharge current peak, indicating the formation of the Li–Si phase, increases drastically for the first 20 cycles. Similarly, the charge current peak, indicating the transition between Li–Si phase and amorphous Si, increases and then decreases after the 20 cycles, which suggests that the active surface area begins to diminish after the 20<sup>th</sup> cycle. This diminishment is probably because the b-Si electrode is influenced by a side reaction, such as considerable electrolyte decomposition. This redox behavior of the b-Si electrode is not consistent with previous studies observing the lithium alloying/dealloying process of micro/nano-structured Si electrodes [68, 80, 81]. The observed redox phenomenon in this study may be attributed to the influence of the electrolyte contact with the b-Si electrode upon its surface condition.

The initial galvanostatic charge/discharge curves of the pristine b-Si electrode from the 1<sup>st</sup> to the 10<sup>th</sup> cycle are shown in **Fig. 4.4**. The lower cut-off voltage is kept above 0.06 V (vs. Li/Li<sup>+</sup>) to avoid the crystallization of the Li<sub>15</sub>Si<sub>4</sub> phase [20], but still allowing a two-phase coexistence composed of amorphous Li<sub>x</sub>Si and amorphous Si. Therefore, the b-Si electrode is cycled in the potential range from 0.07 to 2.0 V (vs. Li/Li<sup>+</sup>) at a constant current

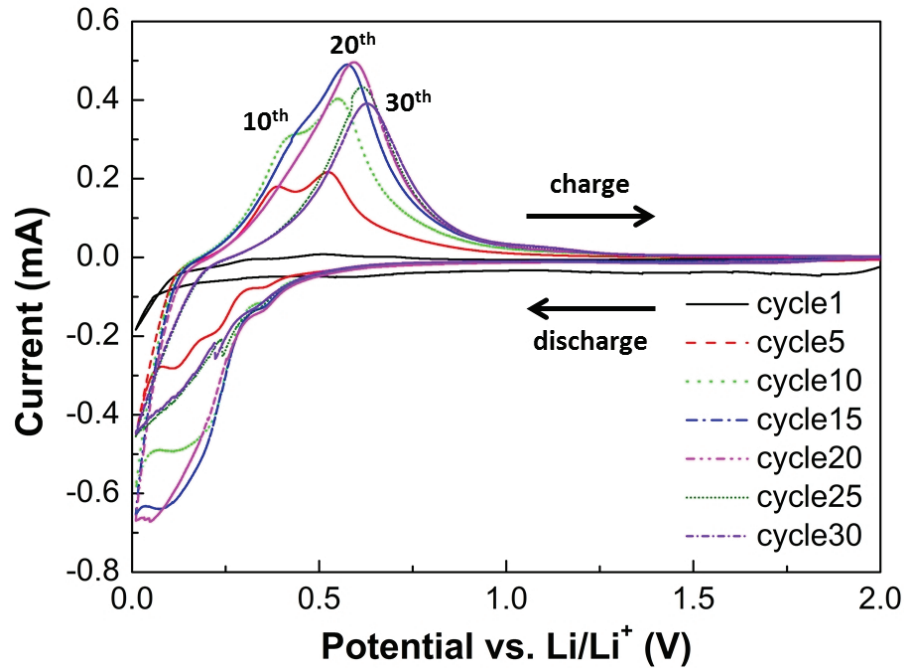


**Figure 4.3:** Cyclic voltammogram for the pristine b-Si electrode from 2.0 to 0.01 V (vs. Li/Li<sup>+</sup>) at scan rate of  $0.5 \text{ mVs}^{-1}$ .

density of  $80 \mu\text{Acm}^{-2}$ . With increasing length of the b-Si, the first discharge capacities of the 5, 10 and 25  $\mu\text{m}$ -long b-Si increases significantly, reaching 206, 1,170 and 5,730  $\mu\text{Ahcm}^{-2}$ , respectively. This can be explained by the nonlinearly increasing active surface area. However, the first coulombic efficiencies of the shorter b-Si (5 and 10  $\mu\text{m}$  lengths) are quite low, with values of 20.0 and 23.9%, respectively, although that of the 25  $\mu\text{m}$ -long b-Si electrode is 68.4%. The high first-cycle irreversible capacity loss may be related to the length of b-Si. If the vertical length of b-Si is small the coulombic efficiency becomes quite low, though the reaction between lithium ions and silicon is likely stronger. This confirms that the coulombic efficiency is more influenced by the state of the surface condition than by the structure shape. For the same reason, a negligible peak for SEI formation is observed at the first discharging on each b-Si electrode.

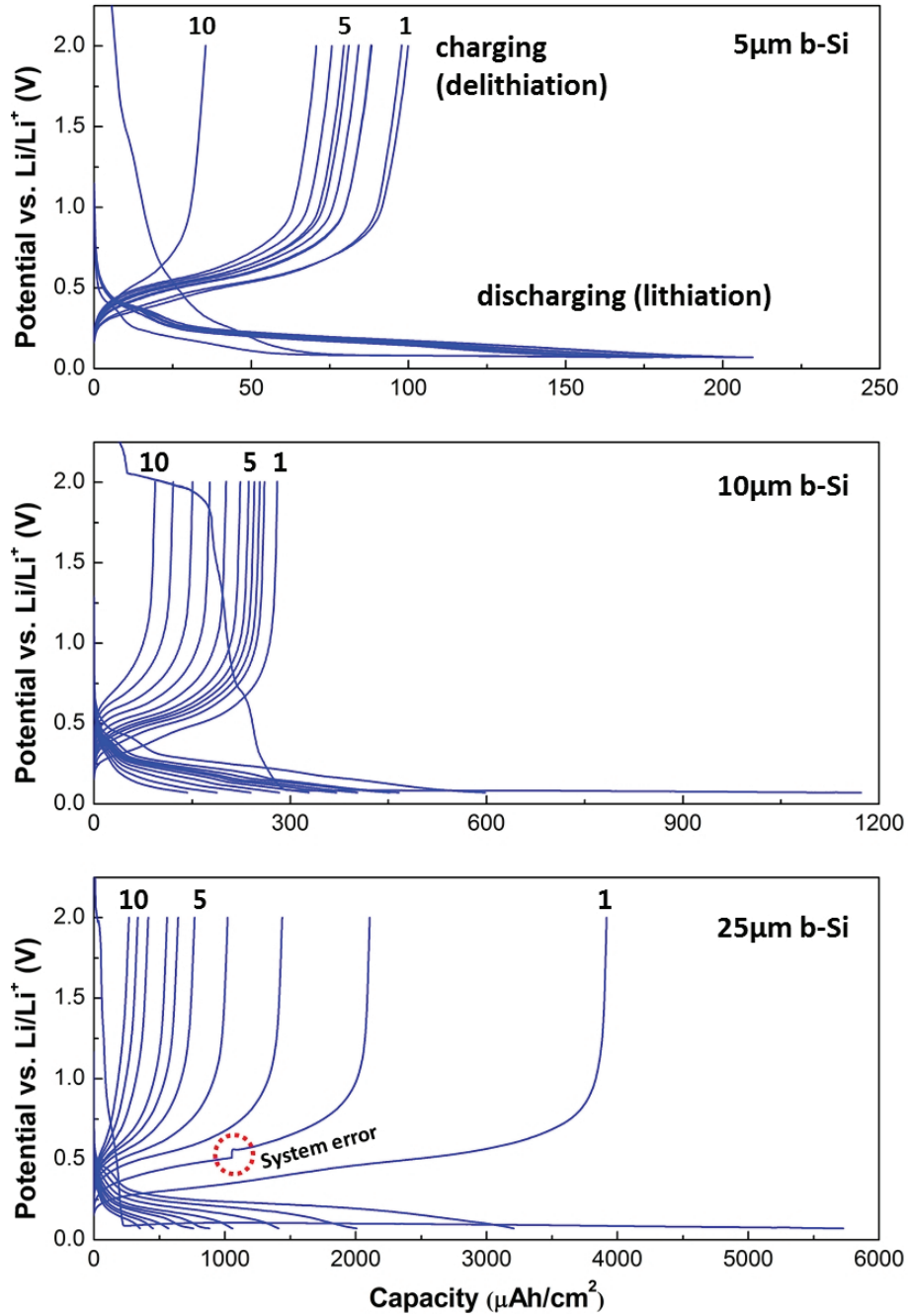


**Figure 4.4:** Initial galvanostatic charge/discharge curve of the pristine b-Si electrode with a length of 5, 10 and 25 μm at a constant current density of  $80 \mu A cm^{-2}$ .



**Fig. 4.5** compares the surface morphology change between lithiated and delithiated b-Si electrodes at the first cycle. **Fig. 4.5(a)** shows that the surface morphology becomes smooth and the nanostructure swells in volume after Li-insertion, probably owing to the amorphization on the nanostructure surface. As shown in **Fig. 4.5(b)**, the surface morphology becomes rough and the nanostructure volume decreases after Li-extraction. Consequentially, such a morphology change observation shows that the b-Si electrode has reacted definitely to lithium ions, and b-Si electrodes could be used a candidate for anode material in lithium-ion batteries.

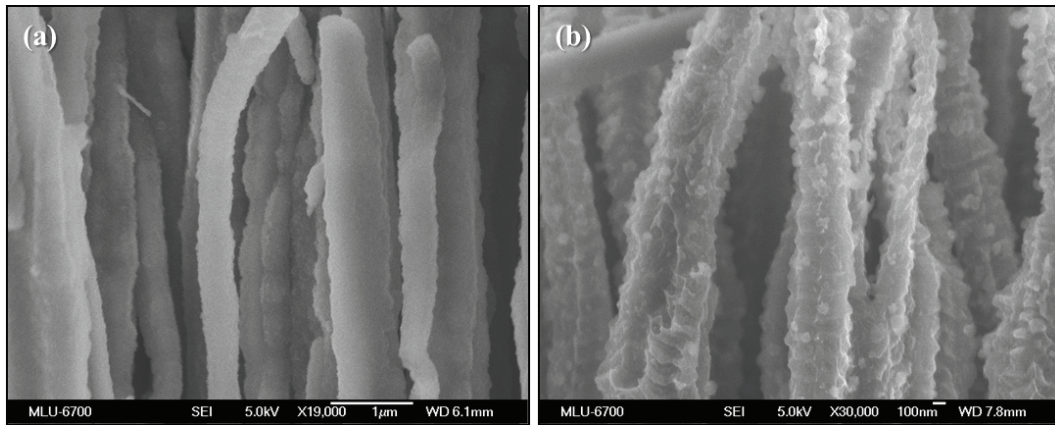


**Figure 4.5:** SEM images of (a) lithiated and (b) delithiated b-Si during the first cycle.

The discharge capacity versus cycle number for the b-Si electrode is shown in **Fig. 4.6(a)**. It is noted that the discharge capacity of the 25  $\mu\text{m}$ -long b-Si electrode decreases dramatically within 10 cycles despite its highest first coulombic efficiency compared to the other samples. However, the fading of the discharge capacity of the shorter b-Si (5 and 10  $\mu\text{m}$  lengths) electrodes is not severe, though the coulombic efficiency level is low. As a result, all of the three prepared b-Si electrodes have a poor cycle life in spite of the presence of highly-ordered nanostructures with sufficient porosity. Thus, the capacity retention of the b-Si electrode is influenced not only by the structure shape, but by the boundary reaction on the surface of b-Si. **Fig. 4.6(b)** shows an SEM image of b-Si electrode (25  $\mu\text{m}$  length) after 100 cycles. It can be observed that the entire nanostructured Si is filled with an SEI, and a thick SEI layer forms on the top of the nanostructured Si as well. This indicates that the electrolyte is decomposing severely with continuous cycling of the pure b-Si electrode, resulting in a low cycling efficiency and poor capacity retention.

Generally, the SEI layer increases the internal cell impedance and reduces the possible electric conductivity. Because of this, the discharge capacity is always higher than charge capacity. This result shows that the overall cyclability and capacity retention of the b-Si electrode are determined by many factors, not the least of which is the formation of the SEI layer during cycles. Thus, it is necessary to investigate boundary reactions between the b-Si surface and the electrolyte.

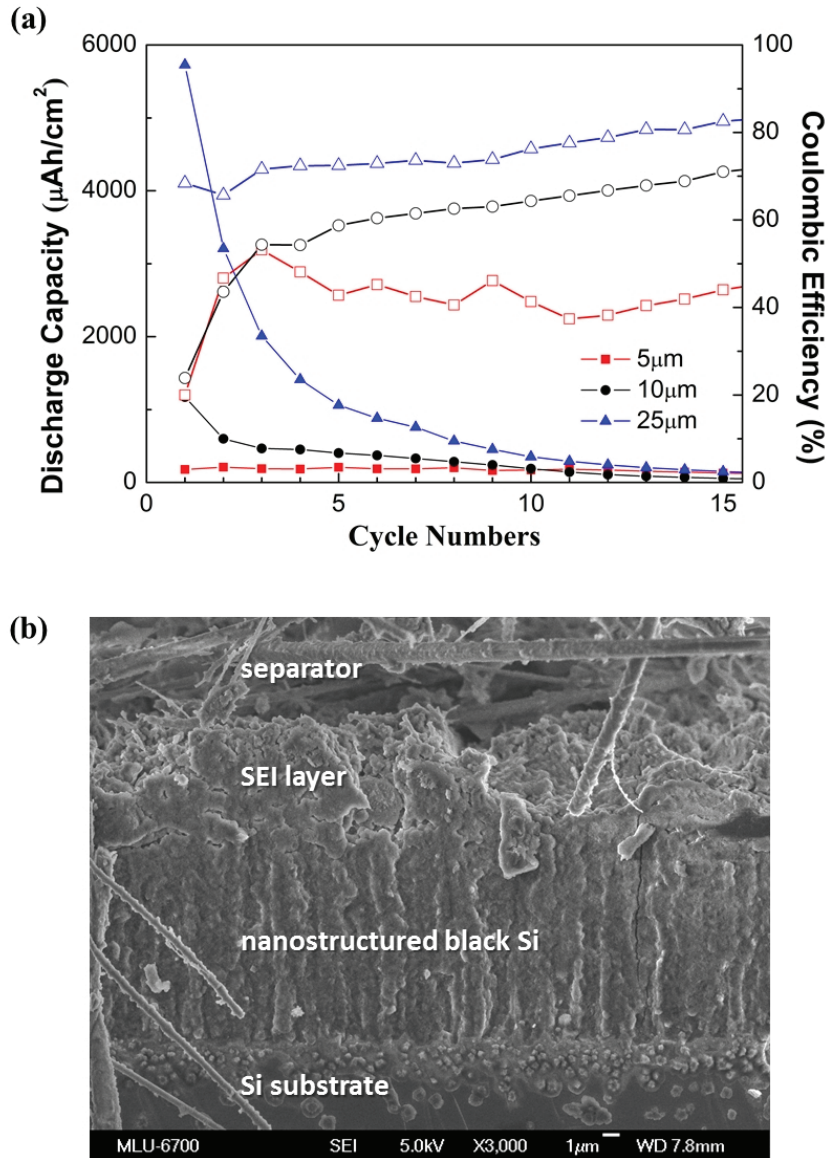


**Figure 4.6:** (a) Plot of discharge capacity (filled symbols) and coulombic efficiency (open symbols) of the cell vs. cycle numbers for the pristine b-Si electrode. (b) SEM image of the pristine b-Si electrode after 100 cycles (the cell is charged to 2.0 V).



### 4.2.2 Surface modifications of b-Si anode materials

In order to figure out the surface phase transformation at first lithiation, a b-Si ( $25\ \mu\text{m}$  length) electrode is lithiated at a low constant current density of  $50\ \mu\text{Acm}^{-2}$  for  $25\ \text{h}$  to allow a complete reaction between the lithium ions and the b-Si on the electrode. **Fig. 4.7(a)** shows a TEM image of lithiated b-Si which demonstrates that the surface morphology of b-Si is transformed into an amorphous  $\text{Li}_x\text{Si}$  phase evenly. Such a behavior is consistent with our previous experiment concerning the SiNWs electrode prepared by MaCE method. As shown in **Fig. 4.7(b)**, however, the partial amorphous  $\text{Li}_x\text{Si}$  phase is not formed uniformly on the b-Si surface when the applied constant current density is set to  $100\ \mu\text{Acm}^{-2}$ . Small ball-like shapes arise on the surface. There is also no appreciable transition of b-Si, which is characterized using the electron energy loss spectroscopy (EELS) as shown in **Fig. 4.7(c)**. The single detected EELS peak from all of the ball-like shapes (A, B and C) is situated around  $56.5\ \text{eV}$ , indicating the presence of lithium alone. This confirms that the main component of the ball-like shapes is not a Li–Si alloy, but metallic lithium. From these experimental observations, it is readily concluded that the formation of metallic lithium is related to the surface charge density and composition because most reactions occur at the area of a strong electric field.

In the interest of further cause analysis, the surface composition of a pristine b-Si electrode is determined using XPS analysis. Its spectra are plotted with that from an etched SiNWs electrode for comparison in **Fig. 4.8**. The XPS spectra of the pristine b-Si electrode exhibits a large peak at  $688.9\ \text{eV}$  attributed to F (1s) that is insignificant in the etched SiNWs electrode spectra, indicating the presence of strong C–F bonds in carbonates on the pristine b-Si surface related to the C (1s) spectra.

The high-resolution spectra for the C (1s), F (1s), O (1s) and Si (2p) peaks for pristine b-Si are shown in **Fig 4.9**. The C (1s) spectra exhibits shoulders, suggesting the presence of  $-\text{CHF}-$ ,  $-\text{CF}_2-$  and  $-\text{CF}_3$  at  $289.75$ ,  $291.65$  and  $293.73\ \text{eV}$ , respectively, while a peak at  $285.5\ \text{eV}$  corresponds to C–C and C–H in the carbonates [82, 83]. Thus, the XPS spectra study confirms that the surface of the pristine b-Si electrode is composed of stable fluorine atoms or groups ( $-\text{CF}_2-$  and  $-\text{CF}_3$ ) despite the fact that the samples are cleaned during preparation. These atoms and groups can therefore be thought to result from the mixture gas of the ICP-RIE technique. The fluorinated groups, however, can generate a hydrophobic surface for the b-Si electrode [84, 85], leading to a significant decline of the reaction between lithium ions and the nanostructured Si at the interface because the electrolyte is hydrophilic (see **Fig. 4.10**).

Therefore, the pristine b-Si electrode should be preprocessed to decompose these strong fluorinated groups ( $-\text{C}_x\text{F}_y-$ ) on the surface [86, 87]. This treatment process includes two distinct reaction mechanisms. At temperatures below about  $525\ ^\circ\text{C}$  (eq 4.1), the main decomposition product is  $-\text{CF}_3$ . At

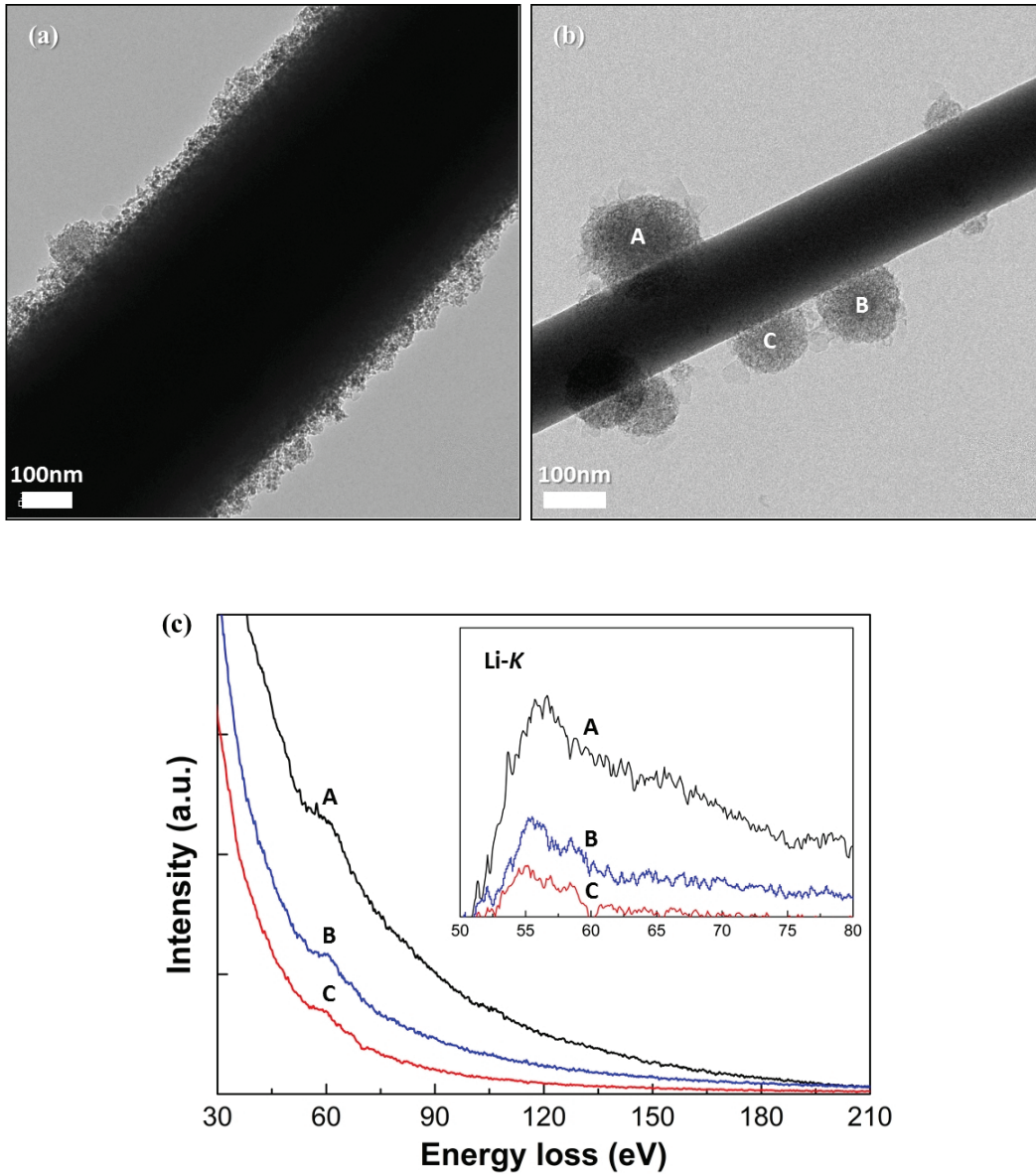


**Figure 4.7:** TEM images of the lithiated b-Si ( $25 \mu\text{m}$  length) electrode at a constant current of (a)  $50 \mu\text{Acm}^{-2}$  and (b)  $100 \mu\text{Acm}^{-2}$  for 24 h. (c) Electron energy loss spectra (EELS) obtained at the ball-like shapes on the surface of b-Si corresponding to (b).

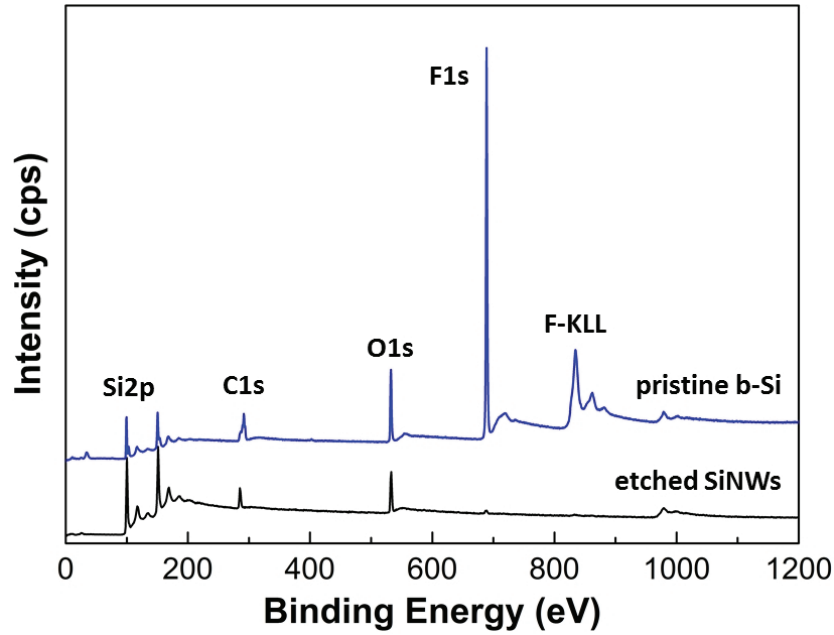


**Figure 4.8:** X-ray photoelectron spectroscopy (XPS) spectra for a comparison between the pristine b-Si electrode and the etched SiNWs electrode.

temperatures above about  $525^{\circ}\text{C}$  (eq 4.2), the  $-\text{CF}_2-$  decomposes mainly into gaseous CO and F following the chain reaction:



After this reaction, a large amount of the continuously developing oxygen and residual fluorine can be removed easily using diluted hydrofluoric acid. **Fig 4.9** includes the XPS spectra of the b-Si electrode after removing the fluorine atoms and groups in the above pretreatment process. After pretreatment, the Si (2p) and O (1s) signals of the b-Si surface are increased as well, indicating that the pristine b-Si surface is covered with a thin oxide layer. Furthermore, the Si peak at 99.5 eV increases significantly, and that of the native oxide at 103.65 eV decreases relative to the untreated pristine b-Si surface. Consequentially, this XPS analysis suggests that the application of b-Si electrodes requires not only a nanostructure to withstand the volume expansion/contraction, but also suitable surface conditions for making the redox-active compound.

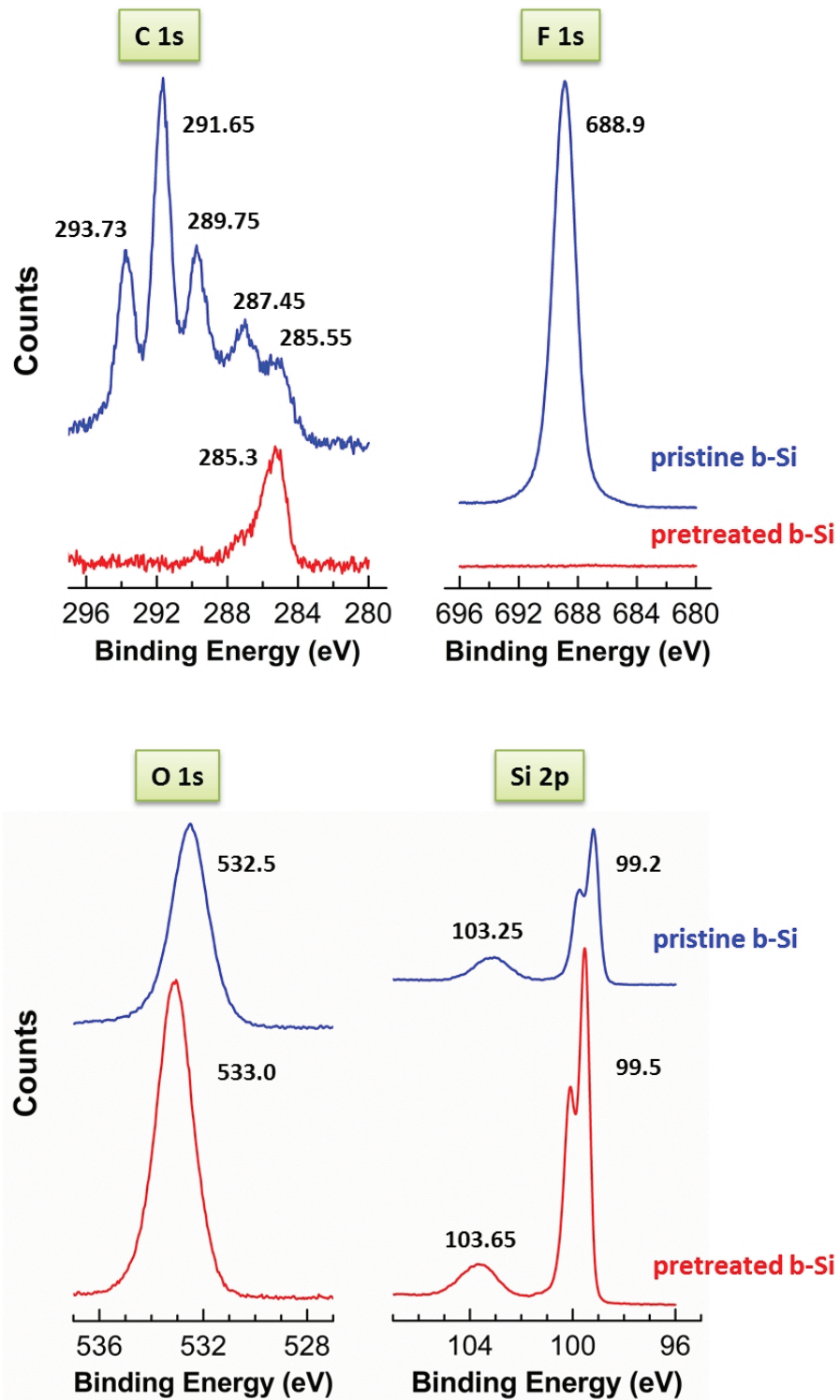


**Figure 4.9:** High resolution XPS spectra before and after surface pretreatment of b-Si electrodes.

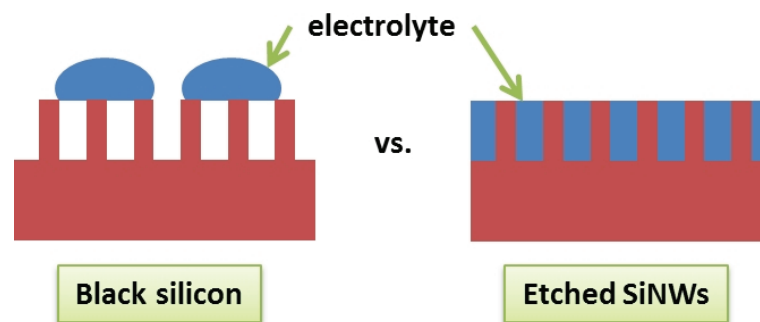


**Figure 4.10:** Schematic illustration of comparison for surface properties of pristine b-Si and etched SiNWs electrodes.

To find out the differences of redox reactions and morphology change, a CV experiment of the pretreated b-Si electrode is carried out in the same condition as a CV of pristine b-Si electrode as shown in **Fig. 4.11(a)**. In contrast with the behavior of pristine b-Si electrode (cf. **Fig. 4.3**), the pretreated b-Si electrode showed a slightly broad peak of SEI formation in the potential range of 0.5–0.7 V during the first discharge process, probably due to the removal of fluorine atoms or group. Subsequently, the redox peaks of pretreated b-Si electrode looked similar to the pristine b-Si electrode.

**Fig. 4.11(b)** and **(c)** show SEM images of pristine and pretreated b-Si electrodes after CV experiments with 30 cycles. It can be seen that the difference in two electrodes morphology is evident. The morphology of the pristine b-Si electrode had a little change due to the fluorinated group on the surface, while the pretreated b-Si electrode had lots of structural transformations induced by more active amorphization. As a result, application of silicon anode material needs not only suitable structure and shape, but also appropriate surface composition and condition to make a strong reaction between silicon and lithium ions

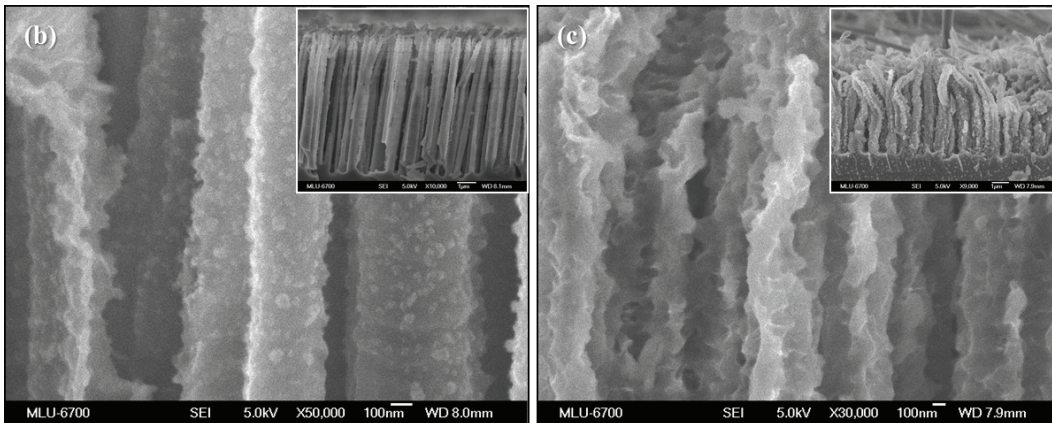
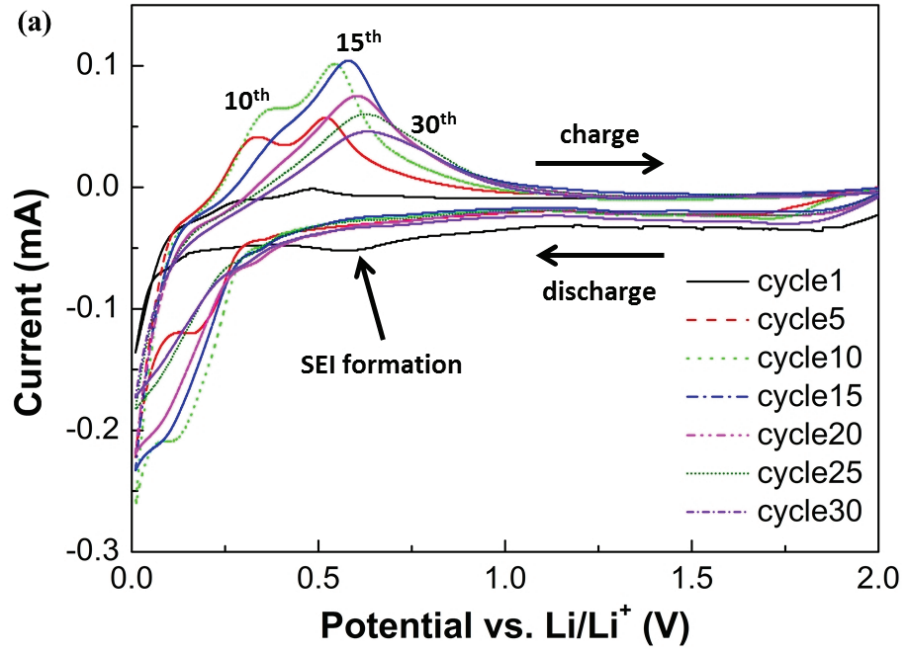


**Figure 4.11:** (a) Cyclic voltammogram of the pretreated b-Si electrode from 2.0 to 0.01 V (vs.  $\text{Li/Li}^+$ ) at a scan rate of  $0.5 \text{ mV s}^{-1}$ . SEM images after the CV experiment of 30 cycles: (b) pristine and (c) pretreated b-Si electrode.

To compare the cycle performance of a pretreated b-Si electrode with that of a pristine b-Si electrode under the same conditions, the pretreated b-Si electrode ( $25\ \mu\text{m}$  in length) is also cycled in the potential range from 0.07 to 2.0 V (vs. Li/Li<sup>+</sup>) at a current density of  $80\ \mu\text{Acm}^{-2}$  (cf. **Fig. 4.4**). The first galvanostatic charge/discharge profiles for the pristine and pretreated b-Si are shown in **Fig. 4.12(a)**. The pretreated b-Si provides a discharge capacity of  $4,320\ \mu\text{Ahcm}^{-2}$  and has a charge capacity of  $2,840\ \mu\text{Ahcm}^{-2}$  with a coulombic efficiency of 65.7%. It is noted that the pretreated b-Si electrode reaches a slightly lower charge/discharge capacity than that of the pristine b-Si electrode during the first cycle despite the decomposition of the fluorinated groups ( $-\text{C}_x\text{F}_y-$ ) on the surface. This might come from fewer side reactions and the formation of an SEI layer on the pretreated b-Si surface. Moreover, the charge curve of the pretreated b-Si exhibits two distinct regions, labeled the A and B regions, which may be the result of a phase change between crystalline and amorphous in the nanostructured Si region, or of two amorphous Si transitions in the nanostructured Si and the Si substrate region [20, 37].

**Fig. 4.12(b)** shows the galvanostatic charge/discharge capacities of the pristine and pretreated b-Si as a function of cycle number. The discharge capacity of the pretreated b-Si electrode decreases rapidly with a few cycles, like that of the pristine b-Si electrode. However, after this initial capacity drop, the pretreated b-Si electrode exhibits a comparatively stable capacity that is at least twice as high as that of the pristine b-Si electrode. The results from this study confirm that the pretreated b-Si electrodes are slightly influenced by the lithiation of the Si substrate region, leading to the capacity enhancement compared to pristine b-Si electrodes.



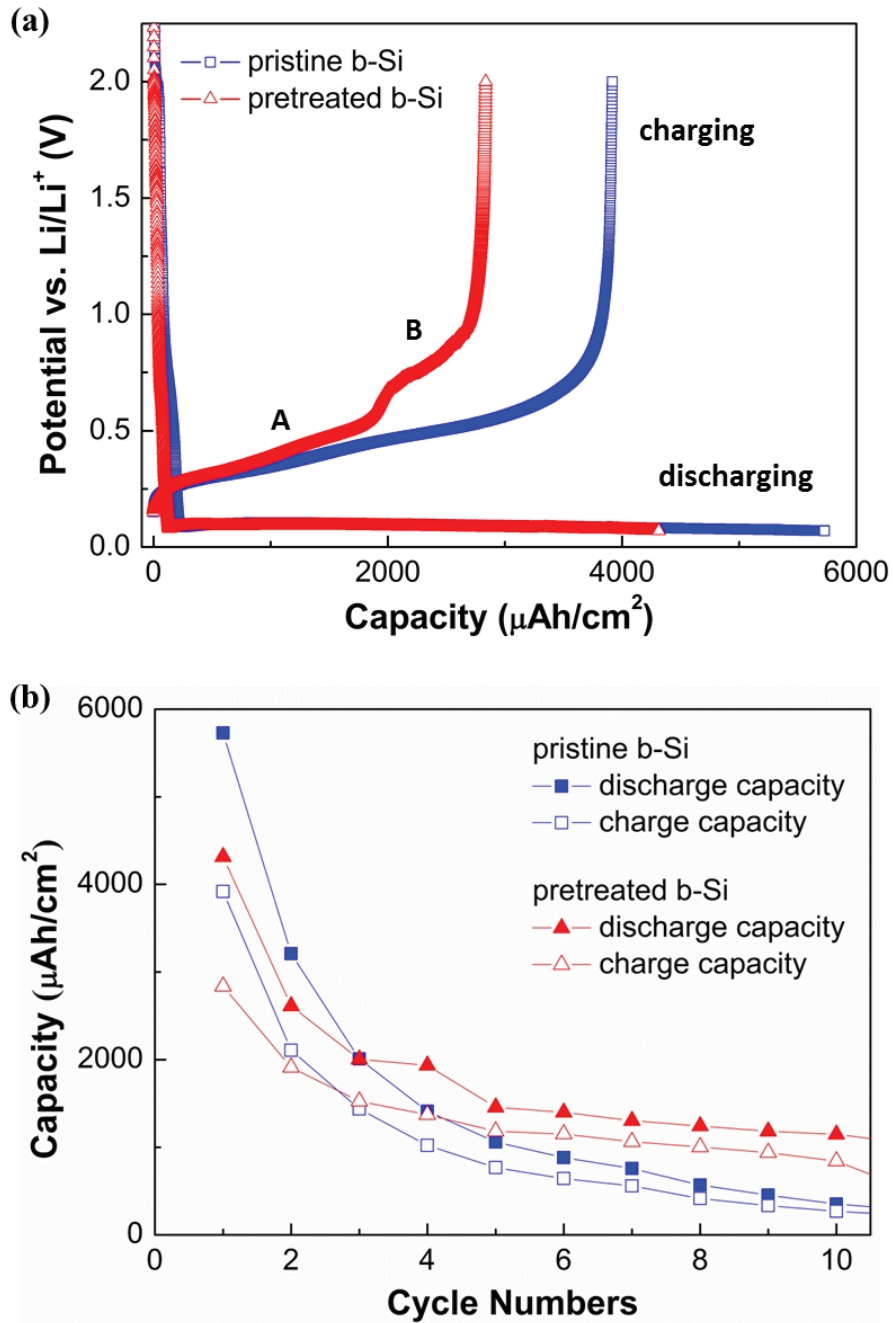


**Figure 4.12:** (a) First charge/discharge profile of pristine and pretreated b-Si electrodes at a constant current density of  $80 \mu\text{Acm}^{-2}$  (lower cutoff voltage is 0.07 V). (b) Plot of discharge (filled symbols) and charge (open symbols) capacity of the cells vs. cycle numbers for the pristine and the pretreated b-Si electrodes



### 4.2.3 Si substrate influence at a high C-rate

In the interest of minutely observing the influence of the Si substrate upon lithiation, an accelerated experiment in the voltage range from 0.01 to 2.0 V at a high current density of  $150 \mu A cm^{-2}$  is carried out with both the pretreated and pristine b-Si samples. The first galvanostatic charge/discharge curves of the samples are shown in **Fig. 4.13(a)**. The first discharge and charge capacities of the pretreated b-Si electrode reach 6,910 and  $5,220 \mu Ah cm^{-2}$ , respectively, indicating that the first coulombic efficiency is 75.5%. In comparison, the first discharge and charge capacities of the pristine b-Si electrode reaches 6,640 and  $4,630 \mu Ah cm^{-2}$ , respectively, with a first coulombic efficiency of 69.6%. The capacity and efficiency of both samples are similar, though the potential profiles of each is quite different at the initial lithiation.

As shown in **Fig. 4.13(b)**, the potential drop and rise at the first stage of lithiation is observed, reflecting a large overpotential, or *IR-drop*, induced by a Si substrate influence. Such behavior of the overpotential can be attributed to a high resistivity and low reaction kinetics during lithium ion insertion into the crystalline Si, leading to the decline of electrical conductivity upon subsequent cycling [27, 88]. The potential of the pretreated b-Si electrode drops initially to around 0.02 V, which is much less than that of the pristine b-Si electrode of around 0.06 V. This demonstrates that it is important to consider the condition of the surface composition and the current rate regarding the lithiation. For this reason, when the low cutoff voltage is kept above 0.07 V to prevent the formation of a crystalline Li–Si phase, a high current rate (like the used  $150 \mu A cm^{-2}$ ) is not possible due to its large potential drop below this crystallization limit of 70 mV. Such overvoltage at the initial lithiation stage may restrict the current rate range of application for these electrodes.

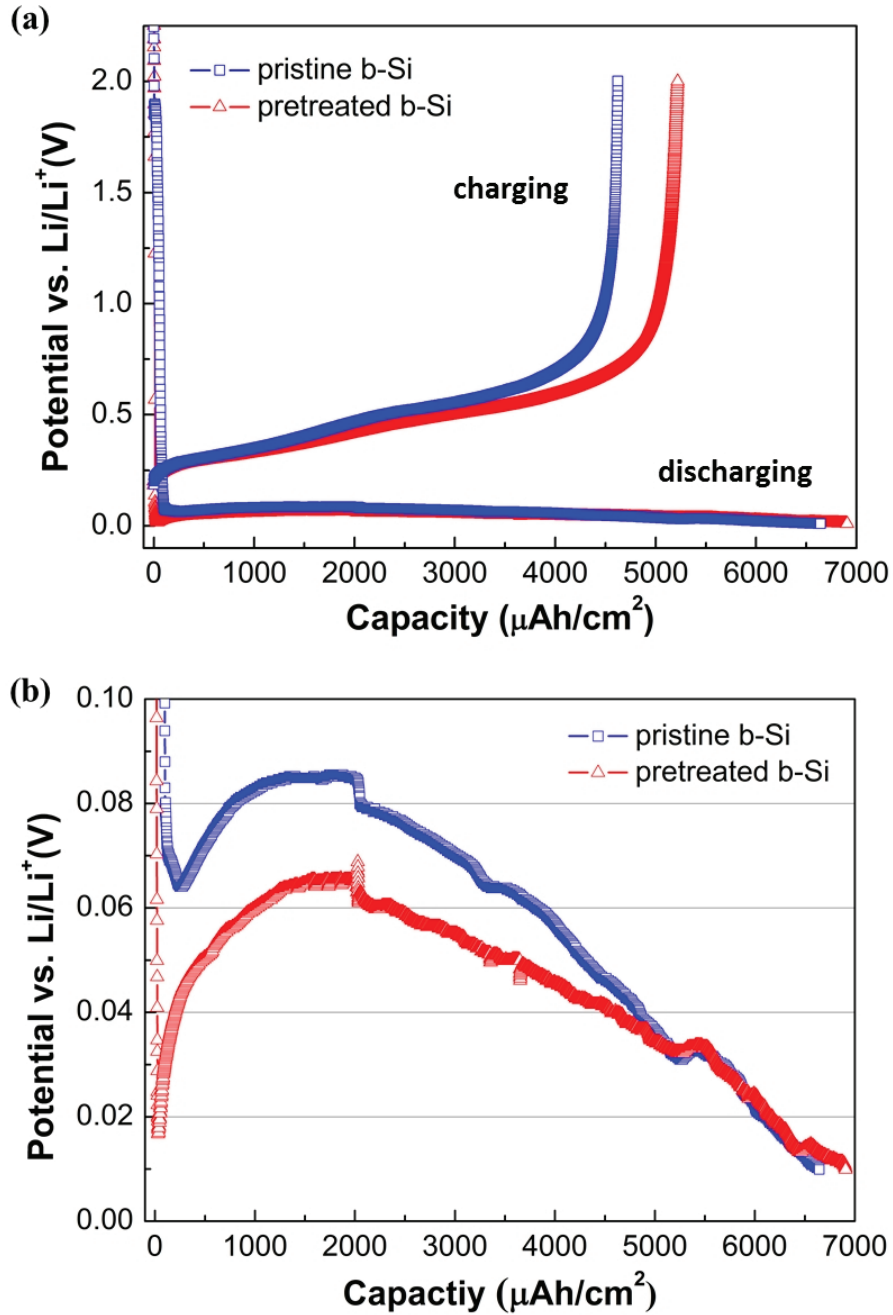


**Figure 4.13:** (a) First charge/discharge profile of pristine and pretreated b-Si electrode between 0.01 and 2.0 V (vs. Li/Li<sup>+</sup>) at a high constant current density of  $150 \mu A cm^{-2}$ . (b) First potential profile of pristine and pretreated b-Si electrode in the potential range from 0.0 to 0.12 V.

**Fig. 4.14** shows the discharge capacity cycles of both samples with regard to the accelerated experiment. The pristine and pretreated b-Si electrodes have a similar discharge capacity at the first cycle, but subsequent cycles exhibit a different behavior. The second discharge capacity of the pretreated b-Si electrode greatly increases and then drops significantly within a few cycles, whereas that of a pristine b-Si electrode drops to one-third of the first charge capacity until the sixth cycle, and then increases to about double the capacity (marked by  $\Downarrow$ ) followed by a significant second drop.

The reason for this abruptly rising charge capacity of both samples is the similar formation of Li–Si alloys in the Si substrate in spite of the difference in their surface conditions. In other words, it can be ascribed to the kinetics difference between the lithium ion diffusion and the electron injection at a high current rate. First of all, only the nanostructured Si can be converted to an amorphous Li–Si phase during the initial charge process because of its high electrical conductivity compared with that of the Si substrate. However, as more lithium ions are inserted with the increasing number of cycles, the electrical conductivity will decrease owing to the phase transformation from crystalline Si to amorphous Li–Si embedded in the nanostructure Si. Thus, more lithium ions move deep into the Si substrate to react with crystalline Si. This is confirmed by the fact that the breakage of Si–Si bonds is an essentially slower process than the diffusion of lithium ions in the Li–Si phase (Li ions diffusion coefficient in Si:  $10^{-13} \text{ cm}^2 \cdot \text{s}^{-1}$ ) [89, 90, 91]. As the reaction progresses with the number of cycles, the gap in kinetics becomes wider, causing more of the Si substrate to be involved in lithiation at the high current rate (see **Fig. 4.15**).

Eventually, the Si substrate experiences significant cracking that provokes a failure of the b-Si electrode because the bulk Si substrate cannot endure the mechanical stress induced by a large volume expansion, unlike the nanostructured Si [75, 92, 93].

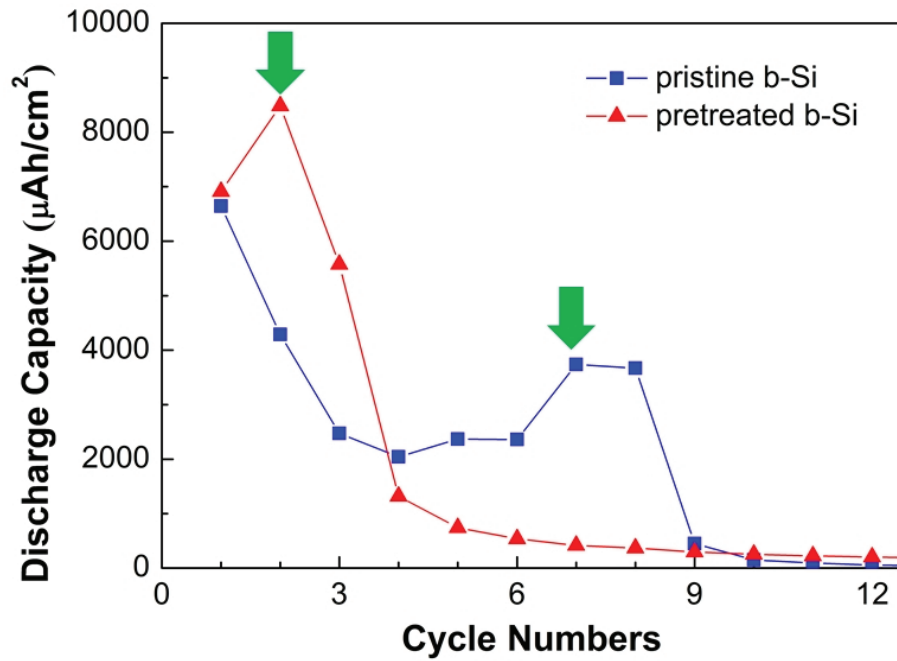


**Figure 4.14:** Plot of discharge capacity of the cell vs. cycle numbers for the pristine and the pretreated b-Si electrode at a high constant current density of  $150 \mu A cm^{-2}$ .

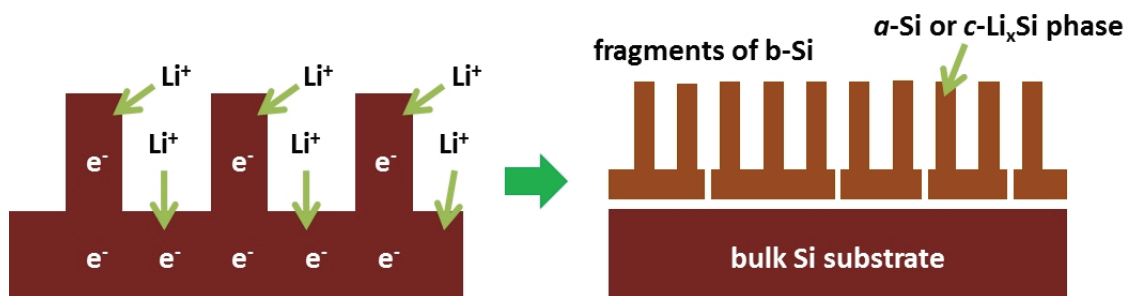


**Figure 4.15:** Schematic illustration of the failure of the b-Si electrode at a high C-rate when the low cutoff voltage is 0.01 V (vs. Li/Li<sup>+</sup>).

This result is corroborated by the SEM image of the b-Si electrode after the accelerated cycling experiment (see **Fig. 4.16**), which clearly shows that the cycled b-Si electrode split into a detached nanostructure Si part and Si substrate part. It is probably due to volume expansion at the boundary between the nanostructured Si and the Si substrate. Consequentially, the failure of the b-Si electrode is related to the fast lithiation of the nanostructure and not to a strong potential caused by the influence of the Si substrate upon lithiation. Therefore, a balance between the electrical resistance and the current rate during the lithiation process is a key factor for a better cycle life and for stable capacity retention of pure b-Si electrodes.

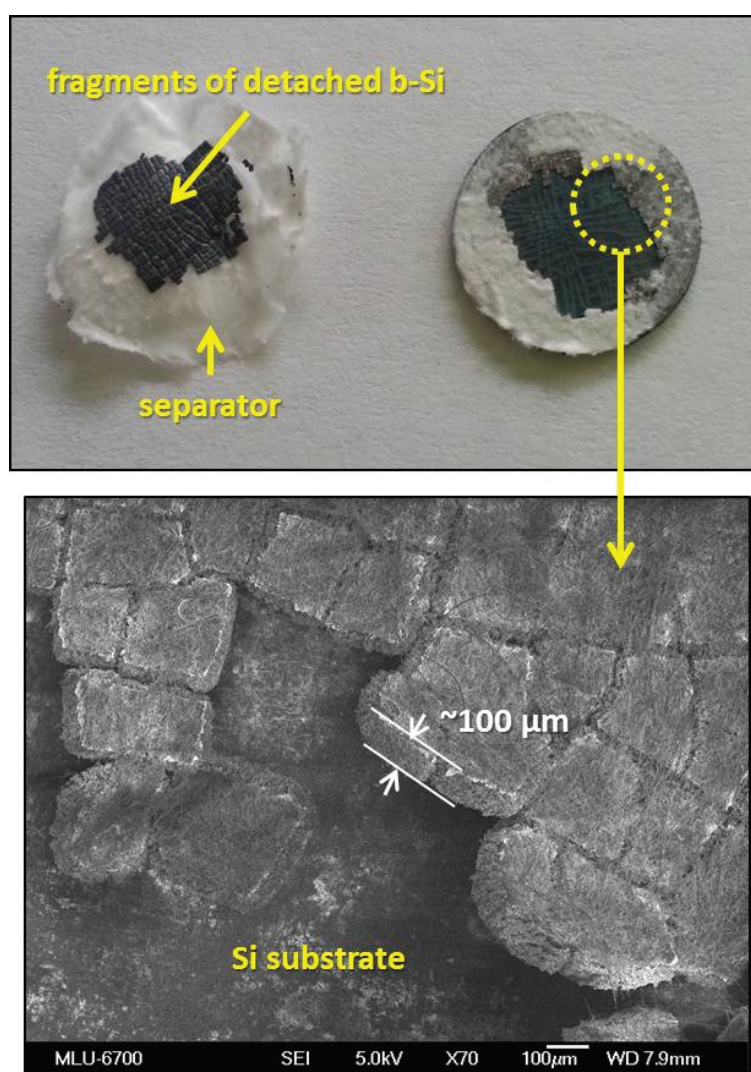


**Figure 4.16:** Photograph and SEM image of b-Si electrodes after accelerated cycle experiments.

### 4.3 Summary

In this chapter, the electrochemical properties of an original nanostructured black silicon (b-Si) anode without binder or conducting materials were investigated. The b-Si was prepared by inductively coupled plasma reactive ion etching (ICP-RIE) technique in rechargeable lithium-ion batteries. The poor cycle life is likely caused by the constant reformation of a SEI layer on the b-Si surface, leading to a reduction of the electric conductivity. Moreover, the formation of a Li–Si alloy during subsequent cycles is dependent upon the surface composition condition and, in particular, upon whether the surface is hydrophobic or hydrophilic. Additionally, metallic lithium is observed on the b-Si surface at high current rates, which is likely due to a nonequilibrium electric charge distribution induced by the presence of fluorinated groups covering the surface of the pristine b-Si. These results show that the cycle life of b-Si electrodes is stronger influenced by the formation of SEI layers and the related surface conditions than by the nanostructure shapes chosen to accommodate a large volume expansion. In regard to the fast lithiation experiment, the nanostructured Si section of the electrode is detached from the Si substrate, induced by the kinetics difference between the diffusion of the lithium ions and the electron injection and phase transformation in nanostructured Si. As a result, a high current rate and the lithiation of the Si substrate are strongly related, though the nanostructured Si has a high electrical conductivity

The results illustrate the major factors of the surface properties relating to the formation of SEI layers and the correlation between the high current rate and the failure in cycle life. In addition, their role in electrochemical processes is presented regarding nanostructured Si on a Si substrate for understanding the fundamental lithium reaction mechanism in pure Si anodes. The noble b-Si electrode may not be used directly as an anode material, but the presented data can increase the understanding of the electrochemical process and the optimal design of a b-Si electrode to increase efficiency and cycle life in Li–ion batteries.

## Chapter 5

# Metal-coated Nanostructured Silicon (M-Si) as Anode Material

In this chapter, the properties of fully complementary metal-oxide semiconductor (CMOS) compatible metal-coated nanostructured silicon anodes for Li-ion microbatteries will be studied. Microbatteries are required to drive small devices such as smartcards, medical implants, sensors, etc. [94, 95, 96, 97]. To date, the electrochemical performances of these all-solid-state batteries are limited because planar thin films are employed as electrode and electrolyte materials. In order to develop improved electrochemical performances new materials and CMOS-compatible high-throughput manufacturing processes are required. Therefore for comparison and evaluation of metal material additives [98, 99, 100], gold (Au) as a representative active metal material and copper (Cu) as an inactive metal material are used, respectively. The active materials can be influenced by Li ions, whereas the inactive materials are impervious to Li ions. In Section 5.1, the fabrication and characteristics of metal-coated nanostructured silicon electrodes are shown. Afterward, the galvanostatic charge/discharge measurements are demonstrated in Section 5.2. Furthermore, the electrochemical and microstructural properties before and after cycling of the metal-coated nanostructured silicon compared to their pristine counterparts are investigated in detail. This study suggests that for the improvement of Li-ion batteries, the electrolyte stability has to be enhanced more urgently than the variation of Si nanostructures.

## 5.1 Experimental

### 5.1.1 Metal-coated nanostructured silicon (M-Si) fabrication via sputtering

Highly ordered silicon nanowire arrays (SiNWs) are fabricated via the one-step MaCE method on Si substrate, and nanostructured black silicon (b-Si) is prepared by the ICP-RIE method as discussed in chapter 3 and chapter 4, respectively. Both specimens use the same Si substrate that is a single crystal n-type Si (100) wafer, 525  $\mu\text{m}$  in thickness with a resistivity of  $1 - 5 \Omega \cdot \text{cm}$ . Afterward, the wafer-scale SiNWs and b-Si are cut into small pieces of suitable size, about 10 mm in diameter. Gold (Au, 99.99%) and copper (Cu, 99.98%) are deposited onto the surface of SiNWs and b-Si electrodes using a sputter coater (108auto, Cressington), equipped with a high resolution thickness monitor system (MTM10, Cressington). Eight metal (Au, Cu)-coated SiNW and b-Si electrodes with a thickness of 20 and 50 nm were prepared, respectively as shown in **Fig. 5.1**.

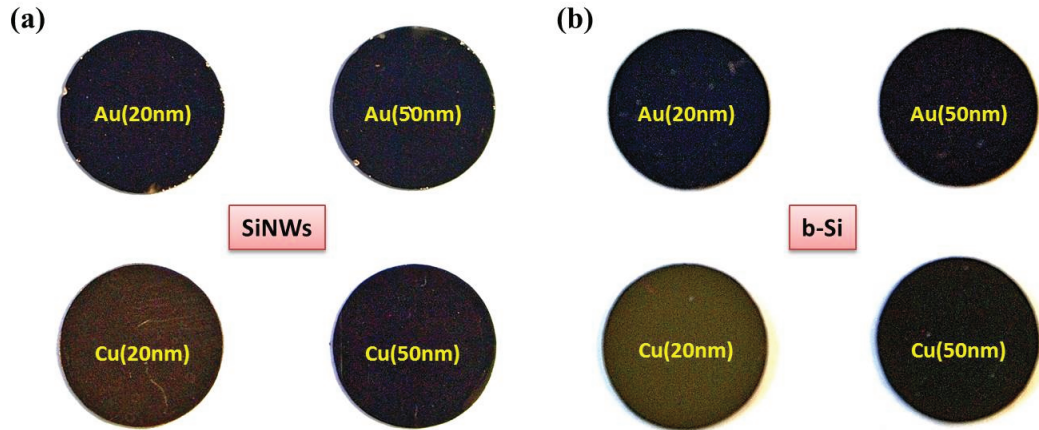


**Figure 5.1:** Photograph of metal-coated nanostructured silicon electrodes. (a) metal-coated silicon nanowires (SiNWs) and (b) metal-coated nanostructured black silicon (b-Si) electrodes.



### 5.1.2 Metal-coated nanostructured silicon (M-Si) properties

**Fig. 5.2** shows SEM images of the as-prepared Au- and Cu-coated SiNWs electrodes, respectively. The vertically aligned Si nanostructures with a length of  $25\ \mu\text{m}$  and  $50\text{--}100\ \text{nm}$  in diameters are obtained by one-step MaCE method and then magnetron sputtering technique on Si substrate. The average distance between the nanowires is in the range of  $0.1$  to  $0.3\ \mu\text{m}$ . As an original part of the Si substrate, the SiNWs ensures an effective charge transport through direct electric pathways. The element distribution of the metal coating was characterized by energy-dispersive X-ray spectroscopy (EDX) mapping. The Au and Cu images show that the most metal is deposited on the upper part of nanostructure. The main reason for this feature is that the metal elements can only penetrate into the top part of the SiNWs due to physical nature of the sputtering process and the high density of Si nanostructures, whereas the Au and Cu images of b-Si electrodes with a length of  $28\ \mu\text{m}$  and about  $730\ \text{nm}$  in diameter show the uniform distribution of metal along the Si nanostructure with hardly any agglomeration (see **Fig. 5.3**).

This means the b-Si prepared via ICP-RIE method offers wider free space between Si nanostructures compared to SiNWs fabricated by MaCE method, leading to the performance improvement by accommodating the volume expansion of Li–Si alloy. The average distance between the nanowires was about  $1\ \mu\text{m}$ . The oxygen images of both specimens are attributed to the surface oxidation covering Si nanostructures and the Si images correspond to the morphology of SiNWs and b-Si electrodes in the SEM images, respectively. These results confirm that the metal-coated Si electrode is composed of nanostructured Si covered with a uniform Au and Cu coating with a small amount of oxides on surface of nanostructured Si.

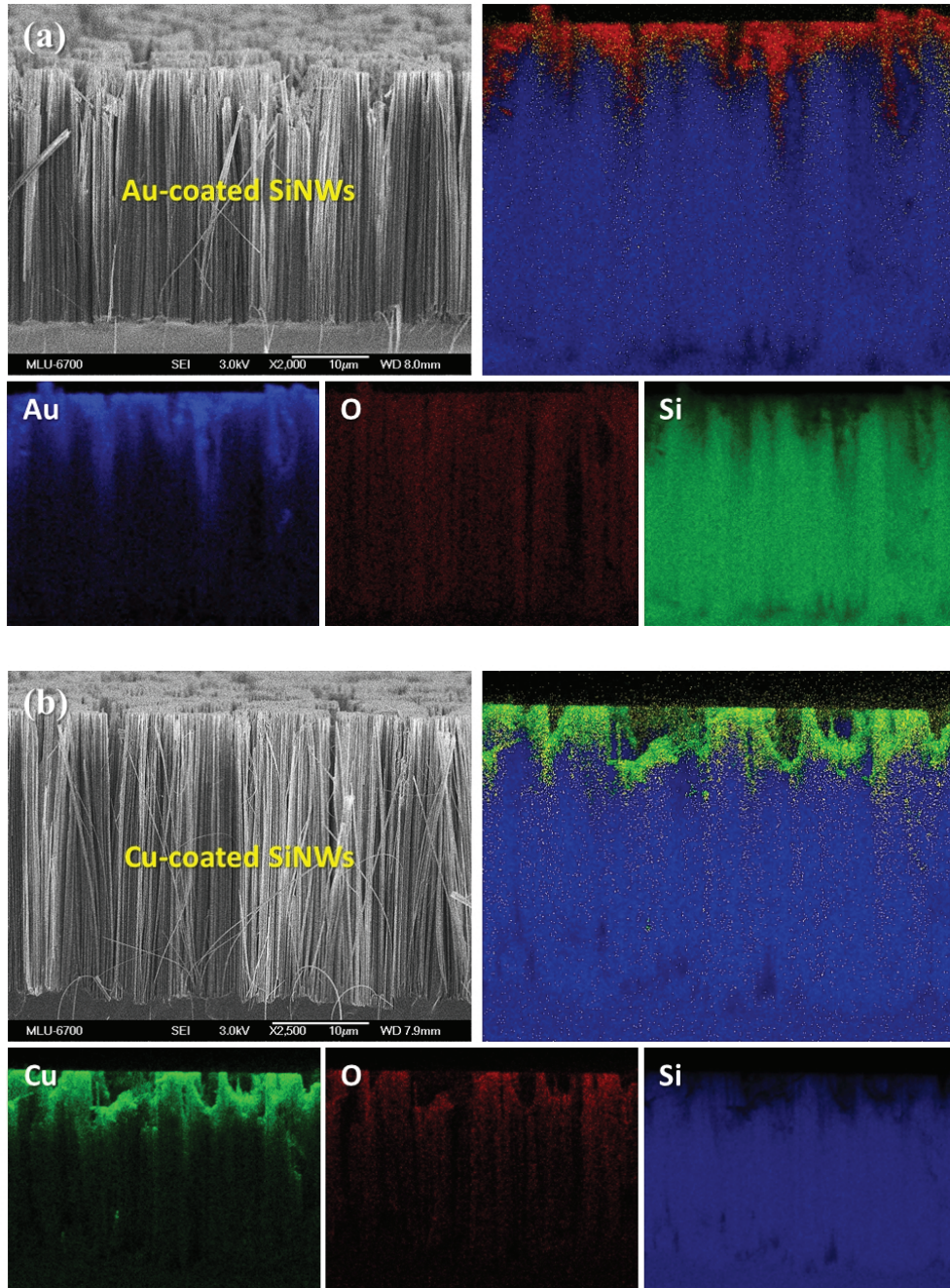


**Figure 5.2:** Characterization of the morphology of metal-coated SiNWs electrodes. SEM images of (a) Au-coated and (b) Cu-coated SiNWs showing where the elemental maps are obtained and corresponding element mapping images of Au, Cu, O and Si. The upper right images show the summarized elemental signals.

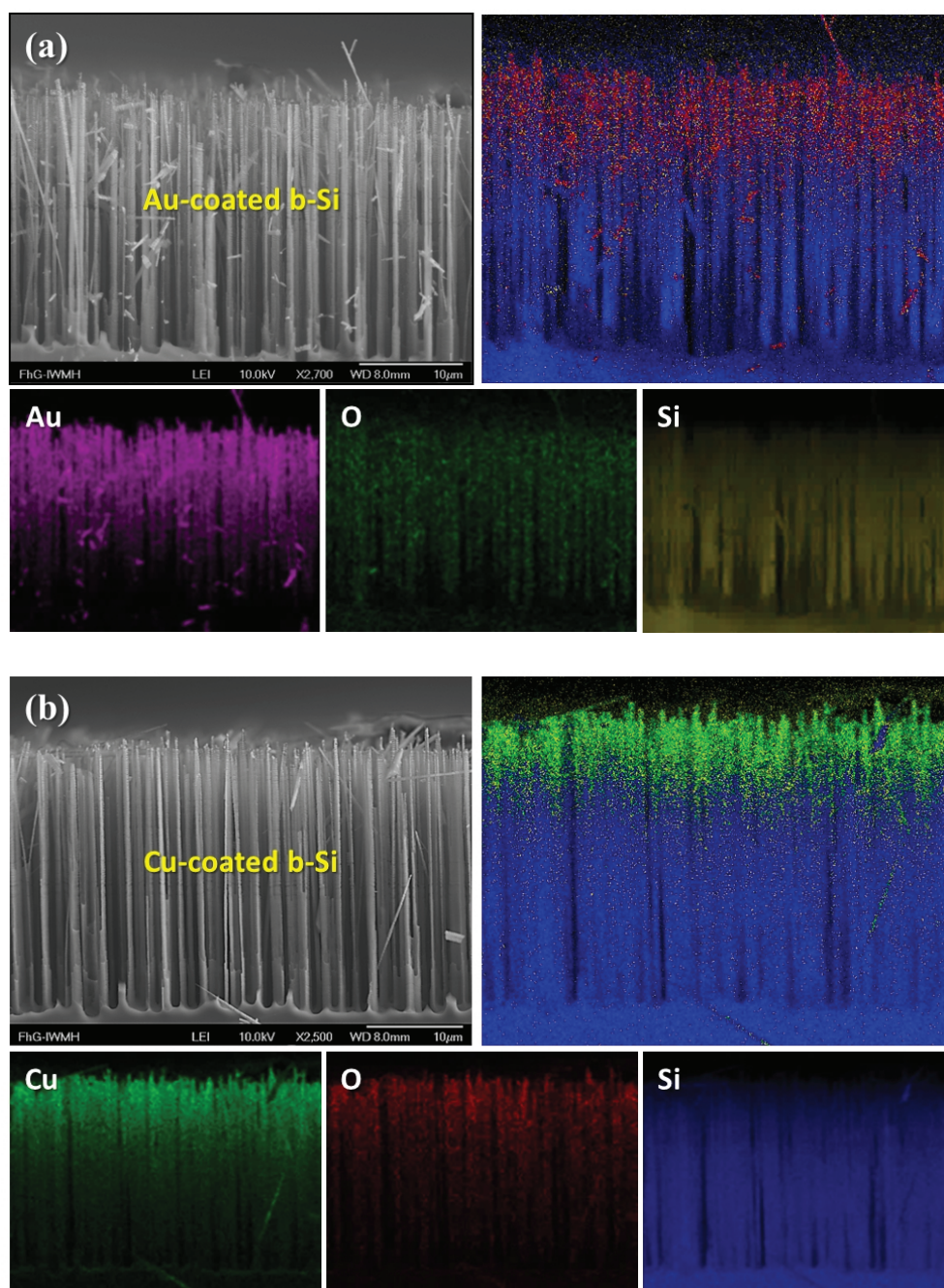


**Figure 5.3:** Characterization of the morphology of metal-coated b-Si electrodes. SEM images of (a) Au-coated and (b) Cu-coated b-Si showing where the elemental maps are obtained and corresponding element mapping images of Au, Cu, O and Si. The upper right images show the summarized elemental signals.



To determine the structural properties of metal-coated nanostructured Si, X-ray diffraction (XRD) patterns of the metal-coated SiNWs and b-Si are compared with those of the pristine nanostructured Si.

**Fig. 5.4** shows XRD patterns of metal-coated and pristine SiNWs, and metal-coated and pristine b-Si electrodes. The XRD patterns of metal-coated SiNWs indicate that diffraction peaks are associated crystalline structures with Au (111), (200), (220) and (311) regarding Au-coated SiNWs and Cu (111) regarding Cu-coated SiNWs, respectively (see **Fig. 5.4(a)**).

In addition, peaks of crystalline silicon are detected, such as (111), (220) and (311). The intensity of the Si (400) peak at about  $70^\circ$  is high compared to others induced by the large crystalline Si substrate. The diffraction peaks of metal-coated b-Si show similar crystalline structures of Au and Cu metal. However, the intensity of the Si (311) at  $56.3^\circ$  of metal-coated b-Si decreases significantly compared with that of metal-coated SiNWs, confirming that the Au and Cu metal are uniformly deposited in the sufficient free space of b-Si as mentioned before.

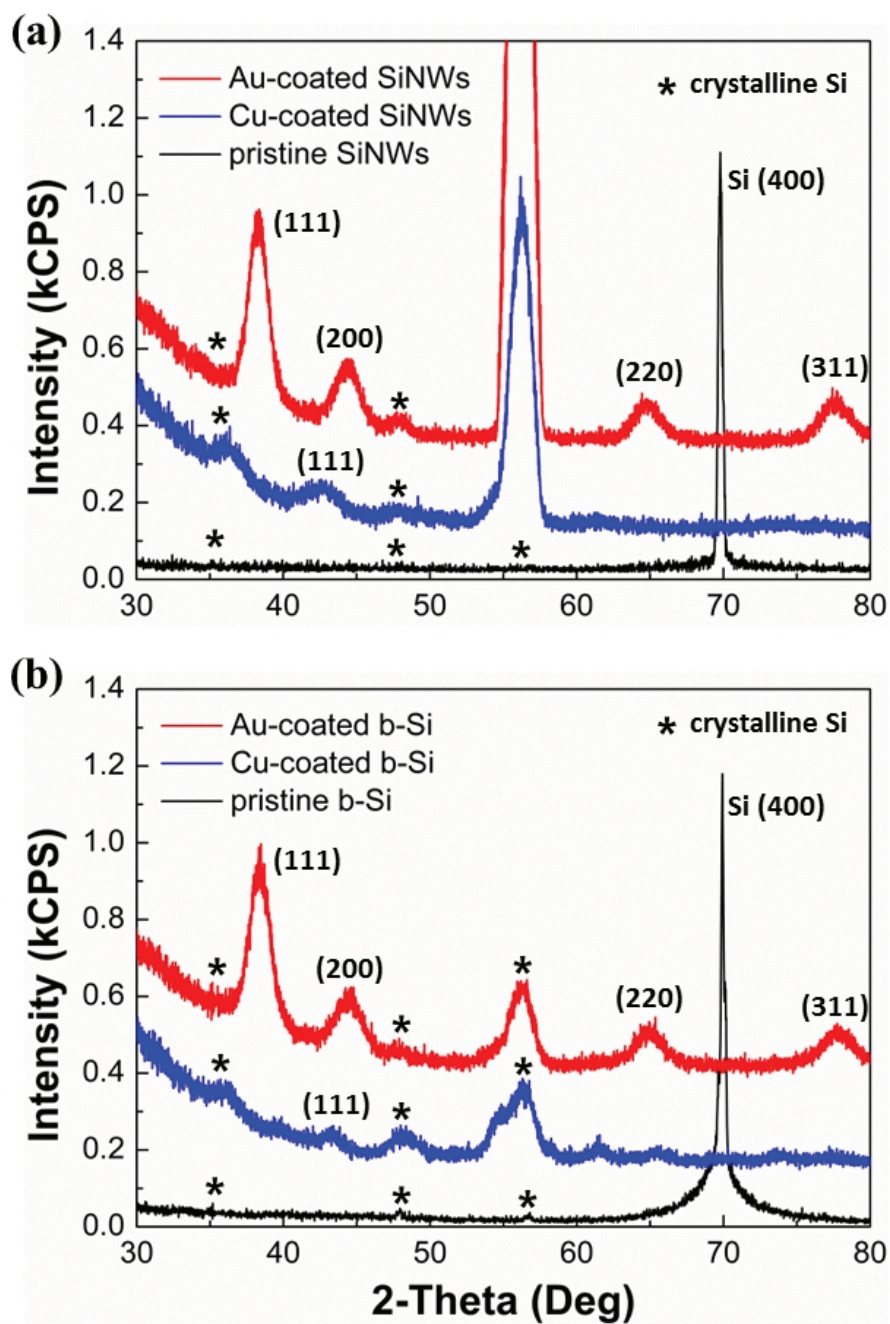


**Figure 5.4:** X-ray diffraction (XRD) patterns of metal-coated nanostructured Si electrodes. (a) XRD patterns of (a) Au-coated, Cu-coated and pristine SiNWs electrodes, and (b) Au-coated, Cu-coated and pristine b-Si electrode.

## 5.2 Results and Discussion

### 5.2.1 Electrochemical measurements of M-Si anodes

To investigate the cycling performance of metal-coated nanostructured Si electrodes, the galvanostatic electrochemical technique is used in the voltage range from 0.1 to 2.0 V (vs. Li/Li<sup>+</sup>) at a constant current density of  $50 \mu\text{Acm}^{-2}$ .

**Fig. 5.5(a)** shows the first charge/discharge curves of 20 nm and 50 nm Au-coated SiNWs. The first discharge capacity of Au(20) and Au(50)-coated SiNWs reaches 2,520 and 2,280  $\mu\text{Ahcm}^{-2}$ , the charge capacity is 1,100 and 580  $\mu\text{Ahcm}^{-2}$  with a coulombic efficiency of 43.6 and 25.5%, respectively. Both capacities of discharge and charge are vastly higher than that of pristine SiNWs. However, the first coulombic efficiencies show a little high and a similar value to that of pristine SiNWs, 26.6%, indicating that the first irreversible capacity loss is still high.

In addition, the discharge capacity of thin Au(20)-coated SiNWs is higher than thick Au(50)-coated SiNWs. In the same manner as these results, the discharge capacity of thin Cu(20)-coated SiNWs, 1690  $\mu\text{Ahcm}^{-2}$ , is higher than that of thick Cu(50)-coated SiNWs, 1,110  $\mu\text{Ahcm}^{-2}$  (see **Fig. 5.5(b)**). However, both specimens have similar charge capacities of 383 and 414  $\mu\text{Ahcm}^{-2}$ , giving a coulombic efficiency of 22.7 and 37.4%, respectively.

These specific capacities are still slightly high compared to pristine SiNWs. But, the capacity increase of Cu-coating is not as strong as in the case of Au-coating. Consequently, metal coating is able to improve the charge/discharge capacity, but a high coulombic efficiency is still required to reduce irreversible capacity loss at the first cycle in case of SiNWs electrodes.

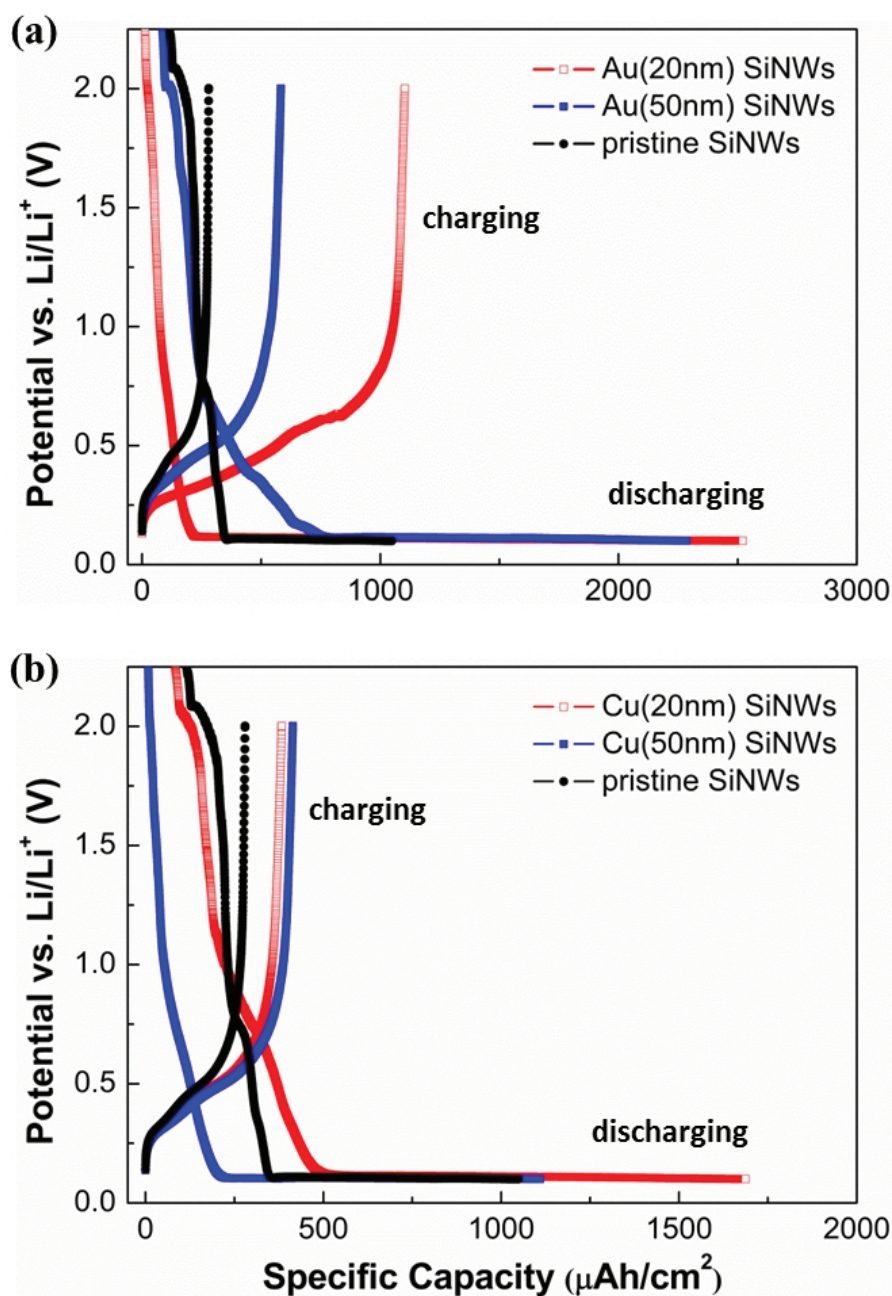


**Figure 5.5:** The galvanostatic charge/discharge voltage profiles obtained with metal (Au, Cu)-coated SiNWs electrodes between 0.1 and 2.0 V (vs.  $\text{Li/Li}^+$ ) at a constant current density of  $50 \mu\text{Acm}^{-2}$ . (a) Au-coated, (b) Cu-coated SiNWs electrodes compared to the pristine SiNWs electrode.

In contrast, metal-coated b-Si shows somewhat different behaviors. **Fig. 5.6** displays the charge/discharge curves of Au-coated and Cu-coated b-Si at its first cycles. The first discharge capacity of Au(20) and Au(50)-coated b-Si reaches 706 and 1,160  $\mu Ahcm^{-2}$  with a coulombic efficiency of 44.3 and 47.2 %, respectively (see **Fig. 5.6(a)**). Both specific capacity and coulombic efficiency is significantly higher than that of pristine b-Si. Moreover, the discharge capacity of Au(50)-coated b-Si is higher than that of Au(20)-coated b-Si contrary to results of Au-coated SiNWs. This is because Au could contribute to form Au-Li-Si alloys as an active material for lithium-ion battery systems.

In comparison, the first discharge capacities of Cu(20) and Cu(50)-coated b-Si are 716 and 633  $\mu Ahcm^{-2}$ , giving a coulombic efficiency of 56.6 and 47.9 %, respectively (see **Fig. 5.6(b)**). This is still slightly higher compared to pristine b-Si as well. However, the increase is not as strong as in the case of Au-coating since Cu is an inactive material. In addition, the discharge capacity of thin Cu(20)-coating is slightly higher than that of thick Cu(50)-coating in contrast to the Au-coatings. As a result, the Au-coating shows a significant enhancement in capacity with increasing thickness of Au in case of metal-coated b-Si.

Consequently, metal coating can help the capacity increase of SiNWs and b-Si electrode. Regarding the influence of the different thicknesses of Au and Cu, Au-coating shows a great variation in capacity according to the deposited thickness. On the other hand, the thickness of Cu-coating has hardly any influence on the specific capacity at the first cycle. Instead, the coulombic efficiency of Cu-coating shows a slightly improvement compared to that of Au-coating. However please note that all prepared metal-coated nanostructured Si show a relative low coulombic efficiency of around 50 %, mainly resulting from the slow reaction paths along the huge specific surface area.



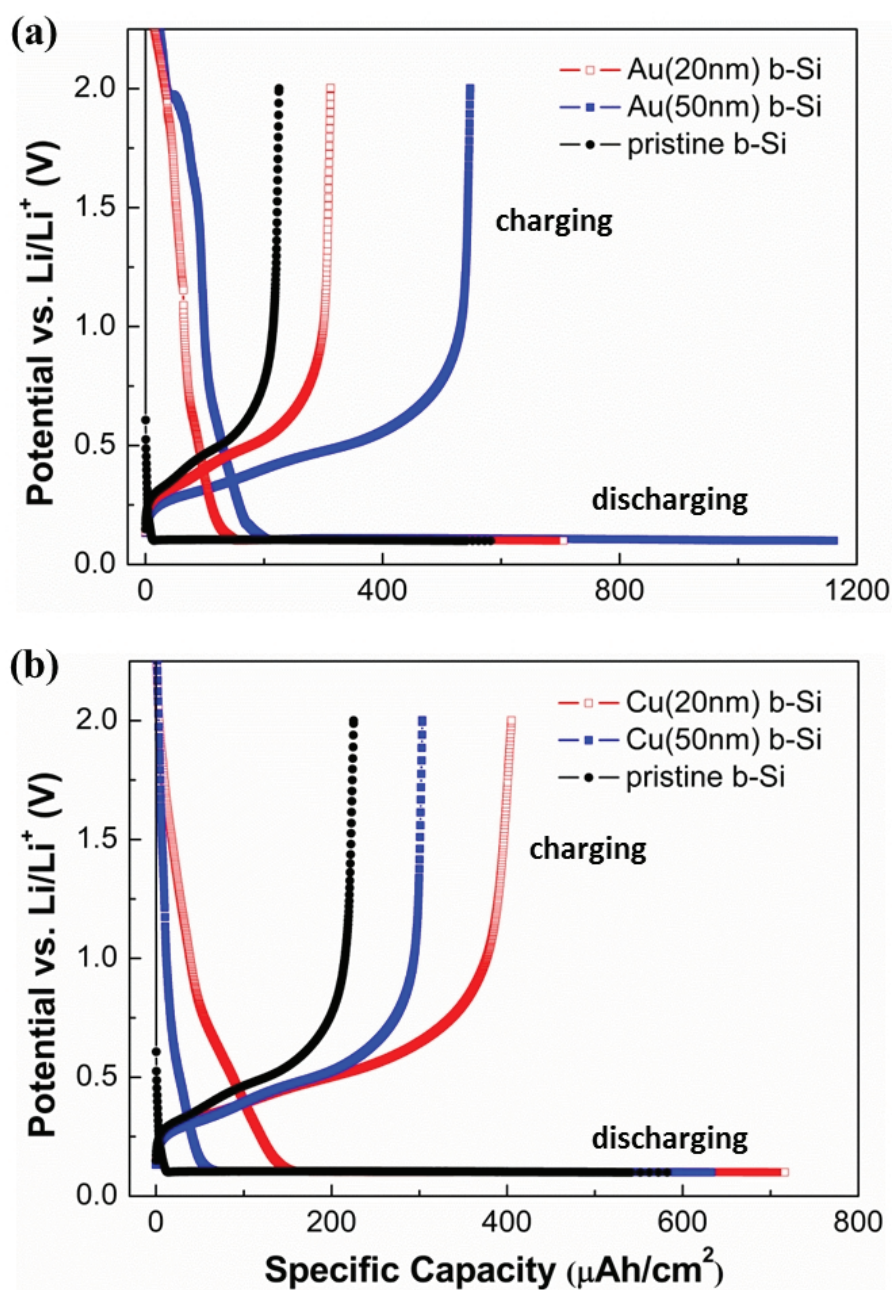


**Figure 5.6:** The galvanostatic charge/discharge voltage profiles obtained with metal (Au, Cu)-coated b-Si electrodes between 0.1 and 2.0 V (vs.  $\text{Li/Li}^+$ ) at a constant current density of  $50 \mu\text{Acm}^{-2}$ . (a) Au-coated, (b) Cu-coated b-Si electrodes compared to the pristine b-Si.

### 5.2.2 Cyclability for M-Si anodes

**Fig. 5.7** shows the discharge capacity versus cycle number for metal-coated nanostructured Si electrodes in the voltage range from 0.1 to 2.0 V (vs. Li/Li<sup>+</sup>) at a constant current density of  $50 \mu A cm^{-2}$ . The metal-coated SiNWs electrodes show a significantly capacity drop upon cycles along with pristine SiNWs (see **Fig. 5.7(a)**). The possible reason is that metal elements are only deposited on the upper part of Si nanostructures, resulting in the fact that specific capacity of metal-coated SiNWs electrodes can increase at the initial cycle. Shortly afterwards, however, reaction between Li ion and Si occurs along the pristine nanostructures. In contrast, metal-coated b-Si electrodes show high capacity retention upon cycles (see **Fig. 5.7(b)**). In particular, the 50 nm Cu-coated specimen has still about 70 % after 20 cycles (**Table 5.1**), whereas pristine b-Si has a remaining capacity of only 24 %. This happens because metal coating is uniformly distributed according to nanostructures having a sufficiently large free space against the volume expansion/extraction.

These electrochemical cycling results of metal-coated b-Si show that the metal coating can improve not only the discharge capacity but also the capacity retention compared to pristine b-Si confirming previous results on other silicon nanostructures [101, 102, 103, 104] and extending it to CMOS compatible processes. This improved stability might be explained by the fact that the metal layer has better electronic and electrochemical interfacial properties than the SEI / silicon interface in the case of pristine b-Si.

To further verify the improved behavior of the morphology and volume changes of metal-coated b-Si, particularly Cu-coated specimens, SEM analysis of the metal-coated b-Si at a fully delithiation after 50 cycles compared to a pristine one is performed (see **Fig. 5.8**). Most of the metal-coated b-Si retained its original shape without cracking or fracturing. The metal coated b-Si shows only slight deformations and volume changes, resulting from the amorphization during continuous cycling.

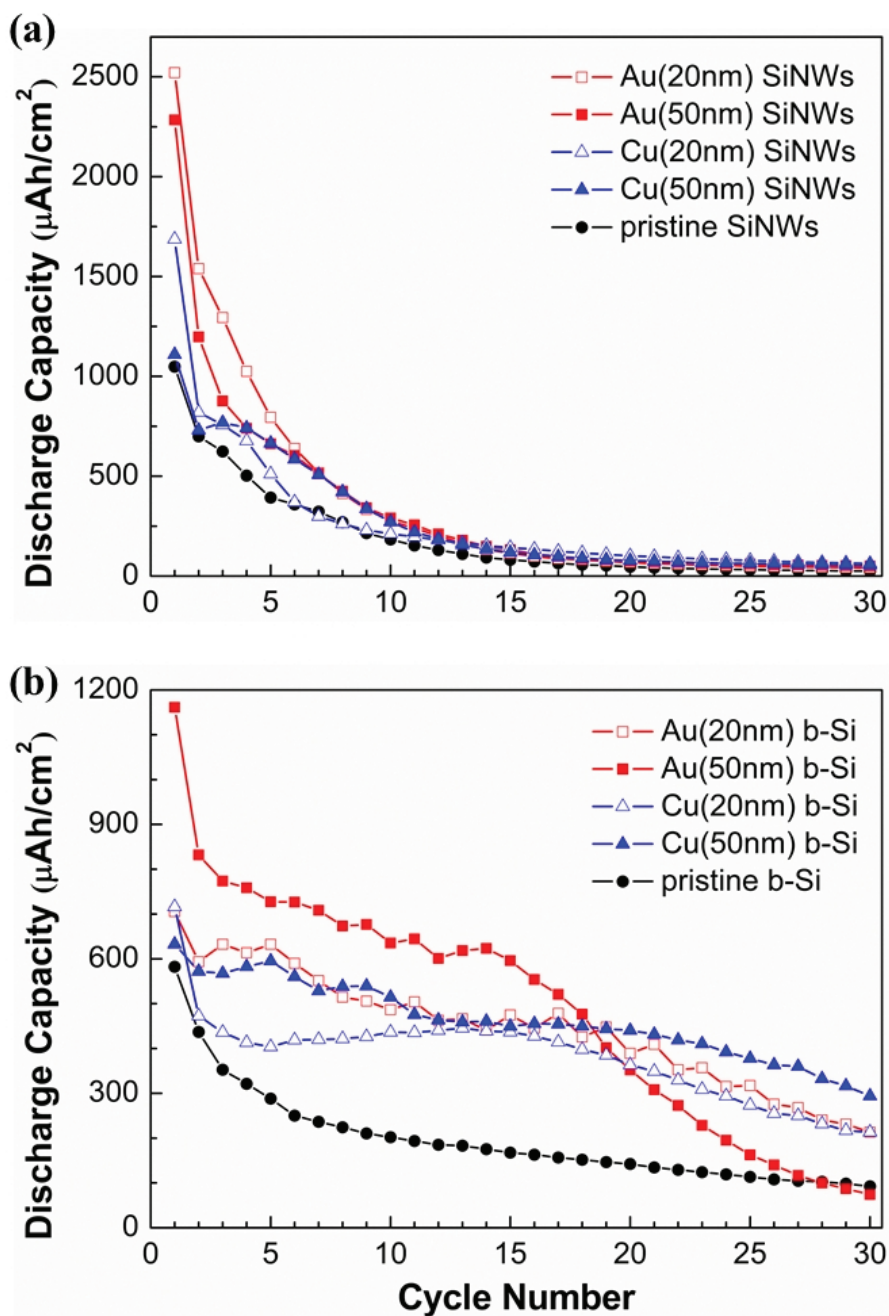


**Figure 5.7:** The comparison of discharge capacity vs. cycle number for (a) metal-coated SiNWs and (b) metal-coated b-Si electrodes, both in comparison with pristine electrodes. The cycle condition is the same as for Fig. 5.5 and Fig. 5.6.

**Table 5.1:** The discharge capacity and capacity retention of pristine b-Si, metal-coated b-Si electrodes after 20th and 30<sup>th</sup> cycles at constant current density of  $50 \mu A cm^{-2}$ .

Samples	Discharge capacity ( $\mu Ah cm^{-2}$ )			Capacity retention	
	1 <sup>st</sup> cycle	20 <sup>th</sup> cycle	30 <sup>th</sup> cycle	20 <sup>th</sup> cycle	30 <sup>th</sup> cycle
Pristine b-Si	582	142	98	24.4 %	16.8 %
Au(20) b-Si	705	389	231	55.2 %	32.8 %
Au(50) b-Si	1,160	352	87	30.3 %	7.5 %
Cu(20) b-Si	716	363	217	50.7 %	30.3 %
Cu(50) b-Si	633	440	316	<b>69.5 %</b>	<b>49.9 %</b>

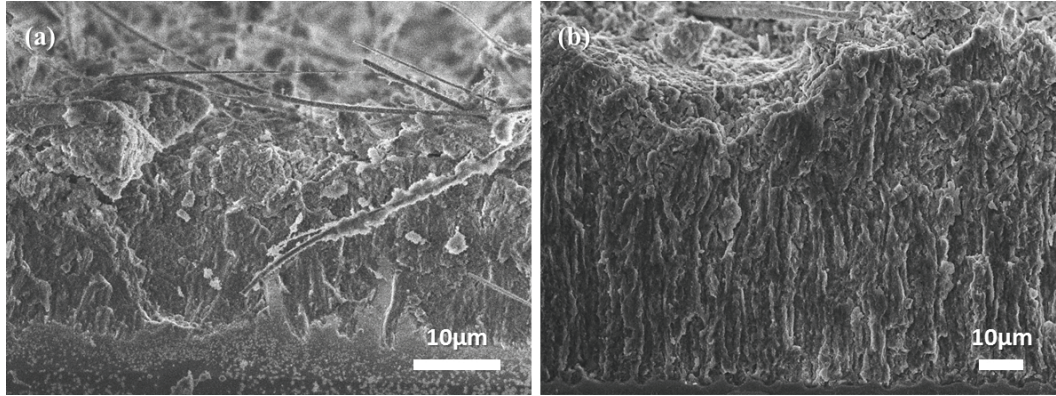


**Figure 5.8:** SEM images of (a) Au-coated and (b) Cu-coated b-Si electrode obtained after 50 cycles (the cell was charged to 2.0V).

### 5.2.3 Electrochemical characterization of M-Si anodes

Recently, it has been reported that metal silicide alloys composed of active or inactive metal material can supply a capacity enhancement and better cycle life of Si-based electrodes [101, 102, 103, 104, 105]. The metal coating can provide better electrical conductivity and less mechanical stress, which leads to the reversible reaction with Li ions at room temperature. In addition, it has been shown by those researches that the expected influences of metal coating are a stable SEI and alloy formation, resulting in the improvement of specific capacity and battery cycle life.

Therefore, the cyclic voltammetry (CV) the metal-coated nanostructured Si electrode is investigated in the potential range from 0.01 to 2.5 V (vs. Li/Li<sup>+</sup>) at a scan rate of 0.5 mV s<sup>-1</sup>. **Fig. 5.9** shows cyclic voltammogram (CV) profiles of Au-coated, and Cu-coated SiNWs electrodes. Both specimens have no peak in the potential range of 0.5–0.7 V during the first discharge process, indicating that a SEI layer is not formed on the SiNWs surface. Afterwards, the redox pair peaks appear, relating Li-insertion and extraction into silicon. The redox current peaks increase drastically upon cycles compared with that of pristine SiNWs (cf. **Fig. 3.5**). This clearly shows that the metal coating can provide better electrical conductivity and active reversible reactions between Li ions and silicon.

To further investigate the morphology and volume changes, metal-coated SiNWs are investigated by SEM imaging (see **Fig. 5.10**). Most of Si nanostructures become bent and twisted in structural morphology induced by amorphization due to volume expansion.



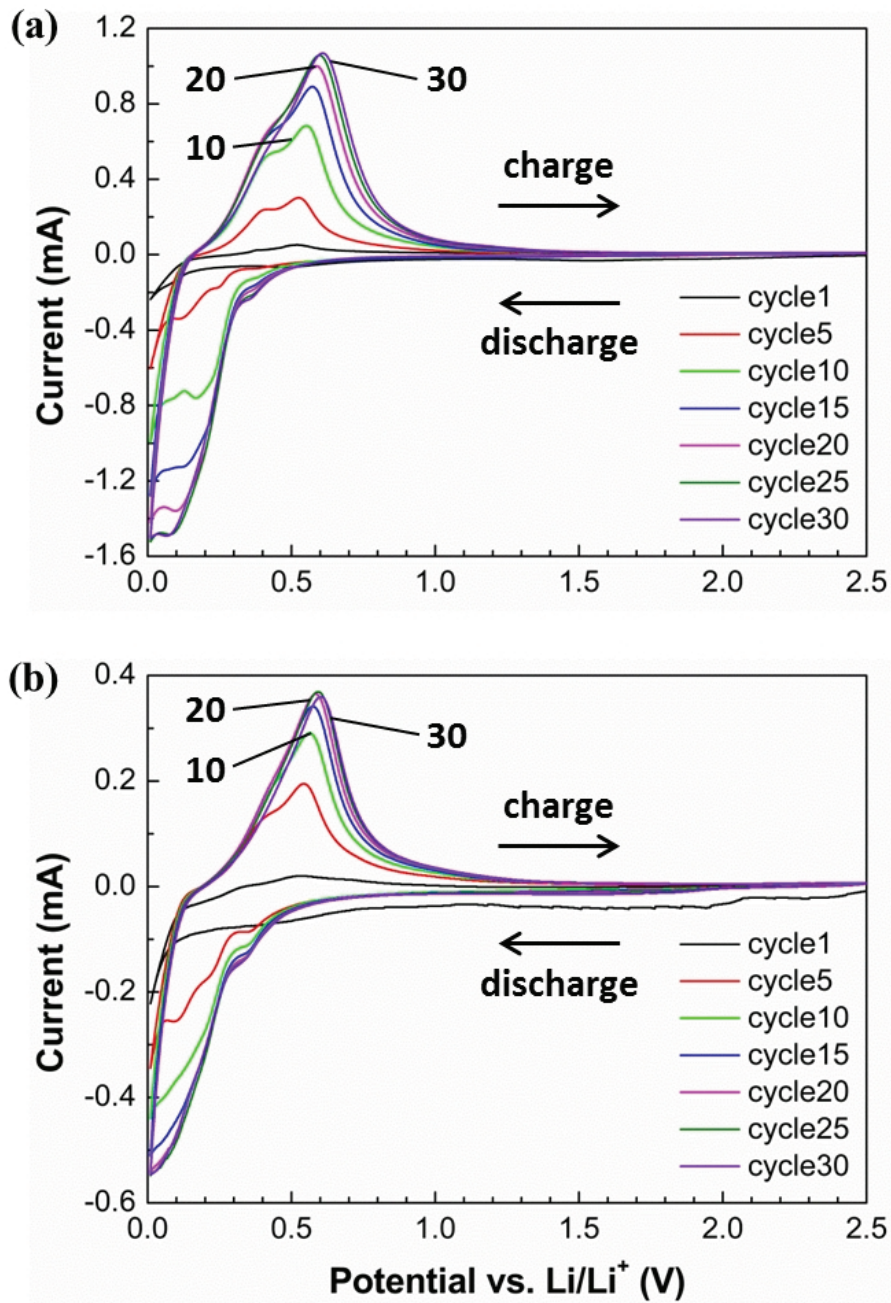


**Figure 5.9:** The Cyclic voltammogram for (a) Au-coated and (b) Cu-coated SiNWs electrode from 2.5 to 0.01 V (vs. Li/Li<sup>+</sup>) at scan rate of 0.5 mV s<sup>-1</sup>.

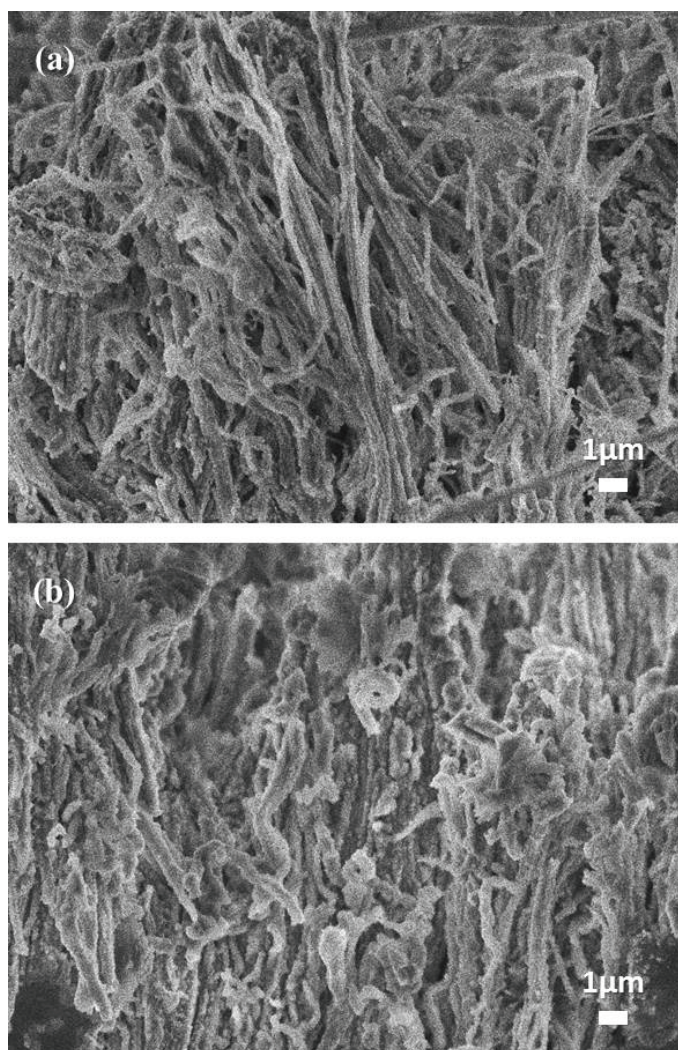


**Figure 5.10:** SEM images of (a) Au-coated and (b) Cu-coated SiNWs electrode obtained after 50 cycles (the cell was charged to 2.0 V).

In **Fig. 5.11(a)** for Au-coated b-Si, a characteristic peak at about  $\approx 0.15$  V indicates the onset of formation of Li–Si alloy during discharging and a peak at  $\approx 0.5$  V implies the Li–Si de-alloying during charging without a peak of SEI formation. These peaks have shifted to slightly higher potentials of  $\approx 0.25$ , and  $\approx 0.6$  V, respectively, during cycling. In the same manner, the Cu-coated b-Si electrode shows a similar phenomenon at the first cycle as shown in **Fig. 5.11(b)**. However, the following cycles show a different behavior. In case of Au-coated b-Si electrode, the current peak increased rapidly within about 15 cycles since Au as an active material leads to an increasing specific capacity by forming Au–Li–Si alloys, as mentioned before, and then stagnated or decreased a little after subsequent cycles. In contrast, the current peak of Cu-coated b-Si electrode increased gradually up to the 30<sup>th</sup> cycle. Note that Au metal is more active with Li–Si alloying/de-alloying than Cu metal at the beginning of cycles, resulting in the initial high specific capacity.



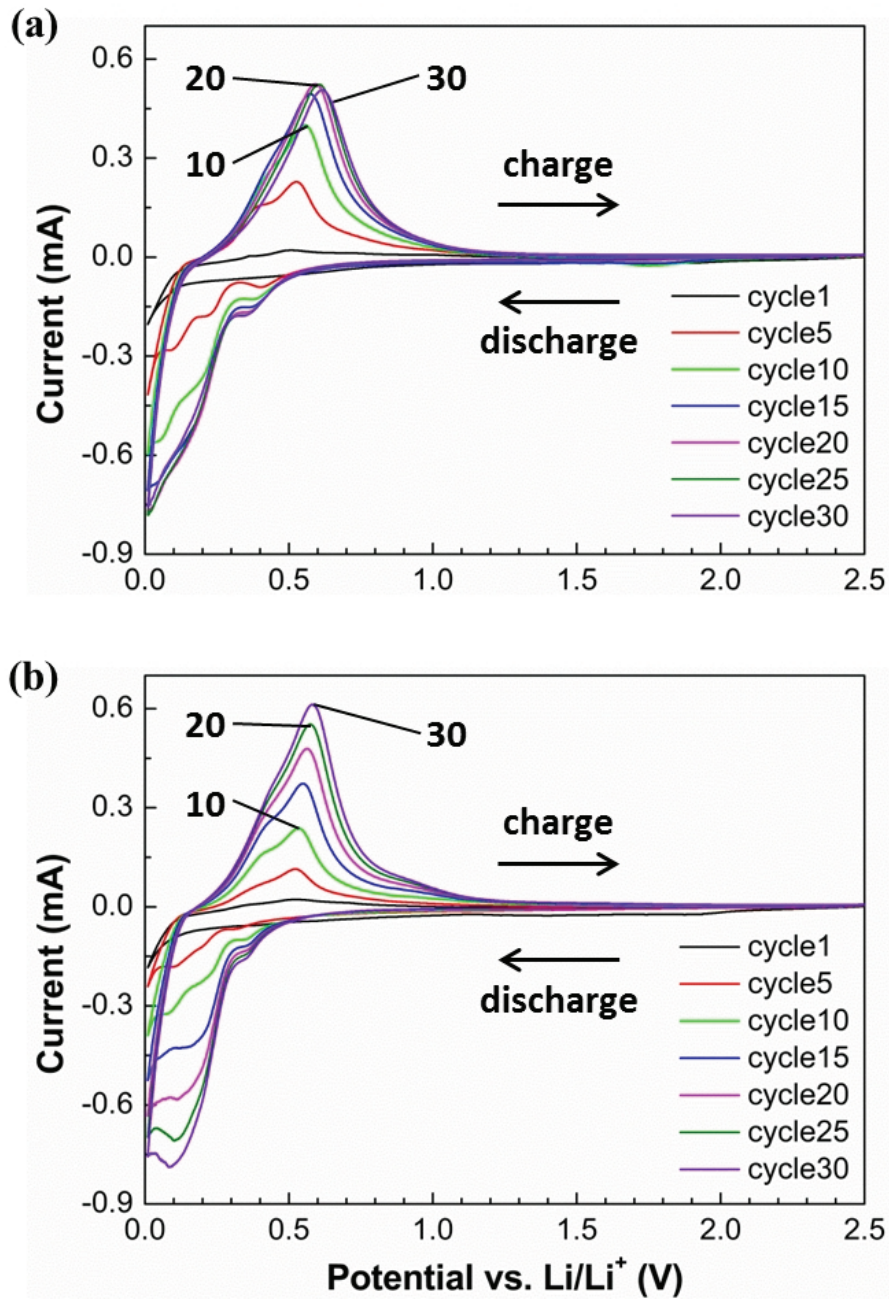


**Figure 5.11:** The Cyclic voltammogram for (a) Au-coated and (b) Cu-coated b-Si electrode from 2.5 to 0.01 V (vs. Li/Li<sup>+</sup>) at scan rate of  $0.5 \text{ mV s}^{-1}$ .



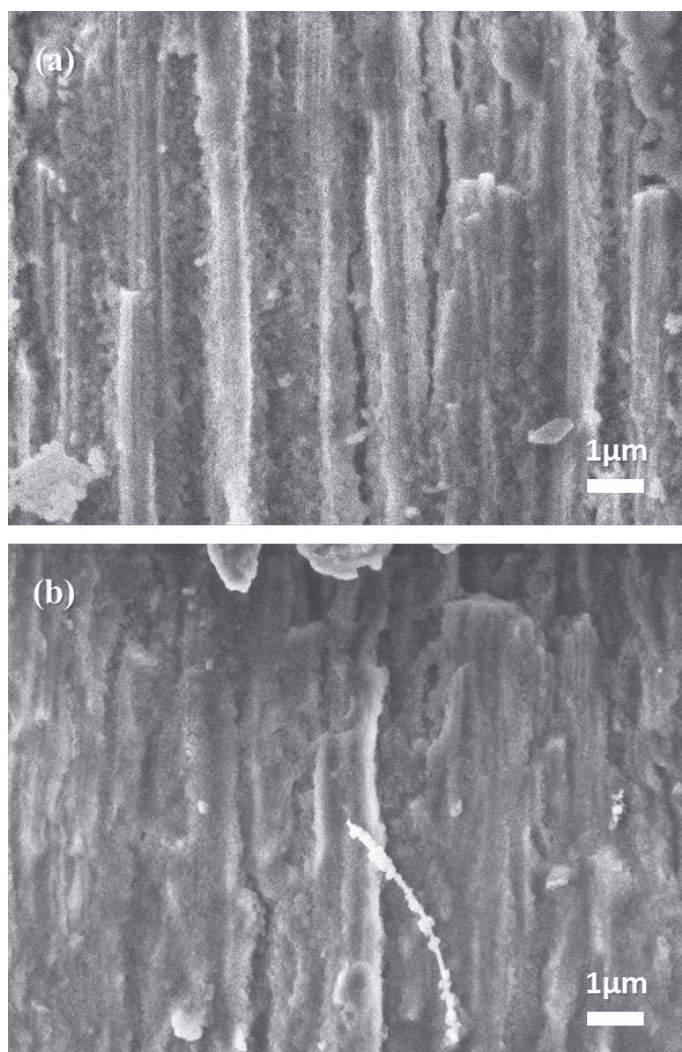


**Figure 5.12:** SEM images of (a) Au-coated and (b) Cu-coated b-Si electrode obtained after 50 cycles (the cell was charged to 2.0 V).

Through the SEM observation after cycling (see **Fig. 5.12**), I could confirm that influences of metal coatings are a stable SEI and alloy formation, and less mechanical stress, resulting in the improvement of specific capacity and battery cycle life.

### 5.3 Summary

In this chapter, complementary metal-oxide semiconductor (CMOS) compatible technology for fabrication of metal-coated nanostructured silicon electrodes as anodes on lithium-ion battery application was used. The Au and Cu coatings on silicon nanowire (SiNW) anodes, fabricated by one-step MaCE method and successive magnetron sputtering of metals, show rising specific capacity during the initial cycles. However, the capacity retention of metal-coated SiNWs is poor regardless of thickness of metal-coating in common with that of pristine SiNWs. The main reason for this result is that metal elements are only deposited on the upper part of the SiNWs due to the physical nature of the sputtering process caused by the high density of SiNWs.

In contrast, the metal coatings on nanostructured black silicon (b-Si) anodes, prepared by directly ICP-RIE method and successive magnetron sputtering of metals, show the enhancement of capacity and stability compared to conventional carbon-based technologies since metal coating is relatively uniform along the Si nanostructures with hardly any agglomeration. In particular, Cu-coated (50 nm) b-Si has the lowest capacity fading and the most stable capacity retention during cycling. The difference of the electrochemical properties of Cu and Au can be explained by the better adhesion of copper on silicon in line with recent in-situ experiments [106]. Furthermore, CV measurements confirm that redox activity and reactions regarding to Li-insertion/extraction of the metal-coated nanostructured Si increase significantly compared to pristine ones in both specimens.

Consequently, these results indicate that metal-coating on nanostructured Si can supply a capacity enhancement and better cycle life of Si-based electrodes by withstanding the mechanical stress caused by large volume expansion. However, metal elements should be distributed evenly along the nanostructures. In addition, a long-term cycle performance is influenced by the SEI formation than by the deformation and disruption of nanostructured Si. Therefore, the electrolyte stability has to be enhanced primarily for the improvement of Li-ion batteries instead of varying the Si nanostructures. This study suggests that the further improvements of the capacity can be made by continuing to optimize the electrolyte / anode interface.

# Chapter 6

## Conclusions and Outlook

### 6.1 Conclusions

Silicon has the highest theoretical specific capacity for lithium storage of  $4,200 \text{ mAh}\cdot\text{g}^{-1}$  (10 times higher than conventional graphite anode at  $372 \text{ mAh}\cdot\text{g}^{-1}$ ), and is drawing attention as a promising candidate for the anode material to achieve higher capacity and energy density demanded by ubiquitous power sources for mobile applications. However, the commercial use of silicon in lithium-ion batteries has been limited by the low cycle-life stability of bulk silicon. The large volume change during lithiation and delithiation (over 300 %) and the solid electrolyte interphase (SEI) on the Si surface lead to high internal stress, electrode pulverization and subsequent electrical loss. Moving from bulk to nanoscale morphologies of silicon anode has the potential to solve these limitations by managing the large stress associated with the expansion and contraction during electrochemical alloying. In this work, one dimensional (1D) nanostructured silicon was fabricated, aiming to understand the fundamental behavior of a reaction between lithium ions and silicon and to improve the capacity and long cycle life for lithium-ion rechargeable batteries.

I fabricated 1D silicon nanowires (SiNWs) via one-step metal assisted chemical etching (MaCE) in hydrofluoric acid with silver nitrate aqueous solution. The SiNWs electrodes were investigated in detail by high-resolution electron microscopy concerning the lithiation and delithiation process. After long-term charge/discharge cycles, only part of SiNWs was transformed into amorphous SiNWs induced by the different surface charge distribution in the individual SiNWs. Furthermore, the morphology change and the chemical composition of individual SiNWs were identified by TEM observation with EELS analysis, showing in the fact that lithiated SiNWs were composed of a crystalline Si core and an amorphous Li-Si alloys shell that is a mixture of crystalline Si and amorphous  $\text{SiO}_2$  as well. This composition might lead to constraints in subsequent formation of Li-Si alloys, resulting in limiting the cycling performance.

We also prepared 1D nanostructured black silicon (b-Si) via inductively coupled plasma reactive ion etching (ICP-RIE) using mixture gases comprising  $\text{SiF}_6$  as the etching gas and  $\text{C}_4\text{F}_8$  as the deposition gas. The microscopic structure strongly resembled other types of nanostructured silicon, with well-arranged nanostructures including large active surface area. However, the b-Si electrode showed a high irreversible capacity loss during the initial charge/discharge cycles and low capacity retention. The main reason for these poor features is the constant reformation of the SEI layer on the b-Si surface, suggesting that the cycle life of nanostructured Si electrodes is heavily influenced by the surface conditions compared to the nanostructure shapes. In regard to high C-rate (fast lithiation), the nanostructured Si region was detached from the Si substrate caused by mechanical stress in bulk Si substrate owing to the kinetics difference and phase transformation.

Lastly, I fabricated metal-coated nanostructured Si via successive magnetron sputtering of metals as anodes for lithium-ion microbatteries. For comparison and evaluation of metallic additive materials, gold (Au) as a representative active metal material and copper (Cu) as an inactive metal material were used, respectively. The metal coatings on b-Si anodes show the enhancement of capacity and cycle stability compared to metal-coated SiNWs anodes since metal coating is relatively uniform along the Si nanostructures with hardly any agglomeration. In particular, Cu-coated (50 nm) b-Si has the lowest capacity fading and most stable capacity retention during cycling. The results indicate that metal-coating on nanostructured Si can supply a capacity enhancement and better cycle life of Si-based electrodes by withstanding the mechanical stress and increasing the electric conductivity.

## 6.2 Suggestions and Recommendations

The potential scope for nanostructured Si anodes is great in capacity enhancement and long-term cycle life for lithium-ion batteries considering conventional cathodes and electrolytes. However, the larger surface-to-volume ratio can aggravate the reaction with the electrolyte and increase the SEI layer formation during charge/discharge processes. Based on the outcome of this study, future research should explore in the following areas:

(1) Nanoscale complex design: Si-based anodes should offer more structurally and compositionally complex nanostructures with void/free space. In addition, the existence of conductive material such as black carbon allows an increased electrical contact and serves as a barrier to further electrolyte decomposition.

(2) Stable SEI layer: the nature of the SEI on Si-based anodes needs to be thoroughly studied, which will lead to improvements in coulombic efficiency. Furthermore, using electrolyte additives for build-up of stable artificial SEI layer could assure the long-term cycle life of Si-based anodes.

(3) Practical application: methods of packing nanostructured Si and understanding degradation mechanisms at the whole cell are necessary. The scalability, manufacturability, and cost of the nanostructured Si will also be important concerning the potential large-scale energy applications of lithium-ion rechargeable batteries, such as EVs, HEV, and electrical power storage.

It is believed that the present results and continual development of these and other strategies and associated electrochemical analysis will lead to the practical and advanced applications of Si-based anodes in real lithium-ion rechargeable batteries.

# Bibliography

- [1] J-M. Tarascon, A. Michel: *Issues and challenges facing rechargeable lithium batteries*; Nature 414(6861) (2001) 359-367.
- [2] *Lithium Battery Energy Storage (LIBES) Publications*; Technological Research Association, Tokyo (1994).
- [3] M. K. Aydinol, G. J. Ceder: *FirstPrinciples Prediction of Insertion Potentials in LiMn Oxides for Secondary Li Batteries*; Journal of the Electrochemical Society 144(11) (1997) 3832-3835.
- [4] N. Imanishi, Y. Takeda, O. Yamamoto: *Lithium Ion Batteries: Fundamentals and Performance*; Wiley-VCH, Weinheim (1998) 98.
- [5] B. Scrosati, J. Garche: *Lithium batteries: Status, prospects and future*; Journal of Power Sources 195(9) (2010) 2419-2430.
- [6] R. Kötz, M. Carlen: *Principles and applications of electrochemical capacitors*; Electrochimica Acta 45(15) (2000) 2483-2498.
- [7] J. B. Holt, L. Himmel: *Marker Techniques for Studying the Mechanism of Scaling of Metals Based on the Use of the  $O^{18}$  ( $p, n$ )  $F^{18}$  Nuclear Reaction*; Journal of The Electrochemical Society 116(11) (1969) 1569-1580.
- [8] S. C. Lai: *Solid lithium-silicon electrode*; Journal of The Electrochemical Society 123 (1976) 1196.
- [9] W. Weppner, R. A. Huggins: *Electrochemical methods for determining kinetic properties of solids*; Annual Review of Materials Science 8(1) (1978) 269-311.
- [10] M. Holzapfel, H. Buqa, W. Scheifele, P. Novk, F.M. Petrat: *A new type of nano-sized silicon/carbon composite electrode for reversible lithium insertion*; Chemical communications 12 (2005) 1566-1568.
- [11] C. M. Park, J. H. Kim, H. Kim, H. J. Sohn: *Li-alloy based anode materials for Li secondary batteries*; Chemical Society Reviews 39(8) (2010) 3115-3141.

- [12] W. J. Zhang: *Lithium insertion/extraction mechanism in alloy anodes for lithium-ion batteries*; Journal of Power Sources 196(3) (2011) 877-885.
- [13] W. J. Zhang: *A review of the electrochemical performance of alloy anodes for lithium-ion batteries*; Journal of Power Sources 196(1) (2011) 13-24.
- [14] H. Li, X. Huang, L. Chen, Z. Wu, Y. Liang: *A high capacity nano Si composite anode material for lithium rechargeable batteries*; Electrochemical and solid-state letters 2(11) (1999) 547-549.
- [15] L. Chen, K. Wang, X. Xie, J. Xie: *Effect of vinylene carbonate (VC) as electrolyte additive on electrochemical performance of Si film anode for lithium ion batteries*; Journal of Power Sources 174(2) (2007) 538-543.
- [16] J. P. Maranchi, A. F. Hepp, P. N. Kumta: *High capacity, reversible silicon thin-film anodes for lithium-ion batteries*; Electrochemical and Solid-State Letters 6(9) (2003) A198-A201.
- [17] N. Tamura, R. Ohshita, M. Fujimoto, M. Kamino, S. Fujitani: *Advanced structures in electrodeposited tin base negative electrodes for lithium secondary batteries*; Journal of The Electrochemical Society 150(6) (2003) A679-A683.
- [18] T. D. Hatchard, J. R. Dahn: *In situ XRD and electrochemical study of the reaction of lithium with amorphous silicon*; Journal of The Electrochemical Society 151(6) (2004) A838-A842.
- [19] M. N. Obrovac, L. Christensen: *Structural changes in silicon anodes during lithium insertion/extraction*; Electrochemical and Solid-State Letters 7(5) (2004) A93-A96.
- [20] J. Li, J. R. Dahn: *An in situ X-ray diffraction study of the reaction of Li with crystalline Si*; Journal of The Electrochemical Society 154(3) (2007) A156-A161.
- [21] L. Y. Beaulieu, T. D. Hatchard, A. Bonakdarpour, M. D. Fleischauer, J. R. Dahn: *Reaction of Li with alloy thin films studied by in situ AFM*; Journal of The Electrochemical Society 150(11) (2003) A1457-A1464.
- [22] V. L. Chevrier, J. W. Zwanziger, J. R. Dahn: *First principles study of LiSi crystalline phases: Charge transfer, electronic structure, and lattice vibrations*; Journal of Alloys and Compounds 496(1) (2010) 25-36.
- [23] M. H. Braga, L. F. Malheiros, I. Ansara: *Thermodynamic assessment of the Li-Si system*; Journal of phase equilibria 16(4) (1995) 324-330.
- [24] N. Tamura, R. Ohshita, M. Fujimoto, M. Kamino, S. Fujitani: *Advanced structures in electrodeposited tin base negative electrodes for lithium secondary batteries*; Journal of The Electrochemical Society 150(6) (2003) A679-A683.

- [25] M. N. Obrovac, L. Christensen, D. B. Le, J. R. Dahn: *Alloy design for lithium-ion battery anodes*; Journal of The Electrochemical Society 154(9) (2007) A849-A855.
- [26] J. R. Szczech, S. Jin: *Nanostructured silicon for high capacity lithium battery anodes*; Energy & Environmental Science 4(1) (2011) 56-72.
- [27] N. Ding, J. Xu, Y. Yao, G. Wegner, I. Lieberwirth, C. Chen: *Improvement of cyclability of Si as anode for Li-ion batteries*; Journal of power sources 192(2) (2009) 644-651.
- [28] M. Green, E. Fielder, B. Scrosati, M. Wachtler, J. S. Moreno: *Structured silicon anodes for lithium battery applications*; Electrochemical and Solid-State Letters 6(5) (2003) A75-A79.
- [29] J. H. Ryu, J. W. Kim, Y. E. Sung, S. M. Oh: *Failure modes of silicon powder negative electrode in lithium secondary batteries*; Electrochemical and solid-state letters 7(10) (2004) A306-A309.
- [30] C. M. Park, H. J. Sohn: *A mechano-and electrochemically controlled SnSb/C nanocomposite for rechargeable Li-ion batteries*; Electrochimica Acta 54(26) (2009) 6367-6373.
- [31] M. S. Park, G. X. Wang, H. K. Liu, S. X. Dou: *Electrochemical properties of Si thin film prepared by pulsed laser deposition for lithium ion micro-batteries*; Electrochimica acta 51(25) (2006) 5246-5249.
- [32] H. Xia, S. Tang, L. Lu: *Properties of amorphous Si thin film anodes prepared by pulsed laser deposition*; Materials research bulletin 42(7) (2007) 1301-1309.
- [33] C. K. Chan, H. Peng, G. Liu, K. McIlwrath, X. F. Zhang, R. A. Huggins, Y. Cui: *High-performance lithium battery anodes using silicon nanowires*; Nature nanotechnology 3(1) (2007) 31-35.
- [34] U. Kasavajjula, C. Wang, A. J. Appleby: *Nano-and bulk-silicon-based insertion anodes for lithium-ion secondary cells*; Journal of Power Sources 163(2) (2007) 1003-1039.
- [35] H. Li, et al.: *The crystal structural evolution of nano-Si anode caused by lithium insertion and extraction at room temperature*; Solid State Ionics 135(1) (2000) 181-191.
- [36] O. Mao, R. L. Turner, I. A. Courtney, B. D. Fredericksen, M. I. Buckett, L. J. Krause, J. R. Dahn: *Active/Inactive nanocomposites as anodes for LiIon batteries*; Electrochemical and Solid-State Letters 2(1) (1999) 3-5.
- [37] J. Yang, B. F. Wang, K. Wang, Y. Liu, J. Y. Xie, Z. S. Wen: *Si/C composites for high capacity lithium storage materials*; Electrochemical and Solid-State Letters 6(8) (2003) A154-A156.



- [38] J. Cho: *Porous Si anode materials for lithium rechargeable batteries*; Journal of Materials Chemistry 20(20) (2010) 4009-4014.
- [39] K. Q. Peng, Y. J. Yan, S. P. Gao, J. Zhu: *Synthesis of large-area silicon nanowire arrays via self-assembling nanoelectrochemistry*; Advanced Materials 14(16) (2002) 1164.
- [40] X. Li: *Metal assisted chemical etching for high aspect ratio nanostructures: A review of characteristics and applications in photovoltaics*; Current Opinion in Solid State and Materials Science 16(2) (2012) 71-81.
- [41] K. Peng, Y. Yan, S. Gao, J. Zhu: *Dendrite Assisted Growth of Silicon Nanowires in Electroless Metal Deposition*; Advanced Functional Materials 13(2) (2003) 127-132.
- [42] K. Peng, H. Fang, J. Hu, Y. Wu, J. Zhu, Y. Yan, S. Lee: *Metal Particle Induced, Highly Localized Site Specific Etching of Si and Formation of Single Crystalline Si Nanowires in Aqueous Fluoride Solution*; Chemistry-A European Journal 12(30) (2006) 7942-7947.
- [43] Z. Huang, N. Geyer, P. Werner, J. De Boor, U. Gösele: *Metal Assisted Chemical Etching of Silicon: A Review*; Advanced materials 23(2) (2011) 285-308.
- [44] Z. Huang, H. Fang, J. Zhu: *Fabrication of silicon nanowire arrays with controlled diameter, length, and density*; Advanced Materials 19(5) (2007) 744-748.
- [45] A. I. Hochbaum, D. Gargas, Y. J. Hwang, P. Yang: *Single crystalline mesoporous silicon nanowires*; Nano letters 9(10) (2009) 3550-3554.
- [46] Y. Qu, L. Liao, Y. Li, H. Zhang, Y. Huang, X. Duan: *Electrically conductive and optically active porous silicon nanowires*; Nano letters 9(12) (2009) 4539-4543.
- [47] K. Q. Peng, et al: *Fabrication of Single Crystalline Silicon Nanowires by Scratching a Silicon Surface with Catalytic Metal Particles*; Advanced Functional Materials 16(3) (2006) 387-394.
- [48] N. Geyer, B. Fuhrmann, Z. Huang, J. de Boor, H. S. Leipner, P. Werner: *Model for the mass transport during metal-assisted chemical etching with contiguous metal films as catalysts*; The Journal of Physical Chemistry C 116(24) (2012) 13446-13451.
- [49] C. Y. Chen, C. S. Wu, C. J. Chou, T. J. Yen: *Morphological Control of Single Crystalline Silicon Nanowire Arrays near Room Temperature*; Advanced Materials 20(20) (2008) 3811-3815.

- [50] H. Chen, H. Wang, X. H. Zhang, C. S. Lee, S. T. Lee: *Wafer-scale synthesis of single-crystal zigzag silicon nanowire arrays with controlled turning angles*; Nano letters 10(3) (2010) 864-868.
- [51] E. S. Kolesar Jr, M. W. Carver: *Deep anisotropic etching of tapered channels in (110)-oriented silicon*; Chemistry of Materials 1(6) (1989) 634-639.
- [52] S. Tachi, K. Tsujimoto, S. Okudaira: *Low-temperature reactive ion etching and microwave plasma etching of silicon*; Applied physics letters 52(8) (1988) 616-618.
- [53] I. W. Rangelow: *Critical tasks in high aspect ratio silicon dry etching for microelectromechanical systems*; Journal of Vacuum Science & Technology A 21(4) (2003) 1550-1562.
- [54] H. Jansen, M. de Boer, R. Legtenberg, M. Elwenspoek: *The black silicon method: a universal method for determining the parameter setting of a fluorine-based reactive ion etcher in deep silicon trench etching with profile control*; Journal of Micromechanics and Microengineering 5(2) (1995) 115.
- [55] A. A. Ayón, X. Zhang, R. Khanna: *Anisotropic silicon trenches 300–500 $\mu$ m deep employing time multiplexed deep etching (TMDE)*; Sensors and Actuators A: Physical 91(3) (2001) 381-385.
- [56] S. A. McAuley, H. Ashraf, L. Atabo, A. Chambers, S. Hall, J. Hopkins, G. Nicholls: *Silicon micromachining using a high-density plasma source*; Journal of physics d: applied physics 34(18) (2001) 2769.
- [57] H. V. Jansen, M. J. de Boer, S. Unnikrishnan, M. C. Louwerse, M. C. Elwenspoek: *Black silicon method X: a review on high speed and selective plasma etching of silicon with profile control: an in-depth comparison between Bosch and cryostat DRIE processes as a roadmap to next generation equipment*; Journal of micromechanics and microengineering 19(3) (2009) 033001.
- [58] K. Tsujimoto, S. Tachi, K. Ninomiya, K. Suzuki, S. Okudaira, S. Nishimatsu: *A New Side Wall Protection Technique in Microwave Plasma Etching Using a Chopping Method*; 18th (1986 International) Conference of Solid State Devices and Materials, Tokyo (1986) 229-232.
- [59] B. Volland, F. Shi, P. Hudek, H. Heerlein, I. W. Rangelow: *Dry etching with gas chopping without rippled sidewalls*; Journal of Vacuum Science & Technology B 17(6) (1999) 2768-2771.
- [60] X. Li, L. Ling, X. Hua, M. Fukasawa, G. S. Oehrlein, M. Barela, H. M. Anderson: *Effects of Ar and O<sub>2</sub> additives on SiO<sub>2</sub> etching in C<sub>4</sub>F<sub>8</sub>-based plasmas*; Journal of Vacuum Science and Technology—Section A—Vacuum Surfaces and Films 21(1) (2003) 284-293.

- [61] C. M. A. Brett, A. M. O. Brett: *Electrochemistry principles, methods and applications*; OXFORD UNIVERSITY PRESS, Bookcraft (Bath) Ltd., Midsomer Norton, Avon (1993)
- [62] W. K. Beak, S. M. Park: *Electrochemistry*; CheongMonGak Publishing Co., Paju-si, Gyeonggi-do (2003)
- [63] J. Wang: *Analytical Electrochemistry, 3rd edn*; John Wiley & Sons (2006).
- [64] *Battery Performance Characteristics*; Electropaedia, <http://www.mpoweruk.com/performance.htm>.
- [65] C. Chartier, S. Bastide, C. Lévy-Clément: *Metal-assisted chemical etching of silicon in HF-H<sub>2</sub>O<sub>2</sub>*; *Electrochimica Acta* 53(17) (2008) 5509-5516.
- [66] *Joint Committee on Powder Diffraction Standards (JCPDS) Card No. 27-1402*.
- [67] K. Kang, et al.: *Maximum Li storage in Si nanowires for the high capacity three-dimensional Li-ion battery*; *Applied physics letters* 96(5) (2010) 053110.
- [68] H. C. Shin, J. A. Corno, J. L. Gole, M. Liu: *Porous silicon negative electrodes for rechargeable lithium batteries*; *Journal of power sources* 139(1) (2005) 314-320.
- [69] M. Ge, J. Rong, X. Fang, C. Zhou: *Porous doped silicon nanowires for lithium ion battery anode with long cycle life*; *Nano letters* 12(5) (2012) 2318-2323.
- [70] M. N. Obrovac, L. J. Krause: *Reversible cycling of crystalline silicon powder*; *Journal of The Electrochemical Society* 154(2) (2007) A103-A108.
- [71] X. H. Liu, et al.: *Ultrafast electrochemical lithiation of individual Si nanowire anodes*; *Nano letters* 11(6) (2011) 2251-2258.
- [72] L. F. Cui, R. Ruffo, C. K. Chan, H. Peng, Y. Cui: *Crystalline-amorphous core shell silicon nanowires for high capacity and high current battery electrodes*; *Nano Letters* 9(1) (2008) 491-495.
- [73] H. Jung, M. Park, Y. G. Yoon, G. B. Kim, S. K. Joo: *Amorphous silicon anode for lithium-ion rechargeable batteries*; *Journal of power sources* 115(2) (2003) 346-351.
- [74] L. Enze: *The distribution function of surface charge density with respect to surface curvature*; *Journal of Physics D: Applied Physics* 19(1) (1986) 1.
- [75] X. H. Liu, et al.: *Anisotropic swelling and fracture of silicon nanowires during lithiation*; *Nano letters* 11(8) (2011) 3312-3318.

- [76] P. Limthongkul, Y. I. Jang, N. J. Dudney, Y. M. Chiang: *Electrochemically-driven solid-state amorphization in lithium-silicon alloys and implications for lithium storage*; Acta Materialia 51(4) (2003) 1103-1113.
- [77] P. Limthongkul, Y. I. Jang, N. J. Dudney, Y. M. Chiang: *Electrochemically-driven solid-state amorphization in lithiummetal anodes*; Journal of power sources 119 (2003) 604-609.
- [78] P. E. Batson: *Current trends for EELS studies in physics*; Microscopy Microanalysis Microstructures 2(2-3) (1991) 395-402.
- [79] J. Yang, Y. Takeda, N. Imanishi, C. Capiglia, J.Y. Xie, O. Yamamoto: *SiO<sub>x</sub>-based anodes for secondary lithium batteries*; Solid State Ionics 152 (2002) 125-129.
- [80] K. Nishio, S. Tagawa, T. Fukushima, H. Masuda: *Highly ordered nanoporous Si for negative electrode of rechargeable lithium-ion battery*; Electrochemical and Solid-State Letters 15(4) (2012) A41-A44.
- [81] J. Li, J. R. Dahn: *An in situ X-ray diffraction study of the reaction of Li with crystalline Si*; Journal of The Electrochemical Society 154(3) (2007) A156-A161.
- [82] J. F. Moulder, W. F. Stickle, P. E. Sobol, K. D. Bomben: *Handbook of X-ray Photoelectron Spectroscopy*; Physical Electronics, Inc., Eden Prairie, Minnesota 55344 (1995)
- [83] C. K. Chan, R. Ruffo, S. S. Hong, Y. Cui: *Surface chemistry and morphology of the solid electrolyte interphase on silicon nanowire lithium-ion battery anodes*; Journal of Power Sources 189(2) (2009) 1132-1140.
- [84] L. Feng, Y. Song, J. Zhai, B. Liu, J. Xu, L. Jiang, D. Zhu: *Creation of a superhydrophobic surface from an amphiphilic polymer*; Angewandte Chemie 115(7) (2003) 824-826.
- [85] N. Politakos, G. Kortaberria, I. Zalakain, A. Avgeropoulos, I. Mondragon: *Modified diblock copolymer bearing fluoro groups and evaluation of its hydrophobic properties*; WILEYVCH Verlag, In Macromolecular Symposia 321(1) (2012) 53-58).
- [86] A. P. Modica, J. E. LaGraff: *Decomposition and oxidation of C<sub>2</sub>F<sub>4</sub> behind shock waves*; The Journal of Chemical Physics 43(9) (1965) 3383-3392.
- [87] N. K. Srinivasan, M. C. Su, J. V. Michael, A. W. Jasper, S. J. Klippenstein, L. B. Harding: *Thermal Decomposition of CF<sub>3</sub> and the Reaction of CF<sub>2</sub> + OH → CF<sub>2</sub>O + H*; The Journal of Physical Chemistry A 112(1) (2008) 31-37.

- [88] X. Sun, H. Huang, K. L. Chu, Y. Zhuang: *Anodized macroporous silicon anode for integration of lithium-ion batteries on chips*; Journal of electronic materials 41(9) (2012) 2369-2375.
- [89] R. Ruffo, S. S. Hong, C. K. Chan, R. A. Huggins, Y. Cui: *Impedance analysis of silicon nanowire lithium ion battery anodes*; The Journal of Physical Chemistry C 113(26) (2009) 11390-11398.
- [90] L. Kong, G. Duan, G. Zuo, W. Cai, Z. Cheng: *Rattle-type Au@TiO<sub>2</sub> hollow microspheres with multiple nanocores and porous shells and their structurally enhanced catalysis*; Materials Chemistry and Physics 123(2) (2010) 421-426.
- [91] S. K. Soni, B. W. Sheldon, X. Xiao, A. Tokranov: *Thickness effects on the lithiation of amorphous silicon thin films*; Scripta Materialia 64(4) (2011) 307-310.
- [92] J. Li, A. K. Dozier, Y. Li, F. Yang, Y. T. Cheng: *Crack pattern formation in thin film lithium-ion battery electrodes*; Journal of The Electrochemical Society 158(6) (2011) A689-A694.
- [93] X. H. Liu, L. Zhong, S. Huang, S. X. Mao, T. Zhu, J. Y. Huang: *Size-dependent fracture of silicon nanoparticles during lithiation*; Acs Nano 6(2) (2012) 1522-1531.
- [94] M. Roberts, et al.: *3D lithium ion batteries from fundamentals to fabrication*; Journal of Materials Chemistry 21(27) (2011) 9876-9890.
- [95] X. Chen, Y. Du, N. Q. Zhang, K. N. Sun: *3D self-supported nanoarchitected arrays electrodes for lithium-ion batteries*; Journal of Nanomaterials 2012, 1.
- [96] M. Armand, J. M. Tarascon: *Building better batteries*; Nature 451(7179) (2008) 652-657.
- [97] T. Song, et al.: *Arrays of sealed silicon nanotubes as anodes for lithium ion batteries*; Nano letters 10(5) (2010) 1710-1716.
- [98] O. Mao, J. R. Dahn: *Mechanically Alloyed Sn-Fe(-C) Powders as Anode Materials for Li-Ion Batteries: III. Sn<sub>2</sub>Fe:SnFe<sub>3</sub>C Active/Inactive Composites*; Journal of The Electrochemical Society 146(2) (1999) 423-427.
- [99] J. I. Lee, N. S. Choi, S. Park: *Highly stable Si-based multicomponent anodes for practical use in lithium-ion batteries*; Energy & Environmental Science 5(7) (2012) 7878-7882.
- [100] S. R. Gowda, et al.: *Three-dimensionally engineered porous silicon electrodes for Li ion batteries*; Nano letters 12(12) (2012) 6060-6065.

- [101] E. OsseiWusu, A. Cojocar, H. Hartz, J. Carstensen, H. Föll: *Silicon nanowires made via macropore etching for superior Li ion batteries*; *physica status solidi (a)* 208(6) (2011) 1417-1421.
- [102] V. A. Sethuraman, K. Kowolik, V. Srinivasan: *Increased cycling efficiency and rate capability of copper-coated silicon anodes in lithium-ion batteries*; *Journal of Power Sources* 196(1) (2011) 393-398.
- [103] A. Vlad, A. L. M. Reddy, A. Ajayan, N. Singh, J. F. Gohy, S. Melinte, P. M. Ajayan: *Roll up nanowire battery from silicon chips*; *Proceedings of the National Academy of Sciences* 109(38) (2012) 15168-15173.
- [104] M. Thakur, M. Isaacson, S. L. Sinsabaugh, M. S. Wong, S. L. Biswal: *Gold-coated porous silicon films as anodes for lithium ion batteries*; *Journal of Power Sources* 205 (2012) 426-432.
- [105] F. Luo, G, Chu, H. Li, L. Chen, X. Huang: *Research on Nano-Si/C Nanocomposites as Anode for Li-Ion Batteries*; 17th International Meeting on Lithium Batteries (IMLB 2014), Como, Italy (2014)
- [106] M. T. McDowell, S. W. Lee, C. Wang, Y. Cui: *The effect of metallic coatings and crystallinity on the volume expansion of silicon during electrochemical lithiation/delithiation*; *Nano Energy* 1(3) (2012) 401-410.

## Publications

1. **Gibaek Lee**, Stefan L. Schweizer, Ralf B. Wehrspohn,  
*CMOS-compatible metal-stabilized nanostructured Si as anodes for lithium-ion microbatteries*; Nanoscale research letters 9(1) (2014) 1-8.
2. **Gibaek Lee**, Stefan L. Schweizer, Ralf B. Wehrspohn,  
*Electrochemical characteristics of plasma-etched black silicon as anodes for Li-ion batteries*; Journal of Vacuum Science & Technology A 32(6) (2014) 061202.
3. **Gibaek Lee**, Stefan L. Schweizer, Ralf B. Wehrspohn,  
*Microstructural characterization of Li insertion in individual silicon nanowires*; Applied Physics A 117(3) (2014) 973-979.
4. K. K. Poornesh, C. D. Cho, **G. B. Lee**, Y. S. Tak,  
*Gradation of mechanical properties in gas-diffusion electrode. Part 2: Heterogeneous carbon fiber and damage evolution in cell layers*; Journal of Power Sources 195(9) (2010) 2718-2730.
5. K. K. Poornesh, C. D. Cho, **G. B. Lee**, Y. S. Tak,  
*Gradation of mechanical properties in gas diffusion electrode. Part 1: Influence of nano-scale heterogeneity in catalyst layer on interfacial strength between catalyst layer and membrane*; Journal of Power Sources 195(9) (2010) 2709-2717.
6. J. Kim, J. Lee, **G. Lee**, Y. Tak,  
*Direct relationship between carbon corrosion and cathode potential during fuel starvation in PEMFC*; ECS Transactions 16(2) (2008) 961-968.

## International Symposiums

### Selected presentations

1. 78<sup>th</sup> Deutsche Physikalische Gesellschaft (DPG) Spring Meeting, Dresden, Germany, March 2014:  
*Electrochemical characteristic of nanostructured black silicon as anode for lithium-ion batteries.*
2. 6<sup>th</sup> International Conference on Polymer Batteries and Fuel Cells (PBFC 2013), Ulm, Germany, June 2013:  
*Microstructural mechanism of Li cycling in individual silicon nanowire for Li-ion battery.*

3. 2013 MRS Spring Meeting & Exhibit, San Francisco, USA, April 2014:  
*Electrochemical analysis of lithiation/delithiation in silicon nanowires as anode for lithium-ion batteries.*
4. 16<sup>th</sup> International Meeting on Lithium Batteries (IMLB 2012), Jeju, South Korea, June 2012:  
*Electrochemical analysis of silicon nanowires anodes in lithium-ion batteries.*
5. 3<sup>rd</sup> German-French Summer School on Electrochemistry & Nanotechnologies, Porquerolles, France, September 2011:  
*Electrochemical analysis of SiNWs anodes filled with copper by electrodeposition in lithium-ion batteries.*
6. 4<sup>th</sup> International Conference on Polymer Batteries and Fuel Cells (PBFC 2009), Yokohama, Japan, August 2009:  
*Stability of Various Cathode Carbon Supports during Fuel Starvation.*
7. 3<sup>rd</sup> Asian Conference on Electrochemical Power Sources (ACEPS-3), Korea Univ., South Korea, November 2008:  
*Relationship Between Degradation of Carbon Support and Cathode Potential During Start-Up/Shut-Down Procedure in PEMFC.*



## Acknowledgements

First and foremost, my heartfelt gratitude goes out to my supervisor, Prof. Dr. Ralf B. Wehrspohn, for successful completion of my dissertation. I am so honored to join in his research group as a PhD student, and worked with him to set up the lab and equipment from scratch. His effort, encouragement, guidance and support helped me greatly in my studies as well as successful completion of my research.

I also wish to thank my previous supervisor, Prof. Yongsug Tak. He is the person who guided me to electrochemistry in nanomaterials during my master degree. Also special thanks to my senior, Prof. Jinsub Choi who strongly supported and assisted my research.

I would like to thank to Dr. Stefan L. Schweizer for all the non-academic and academic guidance and support that he has given to me during my graduate studies. This work would not have been completed without his kindly discussions and friendly support. In addition I wish to thanks Dr. Michael Krause (IWMH), Dr. Paul-Tiberiu Miclea (CSP), Frau Claudia Stehr, Frau Doreen Rawald (Fachgruppe  $\mu$ MD) for their helpful material characterization, scientific discussion and help various administrative and social issues.

My sincere thanks go to all my members of microstructure-based Material Design ( $\mu$ MD) group for creating a pleasant working environment in Halle. I learned a lot from everyone both scientifically and personally, and shared so many unforgettable moments with you. Technical assistance from the people in the Fraunhofer Institute for Mechanics of materials IWM (IWMH) and Center for Silicon-Photovoltaics (CSP), such as Dr. Volker Naumann (XPS) and Dr. Bernd Ahrens (XRD) are gratefully acknowledged.

Finally, words cannot express my gratitude for unwavering support for my family. I wish to express my deepest respect and special thanks to my parents for their continue support, understanding, and love during my study to enable the completion of this thesis.

# Curriculum Vitae

## Personal Information

- Name: Gibaek Lee
- Address: 55, Siheung-daero 51-gil, Geumcheon-gu, Seoul, Republic of Korea
- E-mail: gibaek.lee6@gmail.com
- Date of Birth: May 11, 1979 in Seoul, Republic of Korea

## Education

- **Ph.D.** (Sep. 2010 – Nov. 2015)
  - Microsystems Characterization, Fraunhofer Institute for Mechanics of Materials IWM, Halle, Germany
  - Institut für Physik, Fachgruppe  $\mu$ MD, Martin-Luther-Universität Halle-Wittenberg, Halle, Germany
  - Supervisor: Prof. Dr. Ralf B. Wehrspohn
- **M.E.** (Mar. 2008 – Aug. 2010)
  - Department of Chemical Engineering, Inha University, Inchoen, Republic of Korea
  - Thesis title: *Electrochemical Analysis of Pt/C Catalysts with Different Carbon Supports in PEMFCs*
  - Supervisor: Prof. Yongsug Tak
- **B.E.** (Mar. 1999 – Feb. 2008)
  - Department of Chemical Engineering, Inha University, Inchoen, Republic of Korea

## **Declaration under Oath**

Eidesstattliche Erklärung / Declaration under Oath

Ich erkläre an Eides statt, dass ich die Arbeit selbstständig und ohne fremde Hilfe verfasst, keine anderen als die von mir angegebenen Quellen und Hilfsmittel benutzt und die den benutzten Werken wörtlich oder inhaltlich entnommenen Stellen als solche kenntlich gemacht habe.

I declare under oath that this thesis is my own work entirely and has been written without any help from other people. I used only the sources mentioned and included all the citations correctly both in word or content.

Datum / Date

Unterschrift des Antragstellers / Signature of the applicant